



Strathclyde Department of Physics  
Faculty of Science

**Optical Sectioning Techniques for Widefield Fluorescence  
Mesoscopy with the Mesolens**

Jan Schniete


Thesis presented in fulfilment of the requirement for the degree of Doctor of  
Philosophy

2021

# Declaration

This thesis is the result of the author's original research with the exception of the specimen preparations in Chapters 2.2.5, 2.2.6, 2.2.7, 2.2.8, 3.2.5, 4.3.3, and the acquisition of the data used in Figure 3.8. It has been composed by the author and has not been previously submitted for examination which has led to the award of a degree.

The copyright of this thesis belongs to the author under the terms of the United Kingdom Copyright Acts as qualified by University of Strathclyde Regulation 3.50. Due acknowledgement must always be made of the use of any material contained in, or derived from, this thesis.

Signed: 

Date: 08/12/2021

# Table of Contents

List of Figures

List of Acronyms and Abbreviations (alphabetic)

Abstract

Publications & Presentations

1	Introduction	1
1.1	Light Microscopy: A Historic Overview	2
1.1.1	Spherical aberration	8
1.1.2	Coma aberration	9
1.1.3	Astigmatic aberration	10
1.1.4	Chromatic aberration	11
1.2	Fluorescence	12
1.2.1	Two-photon excitation	13
1.3	Epifluorescence microscopy	17
1.4	Confocal laser scanning microscopy	19
1.5	Light sheet microscopy	24
1.5.1	Gaussian beams and non-diffracting beams	29
1.6	Structured Illumination Microscopy	31
1.7	Mesoscopy	34
1.8	The Mesolens	37

1.9	Thesis Outline	41
2	HiLo Mesoscopy	42
2.1	Introduction	42
2.2	Methods	45
2.2.1	Theoretical background of Hilo microscopy	45
2.2.2	Experimental setup	48
2.2.3	Data processing	51
2.2.4	Measuring the optical sectioning strength of the HiLo mesoscope	52
2.2.5	Mouse hippocampal neuron specimen preparation	53
2.2.6	5-day-old zebrafish larva specimen preparation	54
2.2.7	Pollen grain specimen preparation	55
2.2.8	<i>Daphnia magna</i> (waterflea) specimen preparation	55
2.3	Results	56
2.3.1	HiLo mesoscopy optical section thickness	56
2.3.2	Pollen grain imaging with HiLo mesoscopy	59
2.3.3	<i>Daphnia</i> imaging with HiLo mesoscopy	62
2.3.4	12-day-old zebrafish imaging with HiLo mesoscopy	66
2.3.5	Mouse hippocampal neuronal specimen imaging with HiLo mesoscopy	68
2.4	Discussion	70
3	Light Sheet Mesoscopy (LSMe)	73
3.1	Introduction	73

3.2	Methods	74
3.2.1	Two-photon light sheet setup	74
3.2.2	Single-photon Gaussian light sheet setup	75
3.2.3	Fluorescent bead sample	77
3.2.4	Fluorescent dye solution	78
3.2.5	Mouse pancreas specimen	79
3.3	Results	80
3.3.1	Two-photon Gaussian light sheet	80
3.3.2	Single photon Gaussian light sheet	81
3.4	Discussion	87
4	Blind-SIM Mesoscopy (BlindMe)	91
4.1	Introduction	91
4.1.1	Deconvolution	91
4.1.2	Super resolution microscopy	92
4.2	Theory	95
4.2.1	Blind-SIM	99
4.3	Methods	103
4.3.1	Experimental setup	103
4.3.2	Blind-SIM toolbox graphical user interface (GUI)	105
4.3.3	MeT5A cell sample preparation	108
4.4	Results	109

4.4.1	<i>Taraxacum</i> Pollen grain	110
4.4.2	Actin network	118
4.5	Discussion	124
5	Conclusions and Future Work	128
5.1	Conclusions	128
5.1.1	Hilo Mesoscopy	128
5.1.2	Light Sheet Mesoscopy	129
5.1.3	Blind-SIM mesoscopy	129
5.2	Future Work	132
5.2.1	Hilo Mesoscopy	132
5.2.2	Light Sheet Mesoscopy	133
5.2.3	Blind-SIM mesoscopy	134
6	Acknowledgement	135
7	References	136
8	Appendix	i
8.1	Matlab HiLo script for processing large stacks without GPU acceleration	i
8.2	Matlab HiLo script for processing small stacks with GPU acceleration	v
8.3	User-made functions	ix
8.3.1	Low pass filter function	ix
8.3.2	High pass filter function	ix
8.3.3	Band pass filter function	x



# List of Figures

Figure 1.1: Schematic of a simple compound microscope (modified after (F. L. Pedrotti <i>et al.</i> , 2007)).	4
Figure 1.2: Visualisation of the definition of the Rayleigh criterion from [ <a href="http://hyperphysics.phy-astr.gsu.edu/hbase/phyopt/Raylei.html">http://hyperphysics.phy-astr.gsu.edu/hbase/phyopt/Raylei.html</a> ].	8
Figure 1.3: Illustration of spherical transverse ray aberration.	9
Figure 1.4: Absorption, excitation and emission principle in fluorescent dye molecules for single-photon (a) and two-photon (b) excitation.	16
Figure 1.5: Schematic of a basic widefield epifluorescence microscope.	18
Figure 1.6: Minsky's first design of a confocal microscope (modified after (M. Minsky, 1961)).	19
Figure 1.7: Depiction of single-photon and two-photon excitation of fluorescence.	23
Figure 1.8: LSM in a basic form using a cylindrical lens to create a thin sheet of light in the sample to excite fluorescent molecules.	25
Figure 1.9: Principle of structured illumination microscopy (SIM) from (M. G. L. Gustafsson, 2000).	32
Figure 1.10: Set-up used for dynamic speckle illumination microscopy.	34
Figure 1.11: Detailed view of the Mesolens prototype objective lens.	40
Figure 2.1: Experimental setup to generate speckle and uniform illumination.	50
Figure 2.2: Comparison of optical sectioning strength.	52
Figure 2.3: HiLo mesoscopy sectioning strength.	57
Figure 2.4: Illustration of the speckle illumination contrast degradation compared between pollen grain and <i>Daphnia</i> .	60



Figure 2.5: <i>Taraxacum</i> pollen grain images and quantification of signal-to-background improvement.	61
Figure 2.6: Widefield image of <i>Daphnia</i> and after processed with HiLo and deconvolution.	64
Figure 2.7: Digital zoom of the ROI indicated in Figure 2.6a showing fine detail preservation in thick specimens.	66
Figure 2.8: Standard widefield image (a) compared to Mesolens HiLo-processed optical section (b) of zebrafish stained with Acridine Orange.	67
Figure 2.9: Full field of view HiLo processed image compared to widefield image of the mouse hippocampal neuron specimen.	69
Figure 3.1: Experimental setup for two-photon light sheet generation.	75
Figure 3.2: Experimental setup for Gaussian light sheet mesoscopy on the Mesolens.	76
Figure 3.3: Illustration of the cuvette imaging setup on the Mesolens.	78
Figure 3.4: (a) Two-photon excitation image of the Safranin O filled cuvette in the spot focus setup.	80
Figure 3.5: Two-photon strip focus imaged orthogonally to the propagation direction of the illumination beam.	81
Figure 3.6: Images of 500 nm green-fluorescent beads.	82
Figure 3.7: XY, YZ and XZ views of a <i>propidium iodide</i> (PI) stained mouse pancreas obtained with the LSM illuminator.	83
Figure 3.8: Confocal mesoscopy dataset of the same mouse pancreas specimen as Figure 3.7.	85
Figure 3.9: Cropped insets of the YZ views indicated by the green boxes in Figure 3.7 and Figure 3.8 respectively.	86
Figure 4.1: Simplified overview of an iterative minimisation deconvolution process.	97
Figure 4.2: Schematic of the blind-SIM deconvolution algorithm.	100

Figure 4.3: Experimental setup for random speckle illumination.	104
Figure 4.4: The 'Data' tab (1) of the blind-SIM toolbox GUI.	105
Figure 4.5: The 'PSF' tab (1) of the blind-SIM toolbox GUI.	106
Figure 4.6: The 'deconvolution' tab (1) of the blind-SIM toolbox GUI.	107
Figure 4.7: The 'post-processing' tab (1) of the blind-SIM toolbox GUI.	108
Figure 4.8: Gaussian noise model blind-SIM images of a single pollen grain using combinations of all regularisers and positivity constraint.	111
Figure 4.9: Line plots obtained from the data in Figure 4.8, the position of the line is indicated by the green line.	112
Figure 4.10: Peak signal-to-noise ratio (pSNR) of the images in Figure 4.8.	113
Figure 4.11: Poisson noise model blind-SIM deconvolution with all regularisers and positivity constraints.	116
Figure 4.12: Line plots obtained from images in Figure 4.11.	117
Figure 4.13: Peak signal-to-noise ratio (pSNR) of the Poisson noise model data in Figure 4.11.	118
Figure 4.14: Actin network of MeT5A labeled with fluorescein phalloidin processed using blind-SIM algorithm with the available range of regularisers and positivity constraints.	119
Figure 4.15: Plots of vertical line profiles through the centre of the images shown in Figure 4.14.	120
Figure 4.16: Peak signal-to-noise ratio (pSNR) of the images in Figure 4.14.	121
Figure 4.17: Comparison between widefield image, 2D deconvolution and blind-SIM.	122
Figure 4.18: Result of tiled processing using the blind-SIM toolbox with a 2691 x 2337 x 50 image series of the same focal plane of MeT5A cells labelled with fluorescein phalloidin.	124

# List of Acronyms and Abbreviations

## (alphabetic)

1P/2P: single photon or one photon/two-photon (in the context of fluorescent molecule excitation)

2D/3D: two-dimensional/three-dimensional

BlindMe: Blind-SIM method applied to mesoscale data

CLSM: confocal laser scanning microscopy

CT: computed tomography

DOF: depth of field

DSI: dynamic speckle illumination

DSLMS: digitally scanned light sheet microscopy

FOV: field of view

FPS: frames per second

FWHM: full width at half-maximum

GUI: graphical user interface

HiLo microscopy: high spatial frequency and low spatial frequency filtered sectioning microscopy

LSFM: light sheet fluorescence microscopy

LSM: light sheet microscopy

mSPIM: multidirectional selective plane illumination microscopy

NA: numerical aperture

OCM: Optical coherence microscopy

OCT: Optical coherence tomography

OPT: Optical projection tomography

PALM: photo-activated light microscopy

PSF: point spread function

SDCM: scanning disk confocal microscopy

SIM: structured illumination microscopy

SMLM: single molecule localisation microscopy

SPIM: selective plane illumination microscopy

SR: super resolution

STED microscopy: stimulated emission depletion microscopy

STORM: stochastic optical reconstruction microscopy

W2PM: widefield two-photon microscopy

# Abstract

Optical sectioning in fluorescence microscopy is the process of removing out-of-focus light from the final image. Several techniques have been developed over the years and the gold standard remains confocal laser scanning microscopy (CLSM). As a point scanning instrument, a confocal microscope acquires data one pixel at a time which results in long acquisition times for large field of view (FOV), high-resolution images. Moreover, the confocal method is not useful when imaging large volume specimens with a low power, low numerical aperture (NA) lens. Hence optical sectioning techniques for widefield fluorescence imaging which use a digital camera to rapidly acquire high-resolution images are highly sought after. Widefield detection requires much less excitation light intensity allowing gentler imaging with less photobleaching and phototoxic effects simultaneously outperforming CLSM in acquisition speed.

This thesis reports the development of optical sectioning imaging modalities that have been specified to be compatible with the unique properties of the Mesolens, a novel microscope objective lens that combines millimetre scale FOV, submicron lateral resolution and a long working distance. Firstly, HiLo microscopy was adapted into HiLo mesoscopy. HiLo mesoscopy performs optical sectioning by modulating the in-focus signal with random speckle illumination while leaving out of focus signal uniform. Thus, a weighted map of the image is created that holds information of where the image is in focus and where it is out of focus. HiLo mesoscopy achieved a section thickness of  $5.2 \pm 0.3 \mu\text{m}$  at an acquisition speed of 30 seconds per image pair with an additional post-processing time of  $\sim 5$  minutes compared to CLSM with a section thickness of approximately  $6 \mu\text{m}$  and an acquisition speed of 15 minutes for a three-frame-average final image.

Next, a Gaussian light sheet illuminator was constructed using a cylindrical lens to form a light sheet that covered the field of view of the Mesolens. Although the optical section thickness was 30  $\mu\text{m}$  at the center and 40  $\mu\text{m}$  at the edge of the Mesolens FOV, ten times larger than the axial resolution of 7  $\mu\text{m}$  of the Mesolens would require for light sheet microscopy, in optically cleared and thick specimens the out-of-focus background was reduced when compared to widefield illumination when using this simple setup. Compared to CLSM, the section capability of the Gaussian light sheet was inferior, however, the acquisition speed is only limited by the camera framerate and the photodose to the specimen was low, as can be expected from a light sheet illumination setup.

Lastly, a structured illumination microscopy (SIM) technique called blind-SIM was implemented to attempt super-resolution (SR) at the mesoscale. Blind-SIM uses random speckle illumination and maximum likelihood estimation algorithms (deconvolution) to estimate both the illumination pattern and the object (fluorophore distribution) to achieve super-resolution. Using the blind-SIM toolbox images of pollen grain and Actin network of MeT5A cells were processed and resulted in images with increased peak signal-to-noise ratio (pSNR) of 64.71 for the pollen grain and 67.04 compared to 15.21 pSNR for a widefield image of the Actin network. Processing time for an image stack comprised of 50 slices with 2691 x 2337 pixels per image was on the order of 10 hours, suggesting a processing time for a single full FOV Mesolens image of approximately 4 days.

This thesis achieved proof of concept for the above-mentioned widefield optical sectioning techniques making them a viable alternative to CLSM and opened the path to tackling specific challenges for each technique.

# Publications & Presentations

## Paper

J. Schniete, A. Franssen, J. Dempster, T. J. Bushell, W. B. Amos, and G. McConnell, *Fast Optical Sectioning for Widefield Fluorescence Mesoscopy with the Mesolens based on HiLo Microscopy*, Sci. Rep., **8** (1), 16259, 2018.

## Oral presentations

*A Computational Method for Fast Optical Sectioning on the Mesolens Using HiLo Microscopy*, Focus on Microscopy, 25.03.2018, Singapore

*Clearing the Haze: A Computational Method For Fast Optical Sectioning On The Mesolens Using HiLo Microscopy*, Frontiers in Bioimaging, 27.06.2018, Glasgow

*Widefield Optical Sectioning on the Mesolens*, Glasgow Imaging Network, 19.08.2019, Glasgow

## Poster presentations

*Clearing the Haze: A Computational Method For Fast Optical Sectioning On The Mesolens Using HiLo Microscopy*, European Light Microscopy Initiative, 05.06.2018, Dublin

*Clearing the Haze: A Computational Method For Fast Optical Sectioning On The Mesolens Using HiLo Microscopy*, Glasgow Imaging Network Symposium, 22.08.2018, Glasgow

# 1 Introduction

The aim of this project was to develop fast optical sectioning techniques for mesoscale imaging with the Mesolens. The Mesolens (G. McConnell *et al.*, 2016) is a novel objective lens that offers a unique combination of large FOV of  $4.4 \times 2.9 \text{ mm}^2$ , long working distance of 3 mm and sub-cellular lateral resolution of  $\sim 0.6 \mu\text{m}$  that cannot be achieved with conventional microscope objective lenses. The unusual properties of the Mesolens mean that existing techniques and algorithms cannot be easily used. Commercially available cameras typically do not have sufficiently many or small enough pixels to accommodate the Mesolens (details of the technical requirements are described in Chapter 1.7). At the time of purchase of the Mesolens system used in this project only one such camera was available (VNP-29M/C, Vieworks). Furthermore, large volume specimens present an additional challenge for optical sectioning techniques at the mesoscale due to light scattering and absorption.

Optical sectioning is the process of reducing the imaging volume of a microscope to the focal volume of the objective lens (J.-A. Conchello *et al.*, 2005). This is done non-destructively, as opposed to mechanical sectioning with a microtome, where a specimen is physically sliced into thin layers which are then imaged. Optical sectioning leaves the specimen intact and can be applied in live or fixed cell and tissue imaging.

Optical sectioning techniques can be grouped into two types, namely optical and computational. Confocal laser scanning microscopy and light sheet microscopy (LSM), which is the subject of Chapter 3 fall in the realm of optical methods. The challenges with these methods are due to the combination of large FOV and high resolution. CLSM provides excellent sectioning and is considered the gold standard, however, the combination of large FOV, high resolution and the point-scanning nature of CLSM results in slow acquisition speed



of several minutes per image. LSM on the other hand is a widefield acquisition technique and limited in speed only by the camera used to acquire the image. The challenge with LSM with the Mesolens is generating a light sheet that covers the large FOV and is simultaneously thin enough to accommodate the high axial resolution.

On the computational sectioning side, the industry standard is considered deconvolution. Deconvolution uses predictions of the specimen combined with knowledge about the microscope system point spread function (PSF) and maximum likelihood estimation algorithms to remove out-of-focus background. The challenge with Mesolens data and deconvolution lies in the file size of large images of 500 megabyte (MB) per image, significantly increasing computation time and the requirement for powerful computer hardware. Moreover, deconvolution cannot be applied to all specimen types - it is broadly limited to thinner preparations (<100  $\mu\text{m}$ ).

The following sections explore the imaging techniques relevant for this project in more detail and how they can be adapted to work in combination with the Mesolens. First, I provide some general background on light microscopy and its history and the underlying physical principles.

## 1.1 Light Microscopy: A Historic Overview

The beginning of modern light microscopy can be dated back several hundred years, even though simple magnifiers have probably been used already by the Ancient Greek and during the Chinese Dynasties. Modern microscopy, however, started with the development of the compound microscope. Despite some controversy this invention is generally attributed to Zacharias Janssen in the 1590s to early 1600s (B. R. Shmaefsky, 2006; A. van Helden *et al.*, 2010). Due to the loss of historical records during the Second World War it is uncertain if Janssen truly invented the compound microscope and who else might have contributed.

There were certainly several designs available in the early 1600s of microscopes as well as telescopes, which are essentially microscopes in reverse, by different individuals, including Galileo Galilei. There is, however, no evidence whether these may have been inspired by each other or if they were separate, simultaneous developments. Regardless of who invented the first compound microscope, this early model, although basic, started the development of more sophisticated designs and paved the way for light microscopy as a method of scientific investigation.

The principle of a compound microscope, which is still used in modern microscopes, is that it consists of two lenses, an objective lens and an eyepiece (ocular lens), separated by a distance and pointed at a close object such that an image can be observed through the eyepiece at a magnification equal to the product of the individual magnifications of the two lenses (Figure 1.1) (F. L. Pedrotti *et al.*, 2007). While modern compound microscopes have several additional components (light source, condenser, frame etc.) due to their end user-oriented nature, this combination of objective and eyepiece remains the core feature and the source of their magnifying power. It should be noted at this point that modern objective lenses and eyepieces are not single lenses but are rather comprised of several lens groups which also contain multiple lens elements to correct for common aberrations including spherical or chromatic. Aberrations will be described in more detail in the following paragraphs.

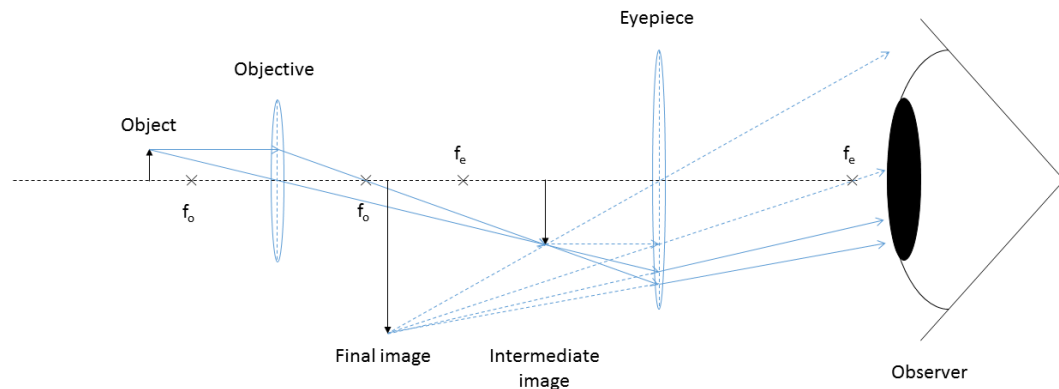


Figure 1.1: Schematic of a simple compound microscope (modified after (F. L. Pedrotti *et al.*, 2007)). The object is imaged by the objective at a point between the objective and eyepiece (the intermediate image). The observer perceives a virtual image (final image) of the object after the light is refracted by the eyepiece into the observer's eye. The total magnification is the product of the individual magnifications of the two lenses.  $f_o$  and  $f_e$  are the foci of the objective and eyepiece respectively. Dotted arrows are virtual light rays, solid arrows are real rays as per convention.

In 1665, Robert Hooke's *Micrographia* (R. Hooke, 1665) popularised microscopy not only as a science but also to the public with drawings of his observations of cork cells and other microscopic structures. Hooke coined the term 'cell' for the 'small rooms' he observed in his specimens derived from the Latin word 'cella' meaning 'storeroom' or 'chamber'. The first living cells were observed only a few years after Hooke's discoveries by Antony van Leeuwenhoek in 1673, which he communicated to the Royal Society of England in several hundred letters in the following years (A. van Leeuwenhoek, 1677; B. R. Shmaefsky, 2006). The discoveries of Hooke and van Leeuwenhoek were the basis of many advances in understanding biological processes. Particularly the discovery of bacteria, blood and sperm cells by van Leeuwenhoek made possible the understanding of infectious diseases and later also the nature of genetic material (J. D. Watson *et al.*, 1953) and the mechanics of cell division (W. Flemming, 1878).

After these early developments, it took almost 200 years until significant advances in microscopy were made again. Most notably in this context was the discovery of stains in 1854 by Joseph von Gerlach (J. von Gerlach, 1858), who used carmine to stain the nuclei of nerve cells with great success. This staining method drastically increased contrast in his fixed samples, and considerably improved the resultant image quality. The downside of staining, especially when considering thin samples on the order of 10  $\mu\text{m}$ , is the high concentration of absorption staining needed. Following the Beer-Lambert Law given by

$$A = \epsilon l C \quad (1)$$

Where  $A$  is the dimensionless observed absorbance,  $\epsilon$  is the absorption coefficient in  $\text{m}^2/\text{mol}$ ,  $l$  is the path length of light through the substance in cm and  $C$  is the concentration of the absorbing substance in mol/L. It directly follows from eq. (1) that for short path lengths (e.g., 10  $\mu\text{m}$  sample thickness, which is commensurate with the thickness of a mammalian cell) the concentration must be high to achieve high absorbance. In practice, this concentration reaches toxic levels in living cells, thus absorption staining is only used with fixed specimens since any living specimen would not survive the staining process.

The discovery of the fluorescence phenomenon in 1845 (J. F. W. Herschel, 1845a, 1845b), subsequent expansion on substances with fluorescent properties in 1852 (G. G. Stokes, 1852) and synthetic fluorescent dyes in 1871 (A. Baeyer, 1871) were of great importance to the later development of the first fluorescent microscope in the early 20<sup>th</sup> century (O. Heimstädt, 1911). The molecules of the fluorescent dye can be engineered, or used with a combination of antibodies, to bind to specific chemical structures and can thus be used to individually label different regions of interest with certain dyes (e.g., labelling the cell nucleus with one fluorescent dye and the cell membrane with another). The fluorescence emission of each dye

can then be spectrally separated, and a comprehensive composite image can be created. Fluorescence imaging is performed today in this fashion.

Another important milestone in microscopy was in 1873 when Ernst Abbe established the theoretical limit for the resolution of a microscope; the diffraction limit (E. Abbe, 1873) also called Abbe limit. The Abbe limit refers to the highest spatial frequency transmissible by the microscope system. With a simple transmission diffraction grating as an example object, the +1/-1 diffraction orders generated by the objective lens must be transmitted by the aperture in the back-focal plane to image the grating as a sinusoidal pattern. Abbe derived from this the resolving power of an optical system, i.e., the minimum grating period that can be resolved, is given by

$$d = \frac{\lambda}{2n \sin \alpha} \quad (2)$$

where  $d$  is the minimum distance between two resolvable points,  $\lambda$  is the wavelength of the light,  $n$  is the refractive index of the medium the lens operates in and  $\alpha$  is the maximum half angle of the cone of light that can enter the front element of the objective lens.

He was also the first to use the term numerical aperture for the product  $n \sin \alpha$  in eq. (2) as a measure of resolving power (E. Abbe, 1881).

In literature the term NA is commonly used and Abbe's original equation has been adapted and expressed for lateral resolution in terms of the Airy disc radius and axial resolution (J. B. Pawley, 2006):

$$r_{Airy} = \frac{0.61\lambda}{NA_{obj}} \quad (3)$$

$$z_{min} = \frac{2\lambda n}{(NA_{obj})^2} \quad (4)$$

Where  $r_{Airy}$  is the radius of the Airy disc (distance from central maximum to first minimum of a diffraction pattern),  $\lambda$  is the wavelength of the light,  $n$  is the refractive index of the medium the lens operates in,  $NA_{obj}$  is the numerical aperture of the objective lens and  $z_{min}$  is the axial distance from the central intensity maximum to the first minimum, analogous to  $r_{Airy}$ . From equations (3) and (4) it is obvious that a low NA has a more severe effect on axial resolution than on lateral resolution due to the quadratic dependence of  $z_{min}$  as opposed to the linear dependence of  $r_{Airy}$ . Two points being just resolved if their spatial separation is equal to or larger than  $r_{Airy}$  is called the Rayleigh criterion. This is shown in Figure 1.2. Other resolution limits used in microscopy are the above mentioned Abbe limit, the Sparrow limit named after Carrol Mason Sparrow (C. M. Sparrow, 1916) and the full-width-half-maximum (FWHM). The advantage of the FWHM over the other definitions of resolving power is that it can be measured from an image of a sub-resolution single emitter, like a fluorescent bead. The minimum theoretical resolution defined by the FWHM is given by:

$$r_{FWHM} = \frac{0.51\lambda}{NA_{obj}} \quad (5)$$

Where  $r_{FWHM}$  is the distance between two points that are just resolved,  $\lambda$  is the wavelength of the emitted light and  $NA_{obj}$  is the numerical aperture of the objective lens.

This fundamental resolution limit manifests itself in the so-called point spread function (PSF) of a microscope system when a point light source is imaged. The entrance pupil of a microscope is a circular aperture. Light passing through the aperture is diffracted which leads to a blurred image of the object. For objects that are smaller than the resolution limit, this image is known as the PSF of the microscope system. The theoretical PSF assumes an infinitely small object, however, experimental PSFs obtained by imaging emitters with dimensions below the expected resolution of the instrument can be used as a measure of

system performance, e.g., how well lenses are corrected for aberrations, and to experimentally determine a system's resolving power by measuring the FWHM.

Lens aberrations, specifically chromatic and spherical aberration, prevented microscopes of that time to reach the diffraction limited resolution of the optical systems. Some of the most common aberrations are briefly explained below.

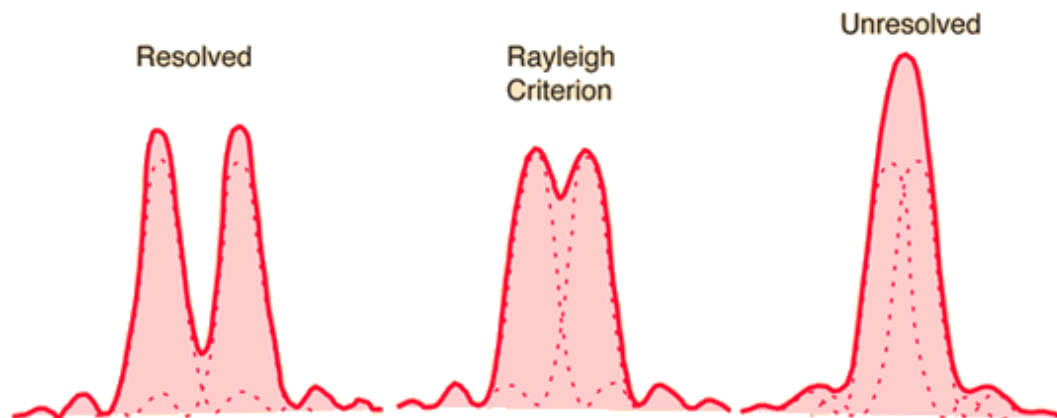


Figure 1.2: Visualisation of the definition of the Rayleigh criterion from [<http://hyperphysics.phy-astr.gsu.edu/hbase/phyopt/Raylei.html>]. The left shows two small light sources clearly resolved, the middle shows them just resolved as per the Rayleigh criterion and the right shows two sources that are not resolved, i.e. they cannot be distinguished from a single source given the resolving power of the instrument used to acquire the image.

### 1.1.1 Spherical aberration

Spherical aberration is a direct consequence of the geometry of a spherical lens (or mirror). Paraxial rays (light rays that only make a small angle with and/or travel close to the optical axis) are focused in a different plane than peripheral rays (light rays that make larger angles with and/or travel far from the optical axis) (F. L. Pedrotti *et al.*, 2007; J. Sanderson, 2019), thus the light coming from the object is focused at different positions along the optical axis resulting in a blurred image. Spherical aberration can be positive or negative, depending on the lens type (convex or concave). Lenses can be manufactured to be aspherical (R. Kingslake *et al.*, 2010), but these are more difficult to accurately produce. Alternatively, only a fraction

of the lens diameter can be used, but this results in a low numerical aperture and only weak focusing. Common practice is to use a combination of lenses such that the aberration of one lens exactly cancels the aberration of the other.

$$SA \propto \rho^3 \quad (6)$$

Spherical transverse ray aberration ( $SA$ ) is proportional to the cube of the so-called zonal radius  $\rho$  but it is independent of the object position in the field of view (M. Born *et al.*, 1970).  $\rho$  is measured in the exit pupil as a distance from the optical axis. It is more convenient to think of the zonal radius as the aperture size or NA of the microscope system. Figure 1.3 shows a diagram of a generic imaging instrument and illustrates the spherical transverse ray aberration.

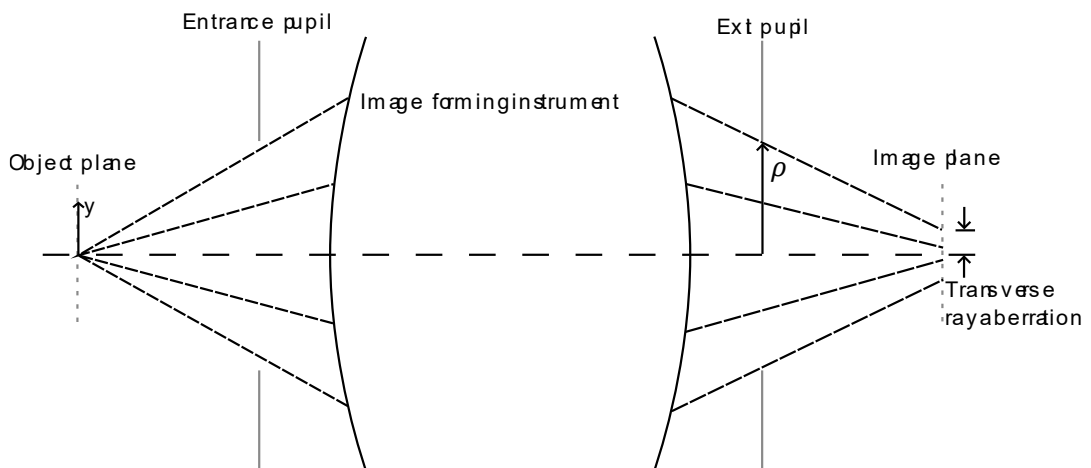


Figure 1.3: Illustration of spherical transverse ray aberration.  $\rho$  is the distance of the ray from the optical axis as it passes through the exit pupil,  $y$  is the position of the source in the object plane adapted from (M. Born *et al.*, 1970). In the case of spherical aberration, the position in the object plane does not contribute to the aberration (see equation (6)).

### 1.1.2 Coma aberration

Coma is generally associated with off-axis light sources. An off-axis point source appears to have a tail, like a comet. Like spherical aberration, this is due to the geometry of the lens itself and can be corrected by using several lenses that exactly cancel out their respective



aberrations. In practice, a doublet or triplet lens is used to correct for coma aberration (J. Sanderson, 2019).

Coma aberration is proportional to the square of the zonal radius and depends linearly on the object position in the field of view.

$$CA \propto y\rho^2 \quad (7)$$

Where  $CA$  is the Coma transverse ray aberration,  $y$  is the object distance from the centre of the field of view and  $\rho$  is the zonal radius.

### 1.1.3 Astigmatic aberration

Astigmatic aberration occurs when light rays from perpendicular planes focus at different locations along the optical axis. These are called tangential and sagittal foci. In general, this is due to imperfections in the lenses, but it can also result in optical systems where lenses are poorly centred on the optical axis or poorly aligned with other optical elements (H. E. Keller, 2006). There are situations where this effect is desired, e.g., in cylindrical lenses that focus a light beam only in one dimension, thus creating a flat sheet at the focus rather than a point. These lenses had success in light sheet microscopy applications (E. Fuchs *et al.*, 2002; J. Huiskens *et al.*, 2009; P. A. Santi, 2011).

Astigmatic aberration is proportional to the zonal radius and the square of the position of the object in the field of view.

$$AA \propto y^2\rho \quad (8)$$

where  $AA$  is the Astigmatic transverse ray aberration,  $y$  is the object distance from the centre of the field of view and  $\rho$  is the zonal radius.

#### 1.1.4 Chromatic aberration

Axial chromatic aberration is a consequence of the refractive index  $n$  being a function of the wavelength  $\lambda$  of light (F. L. Pedrotti *et al.*, 2007). Different wavelengths, or colours, of light passing through a lens are focused on different positions along the optical axis, thus blurring the image. Like spherical aberration, chromatic aberration is corrected by passing light through another optical element. In addition to the second element having opposite curvature, the material has a different dispersion, i.e. the difference in refractive index for the individual colours is larger (or smaller) (J. Sanderson, 2019). Thus, the different colours are brought to the same focus.

Unlike the afore-mentioned monochromatic aberrations, chromatic aberration does not depend on the zonal radius or position of the object in the field of view but only on the difference in refractive index of a given lens material with respect to the wavelength of light passing through it.

Together with Carl Zeiss and Otto Schott, Abbe developed and improved optical tools to measure aberrations and diffraction of optical systems (E. Abbe, 1874) as well as lenses that were corrected for chromatic and spherical aberration (achromatic lenses) that made reaching the diffraction limit with microscope systems working with visible light possible.

Since spherical and chromatic aberrations are corrected through similar processes, they can both be corrected using a lens type called an apochromat (J. Sasian, 2017), which is comprised of three elements and corrected for spherical and chromatic aberration for three colours.

Once high-quality lenses were readily available and the diffraction limit was reached, using a shorter wavelength of light was a good way to achieve better resolution. This is a direct consequence of equation (2); the smaller the wavelength, the smaller becomes the minimum

resolvable distance between two points. August Köhler, who was also working at Carl Zeiss AG, constructed the first microscope using ultraviolet (UV) light in 1904 thereby achieving approximately twice the resolution of regular visible light microscopes (A. Köhler, 1904; J. Smiles, 1958). He also developed what is known as 'Köhler illumination' in 1893 (A. Köhler, 1893), still widely used as a standard illumination technique in microscopy as it produces the best image quality in most microscope systems. In Köhler illumination, the sample is uniformly illuminated over the entire field of view by imaging the light source onto the back focal plane of the illumination lens (either the condenser in transmission illumination or the objective lens in epi illumination). Thus, the light source is placed at infinity. The process is not complicated, especially because modern microscopes are built to allow the user adjustment of all the relevant components in the illumination optical train.

During his work with UV light Köhler also noticed that there was visible light emitted by specimens, but it was Oskar Heimstädt who realised the importance of this fluorescence phenomenon leading to the construction of the first fluorescence microscope in 1911 (O. Heimstädt, 1911).

The 20<sup>th</sup> century saw a great number of developments in the field of microscopy. The following chapters will give a more detailed overview of the techniques that are relevant for this project, as well as their advantages, and disadvantages. It should be noted at this point that there are many more methods, however, only those are covered that are directly relevant to the work presented in this thesis.

## 1.2 Fluorescence

Fluorescence is the physical process of the absorption of a photon, excitation of the dye molecule and emittance of a photon of light of longer wavelength. This process is illustrated in Figure 1.4a. This phenomenon allows to detect only the emitted light by filtering out the

excitation light, resulting in bright signal on a dark background, increasing contrast in the acquired images. Further, it allows specific labelling when imaging fixed biological specimens because it is possible to have fluorescent dyes bind to specific chemical structures. For example, it is possible to have a dye bind to DNA in the cell nucleus (D. J. Arndt-Jovin *et al.*, 1989) to differentiate the cell nucleus from the cytoplasm or other cellular organelles. This advantage however is not unique to fluorescence imaging but can also be achieved with non-fluorescent chromophores. Lastly, functional imaging of live specimens became possible without the need to introduce external fluorescent probes by the development of green fluorescent proteins (O. Shimomura, 1979; J. Wiedenmann *et al.*, 2009). A wide variety of fluorescent dyes and fluorescent proteins have been developed since the original discovery of the phenomenon to label different structures in biological specimens and to use optical techniques to produce high contrast images of the cellular features of interest. This has led to fluorescence imaging becoming a widely used form of imaging in biological research.

The excitation light in fluorescence microscopy is always of shorter wavelength than the detected light due to the Stokes shift that occurs in the fluorescent dye molecules (G. G. Stokes, 1852; J. B. Pawley, 2006), except in the special case that is multi-photon excitation. The commonest type of multi-photon microscopy is two-photon microscopy, which I will describe in brief in the following section.

### 1.2.1 Two-photon excitation

Two-photon excitation requires two photons being absorbed simultaneously by one fluorescent dye molecule, thus the optical intensity required for this process is very high. The two-photon absorption process is inherently non-linear which leads to the optical sectioning capability of two-photon microscopy which is discussed in the next paragraph.

Figure 1.4 shows a simple diagram that illustrates how absorption of a photon of light, excitation of the absorbing molecule and subsequent emission of a fluorescent photon of light occurs in dye molecules for both single-photon and two-photon excitation. For fluorescence to occur an incident photon must have sufficient energy to be absorbed by the fluorescent dye molecule, exciting an electron to a higher energy level. After non-radiative relaxation the electron drops to a lower energy state, emitting a photon with an energy that is lower than the energy of the photon that was originally absorbed. Another set of non-radiative relaxation brings the electron back to its original ground state, ready to start the cycle again. In two-photon excitation the process of relaxation is identical, however, two photons are required to excite the electron from the ground state to the excited state. In the case of two-photon excitation, each photon typically has half the required energy to excite the electron such that their simultaneous absorption is sufficient for the electron to reach the excited state. However, two-photon excitation is possible with two photons having different energy provided the sum of their individual energy is sufficient to excite the electron in the dye molecule. Clearly, for two photons to arrive simultaneously, the radiation density must be very high which in turn leads to the non-linear absorption process, i.e., outside the focal volume of a focused laser beam, the absorption and thus fluorescence excitation and emission does not decline linearly but scales with the square of the instantaneous intensity. This non-linearity is the cause of the inherent optical sectioning of multiphoton microscopy. Furthermore, the high intensity necessitates the use of a pulsed laser to reach high peak intensity while keeping the average incident power low. Two-photon fluorescence excitation is described by the equation published in 1990 (W. Denk *et al.*, 1990):

$$n_a = \frac{p_0^2 \delta}{\tau_p f_p^2} \left( \frac{A^2}{2\hbar c \lambda} \right)^2, \quad (9)$$

where  $n_a$  is the number of photons absorbed per molecule per pulse,  $p_0$  is the average incident laser power in  $mW$ ,  $\delta$  is the two-photon absorption cross section of the fluorescent dye used in  $\frac{cm^4s}{photon}$ ,  $\tau_p$  and  $f_p$  are the pulse duration in  $fs$  and repetition rate of the laser in  $MHz$  respectively,  $A$  is the numerical aperture of the lens focusing the pulsed laser beam,  $\hbar$  is the reduced Planck's constant in  $Js$ ,  $c$  is the speed of light in  $\frac{m}{s}$ , and  $\lambda$  is the wavelength of the pulsed laser light in  $nm$ .

This equation does not account for fluorophore saturation and the paraxial approximation is used. If the result of the calculation would give a value for  $n_a$  larger than one, that would constitute saturation since a single fluorescent molecule cannot reach more than one excited state per pulse since the pulse duration is significantly shorter, on the order of 100s of femtoseconds, than the fluorescent lifetime, typically on the order of nanoseconds (W. Denk *et al.*, 1990). Therefore, absorption-excitation-emission cycles are achieved with repetition rates of  $\sim 100$  MHz and pulse durations on the order of 100 fs without saturation (A. Diaspro,

P. Bianchini, *et al.*, 2006). The pulse length can be adjusted to achieve lower average power with shorter pulses or lower peak power with longer pulses.

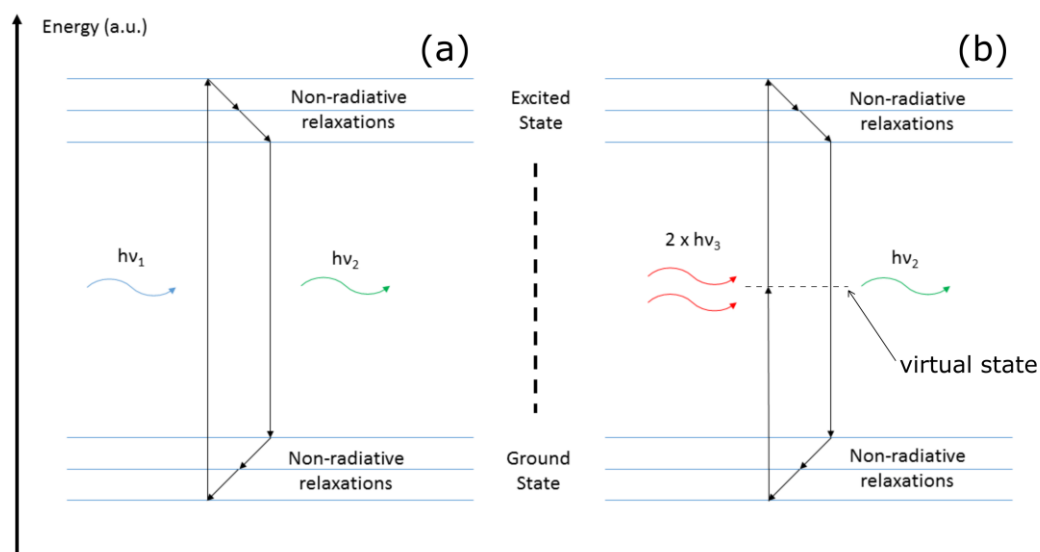


Figure 1.4: Absorption, excitation and emission principle in fluorescent dye molecules for single-photon (a) and two-photon (b) excitation. A photon of sufficient energy  $h\nu_1$ , where  $h$  is Planck's constant and  $\nu$  is the frequency of light, excites the fluorescent molecule and elevates an electron to the excited state. After some non-radiative relaxation, a photon with energy  $h\nu_2$  is emitted, where  $\nu_2 < \nu_1$ . In two-photon excitation, two photons of energy  $h\nu_3$  are absorbed simultaneously, where either photon on its own has insufficient energy to excite the dye molecule but combined, they do. The energy level where one of the two photons could excite the dye to is marked as the virtual state. This state is purely for illustration purpose as there is no energy level present, hence the necessity for the two photons to arrive at the dye molecule simultaneously. Again, after some non-radiative relaxation a photon with energy  $h\nu_2$  is emitted, however, in the two-photon case,  $\nu_2 > \nu_3$ . In both cases, the molecule undergoes non-radiative relaxation and ends up in its original ground state.

The concept of two-photon excitation extends in general further to multi-photon excitation, however, the principles remain the same and the experimental work of this thesis does not extend further than two-photon excitation. Thus, the details of general multi-photon fluorescence excitation are not covered here.

## 1.3 Epifluorescence microscopy

Widefield epifluorescence microscopy, on its own, has no optical sectioning capabilities. Images suffer from weak contrast as a direct result that out-of-focus background light is also detected together with the desired in-focus signal if the specimen has a thickness larger than the depth of field (DOF) of the microscope. Furthermore, widefield epifluorescence illumination can induce photobleaching effects because the entire field of view of the sample is illuminated during imaging. Considering that in thick specimens a large fraction of the generated fluorescence is out-of-focus background in the final image, this bleaching is particularly wasteful.

Widefield epifluorescence microscopy was one of the most common microscopy techniques before confocal laser scanning microscopy was invented (J. G. White, W. B. Amos, *et al.*, 1987). The difference between epifluorescence and transmission fluorescence microscopy is that in epifluorescence the illuminating beam passes through the same objective lens as the detection beam. In other words, the illumination and detection are on the same side of the specimen (Figure 1.5). Only a small amount of reflected excitation light from the sample finds its way back into the objective and towards the detector. However, it is still essential to filter out the back scattered light as it is typically several orders of magnitude higher than the fluorescence signal. Usually, this is achieved by using a dichroic mirror that also guides the excitation light into the sample to begin with (see Figure 1.5), and a further emission detection filter.



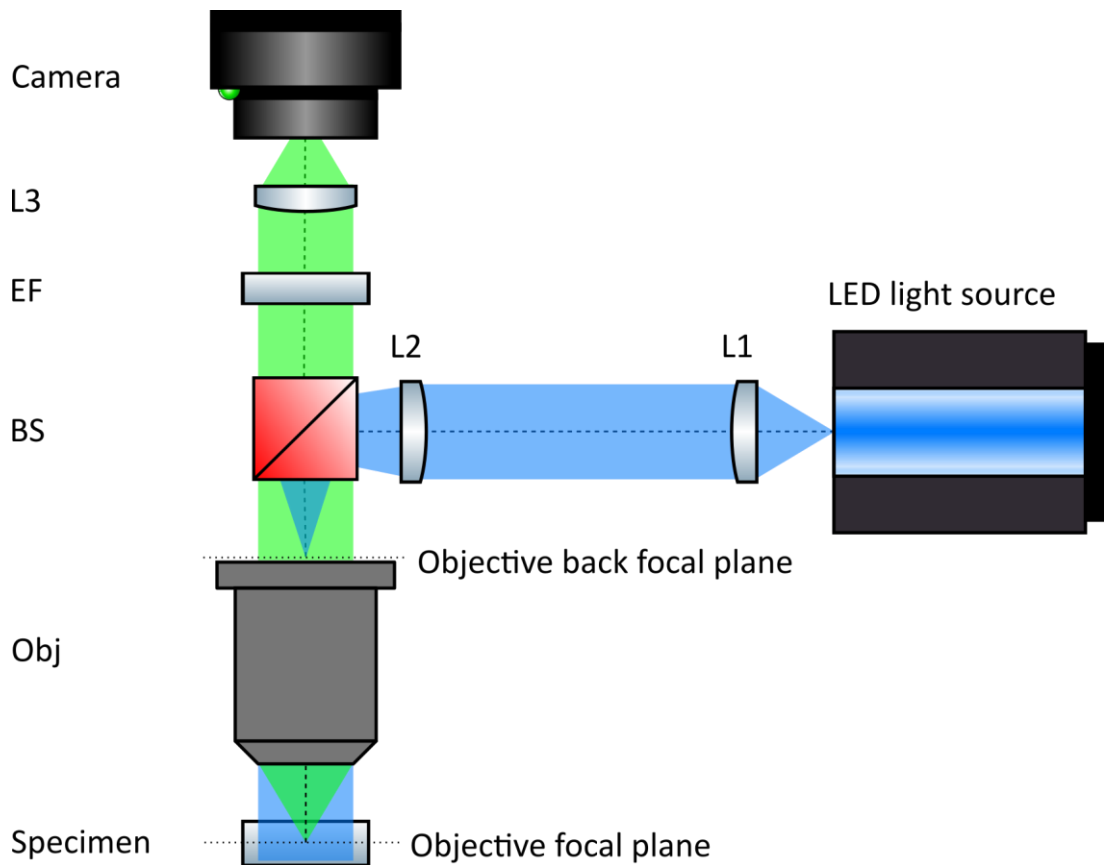


Figure 1.5: Schematic of a basic widefield epifluorescence microscope. The light from the LED is collected and collimated by lens L1 and then focused by lens L2 on the back focal plane of the objective lens via the dichroic beam splitter, BS, resulting in a parallel beam exiting the front element of the objective lens, Obj. The generated fluorescence emanating from the sample is collected by the objective lens and passes through the beam splitter rather than being reflected as it has a longer wavelength than the excitation light and, after passing the emission filter, EF, is focused by lens L3 onto the camera detector.

Widefield epifluorescence microscopy has fast acquisition speed, in principle only limited by the camera frames per second (fps) for bright specimens, because the image is taken using a parallel beam to illuminate the specimen and a camera to detect fluorescence emission in a single snapshot.

Despite being the oldest fluorescence imaging technique, it still has an important place in modern microscopy. The simplicity of the set-up of a commercial epifluorescence microscope makes it an easy-to-use efficient tool for researchers to image specimens. Thin slices of fluorescent specimens or cell monolayers can be imaged without the wasteful

photobleaching and strong background fluorescence. The fast acquisition speed, which is only limited by the detector speed, makes it an attractive technique to investigate fast biological processes and allows time lapse imaging at the same time.  $\text{Ca}^{2+}$  imaging of neurons is an example for observing fast biological processes which cannot be captured easily with point scanning techniques due to the low temporal resolution (P. W. Tinning *et al.*, 2018).

## 1.4 Confocal laser scanning microscopy

The confocal microscope was invented in 1955 and patented in 1961 by Marvin Minsky (M. Minsky, 1961). The key components of his microscope, shown schematically in Figure 1.6, were the two pinhole apertures in the conjugate focal planes in the illumination and detection light paths respectively. The illumination beam is confined by the entrance pinhole such that only a small point in the specimen is illuminated. Similarly, the exit pinhole in the confocal plane limits the detection beam. Therefore, the light from the specimen that did not originate from the focal point was rejected and did not reach the detector. This combination of confocal planes and pinholes provided optical sectioning of the specimen without the need to physically slice it into thin layers (J. B. Pawley, 2006).

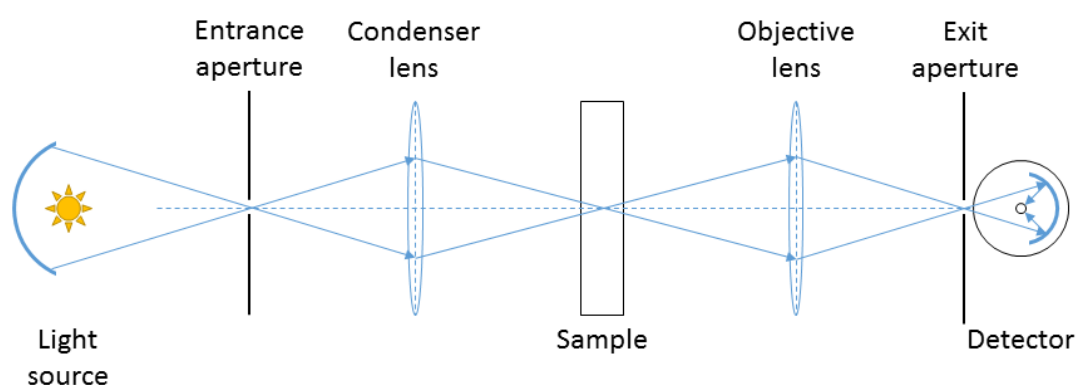


Figure 1.6: Minsky's first design of a confocal microscope (modified after (M. Minsky, 1961)). The entrance aperture limited the light to a small point from which the light diverged. The condenser lens focused the beam on a point in the specimen and the objective lens then produced an image of that point at the exit aperture. Light

originating from other points along the optical axis or laterally displaced were refracted by the objective lens such that they struck the body of the exit aperture rather than the pinhole, thus these rays did not reach the detector.

While the original design by Minsky confined an extended light source to a small point light source, newer designs feature lasers, which are intrinsically point light sources and, as such, they do not require an entrance pinhole. However, irrespective of the illumination methods the exit pinhole is still needed to reject the out-of-focus light. This technique, due to the focused illumination on the sample and point-like detection of the signal, required scanning of the sample to acquire a complete image, as opposed to widefield microscopy where the entire specimen was uniformly illuminated, and the entire image was acquired in a snapshot. Scanning with the model from 1961 was done by moving the sample through the focal point. Newer designs use scanning mirrors to move the light spot laterally across the sample. The first commercial model of a CLSM was invented in 1986 and patented in 1987 (J. G. White and W. B. Amos, 1987a, 1987b; J. G. White, W. B. Amos, *et al.*, 1987). The advantage of scanning mirrors is that the scanning process is faster (J. G. White, W. B. Amos, *et al.*, 1987) compared to moving the sample stage through the focus spot. This flying spot approach is actually older, first published in 1951 (J. Z. Young *et al.*, 1951), than Minsky's confocal microscope, however, only the development of lasers and their use in microscopy made it a useful approach for confocal microscopy. It should also be noted that scanning mirrors required accurate control and alignment, usually by computers, and high-quality manufacture of the mirrors to begin with to reach their full potential. These criteria were difficult to achieve when Minsky invented the first confocal microscope but has since made the instrument a very powerful imaging tool in today's research (W. B. Amos *et al.*, 2003).

The point scanning nature and pinhole setup of confocal microscopy provides excellent optical sectioning, however, there are several disadvantages associated with it. It is comparably slow in acquisition since the image is obtained point by point. The sampling rate

has to satisfy the Shannon-Nyquist theorem (C. E. Shannon, 1949) for full-resolution imaging. Specifically, the sampling rate must be two times the minimum resolvable detail to accurately record the signal. Further, the laser must remain in each object position long enough to collect photons and form an image with a high signal-to-noise ratio. This is known as the pixel dwell time and it is typically on the order of microseconds. The combination of point-by-point scanning, pixel dwell time and field of view determines the acquisition time for a single image. As described above, widefield imaging is only limited by the speed of the camera detector, but just considering video rate (i.e., 24 fps) meant one image acquisition must take no longer than 4 ms. For a standard confocal microscope, it is reasonable to assume a pixel dwell time of about 5  $\mu$ s (for dim samples this could get several times larger or more laser power must be used, potentially damaging the sample). For an image of size 1024 x 1024 pixels it therefore takes more than five seconds for one frame. Confocal images are usually averaged over at least three frames per image to remove random noise. Hence, even if we only consider small images, CLSM is not suited for imaging at high speeds, limiting its application mainly to fixed specimens. An exception to this is Spinning Disk Confocal Microscopy (SDCM) with a Nipkow disk (G. Q. Xiao *et al.*, 1988). SDCM used a fast-spinning disk perforated by many pinholes arranged in an Archimedean spiral. This approach effectively represents many confocal systems working in parallel being imaged simultaneously by a high framerate digital camera. In practice, such a system is limited by camera speed and signal strength rather than disk rotation speed (M. Petr  n *et al.*, 1968; E. WANG *et al.*, 2005; W. B. Amos *et al.*, 2011), however, the disk rotation speed is the physical limit for SDCM.

Another disadvantage of confocal microscopy is the shallow imaging depth. Specimens scatter light as it passes through, hence the thicker the specimen, the more the light is scattered. There are two types of scattering that are important in fluorescence imaging:

Rayleigh scattering and Mie scattering. Rayleigh scattering is highly wavelength dependent and strongly affects short wavelength light (P.-C. Cheng, 2006a) and is caused by small objects, less than a tenth of the wavelength of the light used (P.-C. Cheng, 2006b). Light is scattered by structures on the same order of or larger than the wavelength by Mie scattering. Furthermore, Mie scattering is only weakly wavelength dependent (P.-C. Cheng, 2006b). In fluorescence imaging, the excitation light has shorter wavelength than the emission light and is thus affected more by Rayleigh scattering. In confocal scanning this leads to poorer depth penetration of the unscattered excitation beam and thus weaker signal. Epifluorescence excitation light suffers from the same problem of shorter excitation wavelength, however, because the excitation in CLSM is focused, the scattering strongly affects the signal of a given point in the specimen, whereas in epifluorescence, the excitation beam is collimated and fills the FOV, therefore scattering is less problematic. The CLSM method can be combined with multi-photon excitation of the sample to overcome the lack of depth penetration (W. Denk *et al.*, 1990; W. B. Amos *et al.*, 2003). In addition to the increased depth penetration of the excitation beam, multi-photon excitation is confined to the focal volume of the beam due to the non-linearity of the absorption process reducing the effects of photobleaching (V. E. Centonze *et al.*, 1998). Figure 1.7a shows a simple graphic of the difference between single- and two-photon excitation and Figure 1.7b shows a real comparison using a Safranin Orange solution in a cuvette being excited with a continuous wave laser (top) leading to single-photon excitation and a pulsed IR laser (bottom) leading to two-photon excitation. In the two-photon case, the fluorescence excitation was tightly contained to the focal volume of the excitation beam since only in this region the intensity was high enough to result in visible two-photon excitation. In the single-photon case, the entirety of the beam excited fluorescence which, in a specimen, would be a source of out-of-focus fluorescence and photobleaching.

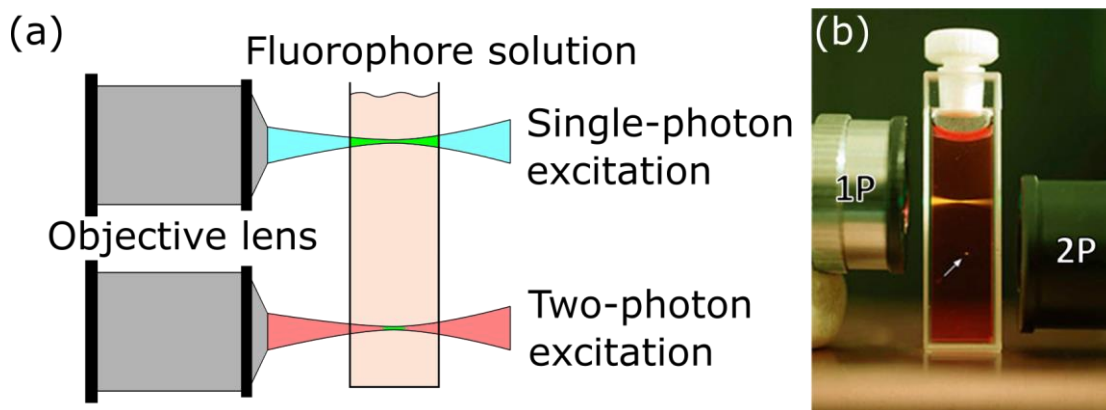


Figure 1.7: Depiction of single-photon and two-photon excitation of fluorescence. A simple schematic of the difference between single-photon and two-photon (a) and a photograph taken by Prof W B Amos of how single-photon and two-photon excitation differs in a real specimen (b). In both cases (single-photon and two-photon) the excitation beam had the same shape but the non-linear absorption process for the two-photon excitation resulted in the excitation being limited to the focal volume where the beam intensity high enough for visible two-photon excitation. Single-photon excitation occurred everywhere along the beam propagation which, in a real specimen, would generate out-of-focus fluorescence and potentially photodamage and photobleaching outside the focal plane of the microscope.

High phototoxicity and photobleaching are further disadvantages of CLSM. Phototoxicity and photobleaching are two forms of photodamage important in fluorescence imaging that are a result of the presence of photogenerated reactive oxygen species in the specimen. Photobleaching is the loss of the ability of the dye molecule to fluoresce permanently (A. Diaspro, G. Chirico, *et al.*, 2006). When a dye molecule is excited, it enters the excited singlet state and it may relax non-radiatively to the triplet state where it can absorb another photon and reach an excited triplet state. In the triplet states, it is highly reactive, and it can bind to oxygen species present in the specimen, effectively destroying the dye molecule. Phototoxicity is a concern in live cell imaging as the aforementioned reactive oxygen species react with proteins, lipids and other molecules in the cell reducing cell viability (I. D. Johnson, 2006; M. E. Dailey *et al.*, 2006). The power delivered to the sample at the focal point can be substantial, on the order of 100's of  $\mu\text{W}$  leading to fluorescence saturation, i.e., most molecules are in the excited state, thus photobleaching can occur more frequently. The high

power is necessary in confocal microscopy because the exit pinhole also limits the in-focus signal, thus more excitation is required to obtain a contrast-rich image. In addition, the short pixel dwell time on the order of microseconds requires bright emitters to collect sufficiently many photons. Further, photomultiplier tubes have low efficiency, requiring more incident photons to acquire high signal-to-noise ratio images. Lastly, although excitation is limited laterally in the sample, it does still occur along the optical axis, but this light is blocked by the exit aperture making it an unwanted source of photobleaching. Regardless of these limitations, CLSM is still one of the most used techniques in cell biology and biological imaging because of the excellent background rejection and thus optically sectioned, high contrast images.

## 1.5 Light sheet microscopy

Originally developed in 1902 (H. Siedentopf *et al.*, 1902), light sheet microscopy was used to observe gold nanospheres in a colloidal suspension. Orthogonal illumination with respect to the detection beam axis resulted in a dark background, and only light scattered by the gold spheres that reached the detection optics was visible. Richard Zsigmondy and Henry Siedentopf used the approach as a novel dark-field illumination method and coined the term “ultramicroscopy”. Zsigmondy was awarded the Nobel prize in Chemistry in 1925 for his work and this early development is seen as the birth of modern nanoscopy.

LSM has gained popularity since its adaptation for modern microscopy in 1993 (A. H. Voie *et al.*, 1993) as orthogonal-plane fluorescence optical sectioning (OPFOS) and more recently as selective plane illumination microscopy (SPIM) (J. Huisken *et al.*, 2004). In both OPFOS and SPIM, the sample is illuminated with a thin sheet of light at a 90° angle with respect to the detection objective such that the illuminated plane coincided with the focal plane of the detection objective. This method of illuminating the sample limited fluorescence excitation

to the focal volume of the detection objective, avoiding the generation of out-of-focus background fluorescence. A simple schematic of the set-up is shown in Figure 1.8.

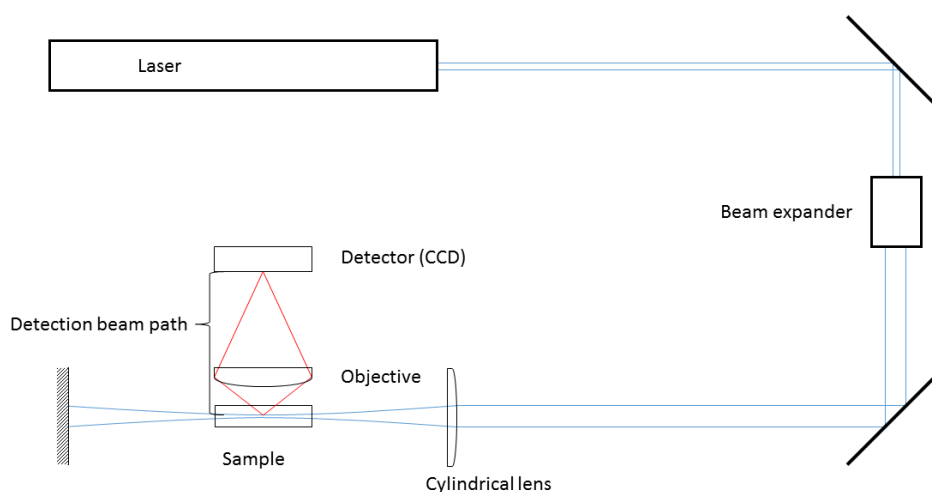


Figure 1.8: LSM in a basic form using a cylindrical lens to create a thin sheet of light in the sample to excite fluorescent molecules. The detection beam path is at an angle of  $90^\circ$  to the excitation beam path. The thickness and size of the light sheet is determined by the beam diameter incident on the cylindrical lens and its focal length.

The light sheet is commonly generated in two distinct ways; light passes through a cylindrical lens which focuses the beam vertically but not horizontally, thus creating a thin sheet of light at the focal plane of the detection objective lens (C. J. Engelbrecht *et al.*, 2010; Z. Yang *et al.*, 2014). Alternatively, the excitation beam is focused to a spot that has a Rayleigh length that covers half the FOV in one dimension of the detection objective to either side of the focus (J. Mertz *et al.*, 2010; F. O. Fahrbach *et al.*, 2013; R. Tomer *et al.*, 2015). The beam is then scanned over the other lateral dimension of the detection objective to form a virtual sheet of light over the exposure time of the camera used to acquire the image. This approach is called digitally scanned laser light sheet microscopy (DSLM) (P. J. Keller *et al.*, 2008, 2010). To keep the beam oriented the same way while scanning it, it passes through a lens that converts beam incidence angle into a lateral translation (e.g., an f-theta lens). There are



several review papers that give a good overview over these approaches (J. Huiskens *et al.*, 2009; P. A. Santi, 2011). For brevity, I cover only some of the main methods here.

In its modern implementation, LSM has become the tool of choice used in developmental biology for imaging of live specimens and millimeter scale cleared specimens (U. Krzic *et al.*, 2012; A. Bassi *et al.*, 2015), out-performing confocal laser scanning microscopy in speed as well as being a gentler imaging technique. LSM techniques are commonly used for the study of zebrafish brain development (P. J. Keller *et al.*, 2008; P. J. Scherz *et al.*, 2008; J. Huiskens *et al.*, 2009; P. J. Keller, 2013; Y. Wan *et al.*, 2019). The gentle illumination scheme allows for repeated imaging of the same embryo during its development, capturing the whole brain at cellular resolution. The orthogonal illumination optically sections the specimen by exclusively exciting fluorescent molecules in the focal plane of the detection objective, thus photobleaching and phototoxicity is reduced (R. M. Power *et al.*, 2017). Furthermore, limiting the excitation light to the focal plane of the detection objective means that less overall power is required to generate the same fluorescent response compared to CLSM (M. Jemielita *et al.*, 2013) by making optimal use of the generated fluorescence photons. LSM setups use digital cameras to record the image which have a limited dynamic range, i.e., each pixel can detect a limited number of photons before it is saturated. In LSM, assuming that the thickness of the light sheet is designed to match the collection range of the objective, fluorescence photons that reach the entrance pupil of the detection objective originate exclusively from the focal volume, whereas in CLSM, the pinhole blocks all photons that originate from out-of-focus regions in the specimen. Thus, LSM techniques generate better signal-to-background ratio at equal excitation power compared to CLSM by making better use of the available photon budget.

Furthermore, LSM is a widefield microscopy technique and can be used at acquisition speeds only limited by camera framerate, provided the specimen is bright enough and can tolerate

the excitation light power. A dedicated setup has been reported that is capable of reaching over 62.5 frames per second for imaging whole zebrafish specimen volumes in <10 seconds (B. Schmid *et al.*, 2013). Z-stacks for three-dimensional imaging of small and transparent specimens can be obtained quickly if both light sheet and objective focal plane can be moved synchronously.

These advantages make LSM techniques an excellent choice for in vivo imaging and fast volumetric imaging of optically transparent specimens.

However, the side-on illumination of the sample has disadvantages as well. The sheet needs to be converging and diverging at shallow angles to generate a large sheet of light of uniform thickness across the FOV of the detection objective. This can cause shadows being cast if opaque or scattering objects are in the beam path resulting in uneven illumination giving rise to the common 'striping' artefacts (A. Rohrbach, 2000, 2009; F. O. Fahrbach *et al.*, 2013). Similarly, in densely labeled and scattering samples, excitation light intensity is reduced along the propagation direction of the light sheet due to scattering and absorption, thus the detected fluorescence appears to decrease across the FOV. This effect is akin to signal degradation with imaging depth in CLSM, where deeper imaging into a scattering sample results in less signal being detected in the final image. In CLSM this means that z-stacks appear dimmer with increasing imaging depth into the specimen whereas in LSM any given image appears to get dimmer along the propagation direction of the light sheet.

Several techniques have been developed to counter these effects. Dual sided illumination (J. Huisken *et al.*, 2007; K. Becker *et al.*, 2008) uses two excitation beam paths instead of one, illuminating the specimen simultaneously from opposite sides and thus creating two light sheets that overlap and ensure uniform illumination. Additionally, slightly changing the angle at which the light sheet propagates through the specimen during image acquisition can

reduce striping and shadowing demonstrated with multidirectional SPIM (mSPIM) (J. Huisken *et al.*, 2007, 2009). Multiview light sheet is another approach to reduce artefacts and overcome the challenge of declining brightness across the FOV in large scattering specimens by rotating the sample with respect to the static illumination and detection beam paths. Thus several images were taken from different viewing angles and combined post-acquisition to form a complete 3D-image (J. Swoger *et al.*, 2007; U. Krzic *et al.*, 2012).

Thus far only single-photon LSM was considered. However, two-photon laser scanning microscopy and its benefits are well established (W. Denk *et al.*, 1990; F. Helmchen *et al.*, 2005) and have been used in LSM in various forms. Two-photon light sheet microscopy can generate thin sheets deep into scattering samples and has been shown to be superior in axial resolution to single-photon light sheet systems and also faster and gentler than two-photon point scanning systems (T. V. Truong *et al.*, 2011; F. O. Fahrbach *et al.*, 2013). The speed advantage of two-photon light sheet over two-photon point scanning comes from removing one scanning dimension; Rather than scanning the FOV laterally in two dimensions, the focused orthogonal illumination already covers the FOV in the direction of the illumination beam propagation and is scanned across the FOV's second dimension only as outlined earlier when DSLM was introduced.

Oblique plane microscopy (OPM) (C. Dunsby, 2008) is interesting because the light sheet is guided into the sample by the objective lens, hence removing the need for synchronous sheet and objective movement or a moving stage. Furthermore, this approach allows imaging of multi-well plates which was not possible with side on illumination due to the limited physical space available between orthogonally oriented illumination and detection arms in 'standard' LSM, as well as the fact that multi-well plates themselves are not well suited to allow side-on illumination. According to Dunsby (C. Dunsby, 2008), this technique resulted in lower detection NA but still provides sufficient resolution to obtain high quality images. Another

approach that also uses epi-illumination is to have the detection and illumination arm at 90° angles to each other but also at 45° angle with respect to the specimen (i.e., the glass cover slip) (A. K. Glaser *et al.*, 2017; B. Hu *et al.*, 2019). The setup reported by Hu *et al.* used either arm for both detection and illumination creating a dual view setup.

### 1.5.1 Gaussian beams and non-diffracting beams

Generating the light sheet can be challenging and there is always a trade-off between field of view and light sheet thickness due to the nature of Gaussian beam propagation. A Gaussian beam that is brought to a small focal point on the order of the wavelength will diverge following the well-known equation for Gaussian beam divergence (J. A. N. Buytaert *et al.*, 2012; J. Sanderson, 2019).

$$\omega_z = \omega_0 \sqrt{1 + \left(\frac{z}{z_r}\right)^2} \quad (10)$$

With  $\omega_z$ , the beam waist in  $\mu\text{m}$  at a given distance,  $z$  in  $\mu\text{m}$ , from the focal point,  $\omega_0$ , the beam waist in  $\mu\text{m}$  at the focal point and  $z_r$ , the Rayleigh range in  $\mu\text{m}$ , is given by

$$z_r = \frac{\pi \omega_0^2}{\lambda} \quad (11)$$

where the Rayleigh range,  $z_r$ , is the distance in  $\mu\text{m}$  either side of the focus along the direction of propagation where the beam waist is no larger than  $\sqrt{2}$  times the waist at the focus, with  $\pi$ , the physical constant Pi,  $\omega_0$ , the beam waist in  $\mu\text{m}$  at the focus and  $\lambda$ , the wavelength of the light in  $\mu\text{m}$ .

The use of non-diffracting beams allows the creation of thin light sheets over a comparably large FOV up to 1 mm (Z. Yang *et al.*, 2014) with a light sheet thickness of less than 1  $\mu\text{m}$ . A ten-fold increase in light sheet FOV coverage over standard Gaussian light sheets has been reported (T. Vettenburg *et al.*, 2014), again up to an FOV of  $\sim 1$  mm. Compared to the

Mesolens, the total image size is still an order of magnitude smaller at similar lateral resolution. Furthermore, the reported non-diffracting beams have side lobes that require deconvolution of the raw data to remove their contribution. As briefly mentioned in the opening paragraph of this chapter, computational methods when used with Mesolens data have long computation times and require powerful hardware, and hence deconvolution methods may not be suitable for Mesolens datasets.

However, recently reported light sheet setups using non-diffracting beams could reach FOVs of up to 6.75 mm at a thickness of  $\sim 14.5 \mu\text{m}$  (J. Tang *et al.*, 2020). Hence LSM combined with non-diffracting beams has the potential for large FOV imaging at high spatiotemporal resolution on scales suitable for the Mesolens.

For the Mesolens, because of its unique combination of high NA and large FOV, it would not be possible to generate a Gaussian light sheet that has a long enough Rayleigh range to cover the full field of view at  $3 \mu\text{m}$  thickness. While non-diffracting beams could be used to generate thinner light sheets, at the point of writing this thesis no light sheet has been reported that covered  $\sim 6 \text{ mm}$  FOV at  $3 \mu\text{m}$  thickness.

The only method to cover such a large FOV with a thin sheet would be to scan the light sheet and acquire multiple images or use a rolling shutter as presented in recent work (T. J. Schröter *et al.*, 2012; K. M. Dean *et al.*, 2015; Q. Fu *et al.*, 2016). However, a camera detector with the necessary combination of small pixel size and high pixel number does not currently exist with a rolling shutter. As such, in this thesis only a static light sheet illuminator was explored.

## 1.6 Structured Illumination Microscopy

The basic principle of SIM is that a known, well-defined pattern of illumination, typically a grating, is projected into the sample. Superposition of two fine structures results in what is called Moiré fringes, which is a beating pattern where the spatial frequency depends on the structure of the two underlying patterns but is coarser by a factor of two than either of the underlying structures (M. G. L. Gustafsson, 2000). Therefore, if one of the fine structures, i.e. the grating structure, is close to the diffraction limited resolution of the microscope system and is known, by processing the resulting image, information of the other fine structure, i.e., the specimen, can be obtained. This results in an image that has two times better resolution than the diffraction-limited resolution. Figure 1.9 shows the basic principle of SIM resolution enhancement and the formation of the Moiré pattern from Gustafsson's original publication (M. G. L. Gustafsson, 2000). In this report, structured illumination was projected into the sample by placing a grating in a secondary image plane. The grating was then demagnified by the objective lens resulting in a sinusoidal illumination structure of the specimen. To completely extend the observable region of the microscope, the grating had to be translated through three phases, offset by  $\frac{2}{3}\pi$  ( $120^\circ$ ), for each of the three rotational positions ( $0^\circ, 60^\circ, 120^\circ$ ). Hence, nine images were recorded to obtain one final image at twice the diffraction limited resolution of the microscope system used. This concept was later extended to 3D structured illumination microscopy including mathematical derivations (M. G. L. Gustafsson *et al.*, 2008). In 3D SIM, additional phase-translated images were acquired at  $\frac{2}{5}\pi$  ( $72^\circ$ ) at three rotational positions. Thus, the total number of images required for 3D SIM was 15, yielding resolution doubling in both the lateral and axial dimensions.

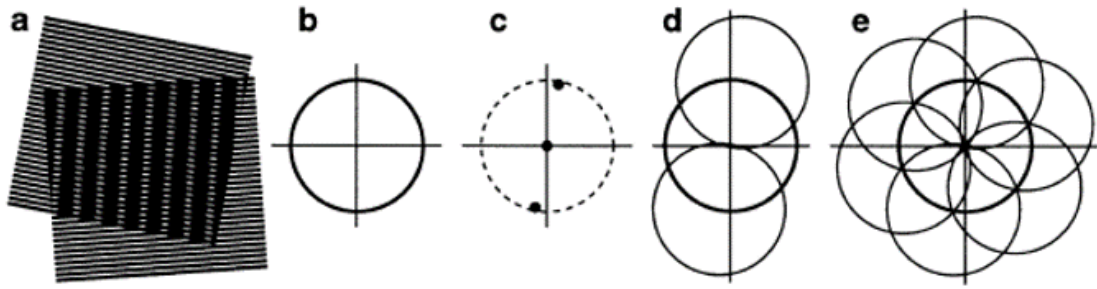


Figure 1.9: Principle of structured illumination microscopy (SIM) from (M. G. L. Gustafsson, 2000). (a) illustrates the formation of a Moiré pattern from two underlying fine structures. (b) depicts the observable region in reciprocal space of a given microscope system with the solid circle being the diffraction limited resolution and everything outside the circle not being resolved. (c) shows the Fourier components of a sinusoidal periodic illumination, i.e., a grating, projected into the specimen plane. In (d) the two offset circles show the regions from which additional information is moved into the observable region. Note that if the Fourier components (solid dots in (c)) are at the edge of the observable region, a resolution improvement by a factor of two is achievable. (e) illustrates how rotation and translation of the grating pattern incorporates spatial frequencies that are out of the diffraction limited bandwidth of the microscopy into the data essentially extending the observable region to a circle twice the original size.

The groundwork of SIM was laid by Gustafsson *et al.* (M. G. L. Gustafsson *et al.*, 1995). Originally he described and patented his work (M. G. L. Gustafsson *et al.*, 1997) as a method to increase the axial resolution of standard widefield microscopes, surpassing those of deconvolution and CLSM by using two objective lenses on opposite sides of the sample simultaneously. By illuminating and collecting light from the sample and letting the detection beams interfere constructively at the detector, effectively the collection angle and thus the numerical aperture was increased yielding higher resolution as suggested by equations (2) and (3). It was also shown (M. G. L. Gustafsson, 1999) that the axial resolution even surpassed the lateral resolution using this method. Furthermore, structured illumination provided access to otherwise inaccessible higher resolution information surpassing the diffraction limit (M. G. L. Gustafsson *et al.*, 1999). This concept was extended to lateral resolution (M. G. L. Gustafsson, 2000) and was later improved for axial resolution (M. G. L. Gustafsson *et al.*, 2008), overcoming the classical limit, set by Abbe over a century earlier, by a factor of two. Techniques that overcome the diffraction limit are referred to as super-resolution

microscopy. In Gustafsson's 2008 paper it was also shown that structured illumination could provide optically sectioned images. The disadvantage, however, was that nine individual images were necessary to fully benefit from this technique. This increase in image number resulted in higher photobleaching and photodamage to the specimen as well as increased acquisition time to obtain the final image. Further, the grating rotation and phase translations had to be precise and required accurate control as knowledge about the exact grating orientation was required for the post-processing steps.

A similar approach to Gustafsson's work was taken to achieve optical sectioning in widefield fluorescence microscopy by Neil *et al.* (M. A. A. Neil *et al.*, 1997, 1998). Structured light was introduced into a sample by projecting a physical grating structure (M. A. A. Neil *et al.*, 1997) at the focal plane and thus creating a fringe pattern (M. A. A. Neil *et al.*, 1998). If only optical sectioning was required without resolution improvement, it was possible to work with fewer images which in turn increased acquisition speed (D. Karadaglić, 2008; D. Karadaglić *et al.*, 2008). The optical sections could be created by comparing the images taken at different orientation of the structured illumination and only considering those spatial frequencies (in Fourier space) that changed, as those that remained the same were not modulated by the structured light and must hence be out of focus. An approach using dynamic speckle illumination (DSI) rather than a grid pattern showed that a speckle pattern can also be used as a structured light source with the same benefit as gratings (C. Ventalon *et al.*, 2005). The authors claimed that the speckle pattern was better suited to imaging of thick specimens as the contrast degradation occurring when fine gratings are projected into scattering tissue did not impact dynamic laser speckle as strongly. This technique has since been improved with regard to optical sectioning strength (C. Ventalon *et al.*, 2006, 2007). Figure 1.10 shows a simple representation of a DSI set-up, modified after (C. Ventalon *et al.*, 2005).



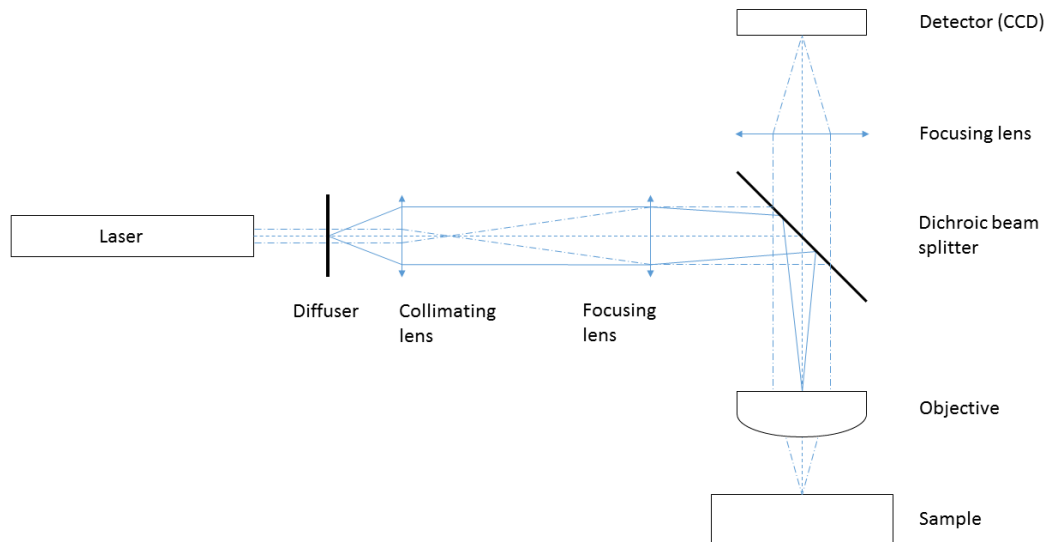


Figure 1.10: Set-up used for dynamic speckle illumination microscopy. The speckle pattern was imaged onto the back aperture plane of the objective, thus creating a speckled illumination of the sample. By then translating the speckle pattern one can observe a large variation in the in-focus fluorescence generated by the speckle grains and weak variation in the out-of-focus fluorescence, thus providing a measure of what region of the images were in focus and which were out of focus enabling an approach for optical sectioning (C. Ventalon *et al.*, 2005).

Simultaneously a technique has been developed (D. Lim *et al.*, 2008) that required only two images to obtain optical sections. This technique, called HiLo microscopy, is the subject of Chapter 2 and will be discussed in more detail there.

## 1.7 Mesoscopy

Optical mesoscopy is a field of imaging that combines FOVs of several millimetres with cellular resolution. This is an intermediate scale between macroscopic imaging on the centimetre scale which has significantly poorer resolution and optical microscopy which covers FOVs of few 10s of micrometres up to the millimetre or centimetre scale with resolution between  $\sim 200$  nm and a few micrometres. These boundaries have become increasingly blurred by advances in recent years, including the Mesolens system which will

be explored in more detail in Chapter 1.7. This section will briefly introduce the mesoscopy imaging techniques that are relevant to this work.

The mesoSPIM initiative (F. F. Voigt *et al.*, 2019) showed an approach for large volume imaging at high speeds by using a rolling shutter camera synchronised with a swept light sheet rather than a stationary one. This way, isotropic resolution could be achieved since the resulting swept light sheet could be focused thinner than a stationary sheet of the same size while the converging and diverging parts were blocked by the rolling shutter. However, very large FOV imaging required undersampling in the lateral dimensions due to the limited pixel number of commercially available digital cameras. The developers reported isotropic sampling at  $6.5\text{ }\mu\text{m}$  both laterally and axially in an imaging volume of  $1\text{ cm}^3$ . The mesoSPIM system allowed variable FOV between 2 and 21 mm via a zoom macroscope, thus the entirety of a large specimen could be imaged at low sampling and regions of interest could be imaged at high sampling in quick succession. However, the instrument cannot circumvent the limitation of the camera, therefore the large FOV cannot be combined with high spatial resolution sampling. The core strength of the mesoSPIM instrument lies in its capability to image large volumes with isotropic resolution fast due to the use of an electro tunable lens to scan the Gaussian beam forming the light sheet. Thus, it is possible to generate datasets of 12-16 GB in 7-8 minutes. Furthermore, the developers supplied a parts list and instructions on how to build and set up the system, thus making it easily accessible to the wider community.

Optical coherence microscopy (OCM) is an optical mesoscopy technique closely related to optical coherence tomography (OCT). Capable of micrometer resolution and imaging deep into tissue (D. Huang *et al.*, 1991; K. Karnowski *et al.*, 2017), this technique provided a label-free alternative to fluorescence imaging on comparable scales.

Optical projection tomography (OPT) achieved isotropic micrometer resolution of 8.75  $\mu\text{m}$  on millimeter scale FOV up to  $\sim 7$  mm (A. Liu *et al.*, 2019). The projection tomography approach used to achieve isotropic micrometer resolution is the main advantage of OPT over e.g., 'standard' LSM, however, mesoSPIM achieved isotropic resolution as mentioned above, at both higher resolution and larger FOV.

Another large FOV imaging technique recently presented (J. N. Stirman *et al.*, 2016; N. J. Sofroniew *et al.*, 2016) involved two-photon multi-region excitation and detection. However, the set-up was complex and, while providing a large FOV and long working distance, are two-photon point scanning systems. Thus, they are slow compared to widefield imaging techniques, although Stirman's method can perform calcium imaging at 30 frames per second, albeit at a much smaller FOV of  $\sim 1$  mm.

An example of a non-optical technique capable of imaging large specimens at high resolution using non-destructive approaches is X-ray computed tomography (CT). X-ray CT can reach sub-micron resolution with FOVs of  $\sim 1$  mm or several millimeter at lower resolution. The switch between high resolution and large FOV is achieved by changing the distance from x-ray source to object and object to detector (M. Töpperwien *et al.*, 2017). Thus, high resolution and large FOV are mutually exclusive in this setup. This approach combined phase-contrast with x-ray CT to achieve high contrast in both soft tissue and mineralised tissue. X-ray imaging can reach resolution as high as 20-50 nm, albeit at very small FOV of  $20 \times 40 \mu\text{m}^2$  (M. Bartels *et al.*, 2015).

In summary, the techniques presented here provide different approaches to mesoscale imaging each increasing either the FOV of classic microscopy to the realm of mesoscopic imaging or improving the resolution of mesoscopic imaging systems to bring it closer to the

microscale but are ultimately limited using standard detectors with large pixel size and/or objective lenses that inherently trade of resolving power for FOV and vice versa.

The Mesolens provides an alternative mesoscopic imaging approach by increasing the FOV without sacrificing resolution. The particulars of the Mesolens are covered in detail in the next section.

## 1.8 The Mesolens

The Mesolens is a novel objective lens for light microscopy that combines a large field of view with subcellular resolution (G. McConnell *et al.*, 2016). A large FOV is equivalent to a low magnification and current low magnification objectives have low numerical apertures and thus poor resolving power. Other approaches to large FOV with high resolving power involve acquisition of several images of neighbouring areas in a sample and then stitching and tiling them together. However, stitching and tiling generally results in a checker board pattern of lighter and darker tiles, degrading the image quality (F. B. Legesse *et al.*, 2015) even if sophisticated stitching algorithms are used. Furthermore, this approach takes significantly longer as the sample must be moved through several positions. Even though computer controlled moving stages are available, this is particularly problematic with live specimens. Not only would the specimen change over time on its own, but specimen drift can also be introduced by moving the stage. Lastly, high magnification lenses used for this kind of imaging have short working distances and are not suited to thick specimens.

The Mesolens overcomes the limitations of large FOV and NA by the sheer size of the optical components. This created several challenges. Every component needed to be custom built, including the frame as with elements of up to 63mm in diameter, the lens could not be fitted into standard microscopes (G. McConnell *et al.*, 2016). Currently, the Mesolens can be used in several imaging modes, namely confocal laser scanning, widefield epifluorescence, bright

field, and dark field illumination. As discussed in previous chapters, CLSM has excellent optical sectioning capabilities, however, the combination of the large FOV and high-resolution results in very long acquisition times. A full resolution (Nyquist sampled at 3.33 pixel per micron and z-step of 3 micron), full volume (6mm x 6mm x 3mm) 3D dataset with a pixel dwell time of 5  $\mu$ s would take 555 hours, or approximately 23 days, to acquire. Acquisition time is comparable to that of a stitching and tiling setup, however, there is no need for image alignment and the resulting image has uniform brightness (G. McConnell *et al.*, 2016).

The camera of the current Mesolens system uses a pixel-shifting mechanism where the detector chip is moved through 9 positions (a 3x3 grid) by two piezoelectric transducers. Images with over 250 million pixels are acquired this way by oversampling the sensor area. Naturally, a large FOV combined with high spatial resolution results in images with large file size. Large files are difficult to handle when using computational methods for post processing images, increasing computational cost to the point where algorithms might not be useable at all, or they take days to finish. Additionally, acquisition speed of the camera was limited to 0.5 fps. The full imaging volume of the Mesolens resulted in an image stack of 1000 slices with each slice being 500 MB in size totalling approximately 500 gigabytes (GB). This amount of data is impossible to process or analyse on standard desktop workstations and a dedicated server was procured for Mesolens data analysis (details in Chapter 2.2.3). The camera mode lacked optical sectioning but was very powerful to image prepared specimens of large specimens, like mouse embryo slices, as demonstrated (G. McConnell *et al.*, 2016).

Figure 1.11 shows the Mesolens prototype in detail, showing the complexity of the objective. The inset shows the number of optical components. Due to the large FOV, the optics had to be well corrected for astigmatism in addition to chromatic and spherical aberration (G. McConnell *et al.*, 2016). The Mesolens is a multi-immersion lens, using correction collars on

the lens barrel it could be corrected for imaging in water, glycerol, and oil. The excitation laser beam was expanded using a beam expander comprised of a  $f=-25$  mm lens (LC1054, Thorlabs) and a  $f=125$  mm lens (LA1986-A, Thorlabs) and focused by another  $f=50$  mm lens (LA1131-A, Thorlabs) into a periscope. An 80/30 beamsplitter (PBSW-532, Thorlabs) was used as the bottom mirror of the 1 m tall periscope and the top mirror (BB2-E02, Thorlabs) guided the beam into a large-aperture  $f=1000$  mm lens (LA1779-A-ML, Thorlabs) that filled the scanning mirrors with a collimated beam. The beam was guided into the scan lens by the mirrors and the Mesolens focused the beam into the specimen. Fluorescence emission was collected by the Mesolens and followed the same beam path as the excitation light back to the 80/30 beamsplitter, which was chosen to transmit 80% of the fluorescence signal (unpolarised) and reflect 30% of the linearly polarised excitation light. The signal after the beamsplitter passed through a  $f=75$  mm lens (LA608-A, Thorlabs) and was focused on the exit pinhole, set to one Airy unit, by the 10x objective lens (10 OA 25, Comar Optics). Lastly, the signal was detected using bandpass filters suitable for the fluorescent probe used and photomultiplier tubes (PMM02, Thorlabs, and P30-09 and P30-01, Senstech). Additional information is available in the 2016 paper (G. McConnell *et al.*, 2016)

Since the original work on the Mesolens prototype was published (G. McConnell *et al.*, 2016), a commercial Mesolens system was developed called the Mesolens MkII. The Mesolens MkII system also has a 0.47 NA albeit with a slightly shorter working distance of approximately 3 mm (for oil immersion). It is also corrected for aberrations in the visible range for three immersion media (water, glycerol, and oil) which the lens can be set for with three correction collars on the lens barrel. There are two Mesolens MkII systems in operation in our lab in addition to the prototype system. One of the Mesolens MkII is a camera only system, the other can be switched with a rotatable mirror between confocal laser scanning and camera. All results shown in this thesis were obtained with the MkII system that is equipped with the

camera only except for the confocal dataset in Figure 3.8, which was obtained with the prototype system as described in the original Mesolens publication (G. McConnell et al., 2016).

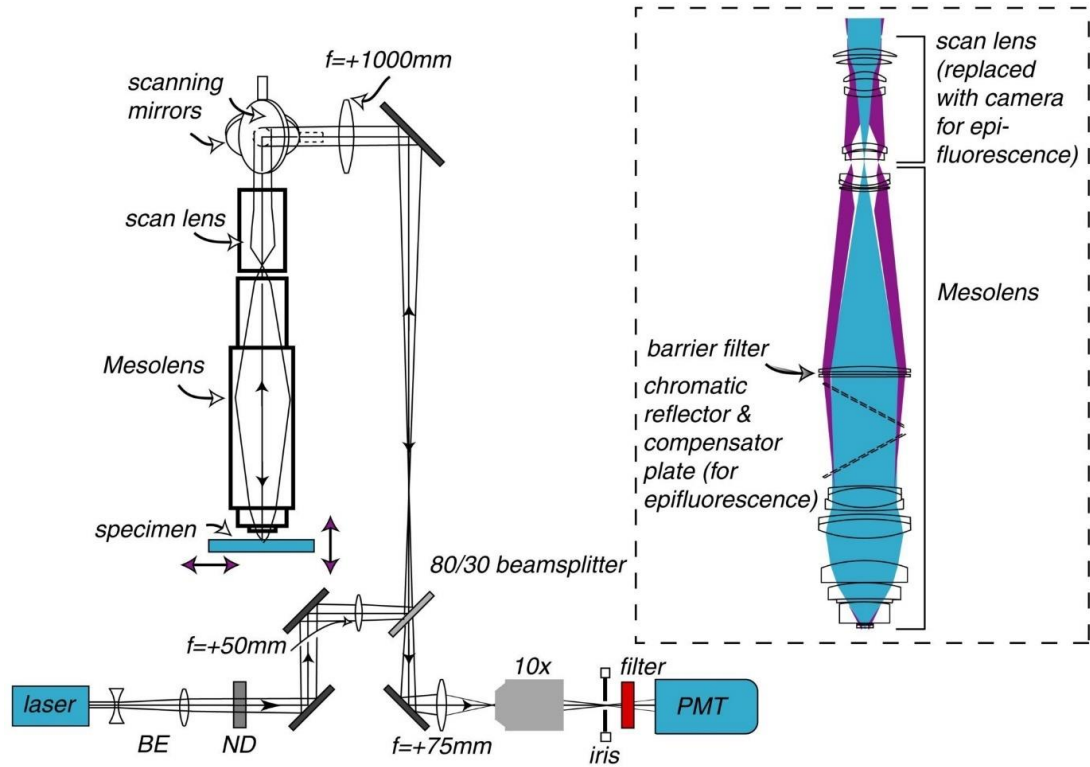


Figure 1.11: Detailed view of the Mesolens prototype objective lens. The setup for both laser scanning and widefield epifluorescence with a digital camera from (G. McConnell *et al.*, 2016) is shown detailing the optical path through the lens and the scanning mirrors for both excitation from the laser and detection with the photomultiplier tube (PMT). BE, a beam expander and ND, a neutral density filter. Inset shows the objective cross section. It should be noted that the lenses shown are actually lens groups comprised of several individual lens elements.

## 1.9 Thesis Outline

Chapter 2 shows the results of implementing the HiLo mesoscopy method with the Mesolens. It is a computational method capable of producing optical sections from two input images: one with uniform and one with structured illumination, in this case random laser speckle. The sectioning strength is on par with CLSM but acquisition speed of HiLo mesoscopy surpassed CLSM by an order of magnitude.

Chapter 3 shows the implementation of a Gaussian light sheet illuminator as well as attempts at building a two-photon excitation light sheet illuminator. Optical sectioning was achieved to the level that could be expected from the theory of Gaussian beam propagation resulting in reduction of out of-focus background fluorescence but with optical section thickness an order of magnitude larger than the Mesolens axial resolution. Acquisition speed was only limited by the camera framerate and the sample brightness.

Lastly in Chapter 4, it was attempted to perform blind-SIM deconvolution, a super-resolution technique that used structured illumination to achieve deconvolution with a 2-fold increase in lateral resolution. Although no resolution improvement could be observed when processing Mesolens data, the method produced optical sections on par with 2D deconvolution and CLSM and the lack of resolution improvement could be attributed to low illumination NA in the system.



## 2 HiLo Mesoscopy

### 2.1 Introduction

Widefield techniques capable of performing optical sectioning are highly sought after in biological imaging to reduce photodamage and photobleaching as well as increasing contrast (reduction of out-of-focus blur) at high acquisition speed.

The SDCM approach introduced in Chapter 1.4 represents a viable approach for high fps point scanning acquisition, however, the pixel shifting mechanism required to achieve Nyquist sampling on the Mesolens is not straightforward with a fast-spinning Nipkow disk used in SDCM. The disk would require as many perforations as the final image had pixels and must be large enough to support the perforations. This would be mechanically challenging, if not impossible.

An alternative wide field optical sectioning method is widefield two-photon microscopy (W2PM). W2PM has been reported for *in vivo* imaging (J. Y. Hwang *et al.*, 2011) and has been shown to produce less photobleaching than single-photon excitation without the need to scan the beam over the field of view, capable of reaching 100 fps acquisition speed (R. Amor *et al.*, 2016). W2PM can perform optical sectioning when the peak intensity of the excitation beam is high in the focal plane only using temporal focusing (D. Oron *et al.*, 2005; E. Y. S. Yew *et al.*, 2013). Temporal focusing is achieved by introducing a scattering plate into the beam path of the excitation beam at a position such that the difference in path length travelled for individual light paths results in a longer pulse duration everywhere except the focal plane of the objective lens. Thus, the high peak intensity necessary for two-photon excitation is reached only at the focal plane resulting in an optically sectioned image. However, W2PM

would require very high peak intensity radiation propagating through the Mesolens to excite fluorescent molecules at the specimen across the entire FOV, and this would potentially damage the optical elements.

As mentioned in Chapter 1.6, structured illumination microscopy is a super-resolution imaging technique that inherently provides optical sectioning as it only regards modulated, in-focus signal for the final image (M. G. L. Gustafsson *et al.*, 1997; M. G. L. Gustafsson, 2000). SIM is discussed in more detail in Chapter 4.1.2 together with other common SR microscopy techniques.

A related method called HiLo microscopy (“Hi” and “Lo” representing the high and low spatial frequency components, not to be confused with HILO, highly inclined and laminated optical sheet) has been developed (D. Lim *et al.*, 2008) which makes use of the optical sectioning capability of SIM without any super-resolution content. Only two images are required for HiLo microscopy, which can reduce phototoxicity and photobleaching effects (F. Orieux *et al.*, 2012; F. Ströhl *et al.*, 2017) as opposed to three images for optical sectioning SIM (M. A. A. Neil *et al.*, 1997) or at least 4 images for 2D super-resolution SIM techniques (F. Ströhl *et al.*, 2017).

The two images required are one uniformly illuminated image and one with structured illumination. By using the difference image, i.e., speckle illumination minus uniform illumination image, a weighting function is generated which is used on the uniformly illuminated image and applying a low-pass filter to the Fourier transformed digital image, the in-focus low spatial frequency signal is acquired. The high-frequency in-focus signal is obtained by applying a high-pass filter to the image of the uniformly illuminated specimen. The high and low frequency in-focus information is combined, and a final image is obtained

that contains the full spatial frequency spectrum of only the in-focus signal. For a detailed theory of HiLo imaging see Chapter 2.2.1.

The optical sectioning strength of HiLo has been reported to be comparable to CLSM while the acquisition speed is only limited by the camera framerate (D. Lim *et al.*, 2011). The HiLo method can be implemented inexpensively by using a diffuser to create laser speckle with coherent (laser) light or with a grating and incoherent light. This diffuser-based method of generating laser speckle has been reported to be more robust than using a grating when imaging thick specimens because speckle illumination is random in nature and less affected by scattering effects in thick specimens (D. Lim *et al.*, 2011). Furthermore, the speckle size can be easily adjusted by changing the diameter of the beam incident on the diffuser to suit different specimens (J. Mazzaferri *et al.*, 2011).

HiLo is fast and robust. It has made widefield microscopy an excellent alternative to confocal microscopy by providing comparable optical sectioning strength at higher acquisition speeds as no point scanning is required. This has been shown with live specimens (D. Lim *et al.*, 2011), requiring a wide FOV and fast acquisition speed with optical sectioning comparable to commercially available confocal microscopes. Moreover, there are fundamentally no obstacles to applying HiLo with the Mesolens.

HiLo imaging has recently been used in calcium imaging to observe neuronal activity (M. A. Lauterbach *et al.*, 2015). The authors performed imaging at speeds of up to 100 frames per second, and deep into the tissue specimens without damage. Furthermore, HiLo has been combined with LSM (J. Mertz *et al.*, 2010) to enhance the optical sectioning strength of LSM imaging of the whole mouse brain and more recently to improve three dimensional reconstruction in thick tissue imaging (D. Bhattacharya *et al.*, 2012) in what the authors call '3D HiLo'.

HiLo microscopy in transmission illumination with laser speckle illumination was chosen with the Mesolens to obtain optical sections and sectioning strength, quality and speed compared to CLSM (J. Schniete *et al.*, 2018) was investigated.

## 2.2 Methods

### 2.2.1 Theoretical background of Hilo microscopy

HiLo microscopy was described in detail by its developers Lim and Mertz (D. Lim *et al.*, 2008, 2011), including a mathematical derivation of its optical sectioning strength for the interested reader, therefore I repeat only the basic principles of its operation here that are necessary to reproduce my results.

HiLo microscopy performs optical sectioning of fluorescent samples by segmenting the image using contrast evaluation of the difference image of a structured illumination image and a uniform illumination image and obtaining a weighting function as a result. The uniform image  $i_u$  is a simple widefield fluorescent image. To obtain the structured illumination image  $i_s$ , the sample is illuminated by a random laser speckle pattern. The in-focus high spatial frequencies of the image are obtained by simply applying a Gaussian high-pass filter to a Fourier transformed uniform image such that:

$$i_{HP} = \mathcal{F}^{-1}(\mathcal{J}_u \times HP), \quad (12)$$

where  $i_{HP}$  is the high-pass filtered uniform image,  $\mathcal{F}^{-1}$  is the inverse Fourier Transform,  $\mathcal{J}_u$  is the Fourier Transform of  $i_u$  and HP is a Gaussian high-pass filter with cut-off frequency  $k_c$ , such that  $HP(k_c) = 1/2$ .

The high spatial frequencies are inherently in focus and thus do not need to be further processed. To obtain the in-focus low spatial frequencies, first the difference image,  $i_d$ , must be calculated

$$i_d = i_s - i_u. \quad (13)$$

Subtracting  $i_u$ , the uniform illumination image, from  $i_s$ , the speckle illumination image, removed the sample induced bias and allowed the evaluation of local speckle contrast to be performed on the variations of the speckle pattern only. The resulting difference image is rescaled to have values strictly larger than one to avoid local mean values close to zero which would generate computational problems when the local contrast is evaluated using equation (15), i.e., values can become very large due to the division by very small numbers rendering the resulting weighting function useless. Furthermore, it must be taken care that images were in a format that did not clip high or low values before subtracting, e.g. convert to floating point first.

The local contrast of speckle grains tended to zero with defocus and thus allowed to distinguish between in-focus and out-of-focus signal. This decay to zero can be accelerated by applying a bandpass filter to  $i_d$  prior to contrast evaluation

$$BP = \exp\left(-\frac{k^2}{4\sigma^2}\right) - \exp\left(-\frac{k^2}{2\sigma^2}\right), \quad (14)$$

where BP is the bandpass filter, generated by subtracting two Gaussian lowpass filters,  $k$  is the spatial frequency and  $\sigma$  is the bandpass filter standard deviation.

Correct evaluation of local speckle contrast is key to separate in-focus from out-of-focus signal. Local contrast evaluation can be performed by calculating the quotient of standard deviation and mean in a local neighbourhood with a sliding window (D. D. Duncan *et al.*, 2008; J. Mazzaferri *et al.*, 2011).

$$C_{\langle\Lambda\rangle} = \frac{sd_{\langle\Lambda\rangle}}{\mu_{\langle\Lambda\rangle}}. \quad (15)$$

where  $C_{\langle\Lambda\rangle}$  is the contrast in the local neighbourhood, evaluated within a sliding window of side length  $\Lambda$  (pixels).  $sd_{\langle\Lambda\rangle}$  and  $\mu_{\langle\Lambda\rangle}$  are the standard deviation and mean intensity in the local neighbourhood respectively.

The side length  $\Lambda$  of the sliding window is determined depending on the cut-off frequency  $k_c$  as described in literature (J. Mazzaferri *et al.*, 2011).

$$\Lambda = \frac{1}{2k_c} \quad (16)$$

By applying a Gaussian low-pass filter LP complementary to HP, i.e.  $LP + HP = 1$ , low spatial frequencies are obtained from the uniform illumination

$$i_{su} = \mathcal{F}^{-1}(J_u \times LP), \quad (17)$$

where  $i_{su}$  is the low spatial frequency image,  $J_u$  is the Fourier Transform of  $i_u$  and LP is the complementary low-pass filter.

Applying the local contrast as a weighting function to  $i_{su}$  resulted in an image of in-focus low spatial frequencies.

$$i_{LP} = i_{su} \times C_{\langle\Lambda\rangle}, \quad (18)$$

where  $i_{LP}$  is the weighted, low-pass filtered uniform illumination image.

To ensure a smooth transition between  $i_{LP}$  and  $i_{HP}$ , a scaling factor is calculated

$$\eta = J_{HP}(k_c) / J_{LP}(k_c), \quad (19)$$

where  $\eta$  is the scaling factor,  $J_{HP}(k_c)$  and  $J_{LP}(k_c)$  are the Fourier Transforms of  $i_{HP}$  and  $i_{LP}$  respectively evaluated at the cut-off frequency  $k_c$ .

The final optically sectioned HiLo image was obtained by adding the in-focus high and low spatial frequency images together

$$i_{HiLo} = i_{HP} + \eta * i_{LP} \quad (20)$$

where  $i_{\text{HILo}}$  is the final optically sectioned image. By setting  $k_c=0.18\sigma$  (D. Lim *et al.*, 2011; J. Mazzaferri *et al.*, 2011), the optical sectioning strength can be controlled by changing only the  $\sigma$  parameter.

### 2.2.2 Experimental setup

A schematic of the setup is shown in Figure 2.1. A Coherent Sapphire 488-10 CDRH laser (Coherent, UK) was used as a light source. The beam was guided through a variable beam expander (Thorlabs BE02-05, 2x-5x variable zoom Galilean beam expander), increasing the FWHM beam diameter from 1 mm to a minimum of 2mm and a maximum of 5 mm. The final beam diameter resulted in coarse speckle (beam expander set 2x) with higher contrast in thick specimens at the cost of optical sectioning strength or fine speckle (beam expander set to 5x), allowing thin sectioning but contrast degradation in thick samples as described in Chapter 2.3. Subsequently the beam illuminated a 1500 grit ground glass diffuser (DG20-1500, Thorlabs). The diffuser was glued to a DC motor controlled via an Arduino Uno board connected to a PC via USB. It was imaged onto the back aperture of the 0.6 NA Mesolens condenser (Mesolens Ltd.) using an aspheric lens with 0.6 NA (ACL5040U-A, Thorlabs). With the diffuser stationary, a speckle pattern was generated in the sample. Rotating the diffuser via the DC motor (6 V, 12000 $\pm$ 15% rpm) resulted in uniform illumination, thus allowing acquisition of both uniform and speckle illumination images at 30 seconds acquisition time per image pair on the full 4.4 x 2.9 mm<sup>2</sup> FOV of the Mesolens. The 30 seconds included saving images to disk as well as the time required for the motor to reach full speed and full stop again. Images were acquired with a thermoelectric Peltier cooled camera (VNP-29MC, Vieworks) with a chip-shifting mechanism. The chip-shifting mechanism was essential to benefit from the large FOV and high resolution (700 nm lateral, 7  $\mu$ m axial (G. McConnell *et al.*, 2016)) provided by the Mesolens. The camera port on the Mesolens system contained a

focusing lens providing an additional magnification of 2x bringing the total system magnification to 8x. The Mesolens system was also equipped with a multiband barrier emission filter. The technical specifications of the Mesolens system have been published elsewhere (G. McConnell *et al.*, 2016) and brief details of the key features of the setup are provided in Chapter 1.8. The camera had a chip-shifting mechanism to increase the sampling rate by moving the detector chip by a distance equal to a fraction of a pixel (one third of a pixel for 3x3 chip-shifting or half a pixel for 2x2 chip-shifting). The camera could be operated without chip-shift at a resolution of 6576 x 4384 pixels (28.8 Megapixel), with 2x2 chip-shift at 13152 x 8768 pixels (115.3 Megapixel) and with 3x3 chip-shift at 19728 x 13152 pixels (259.5 Megapixel).



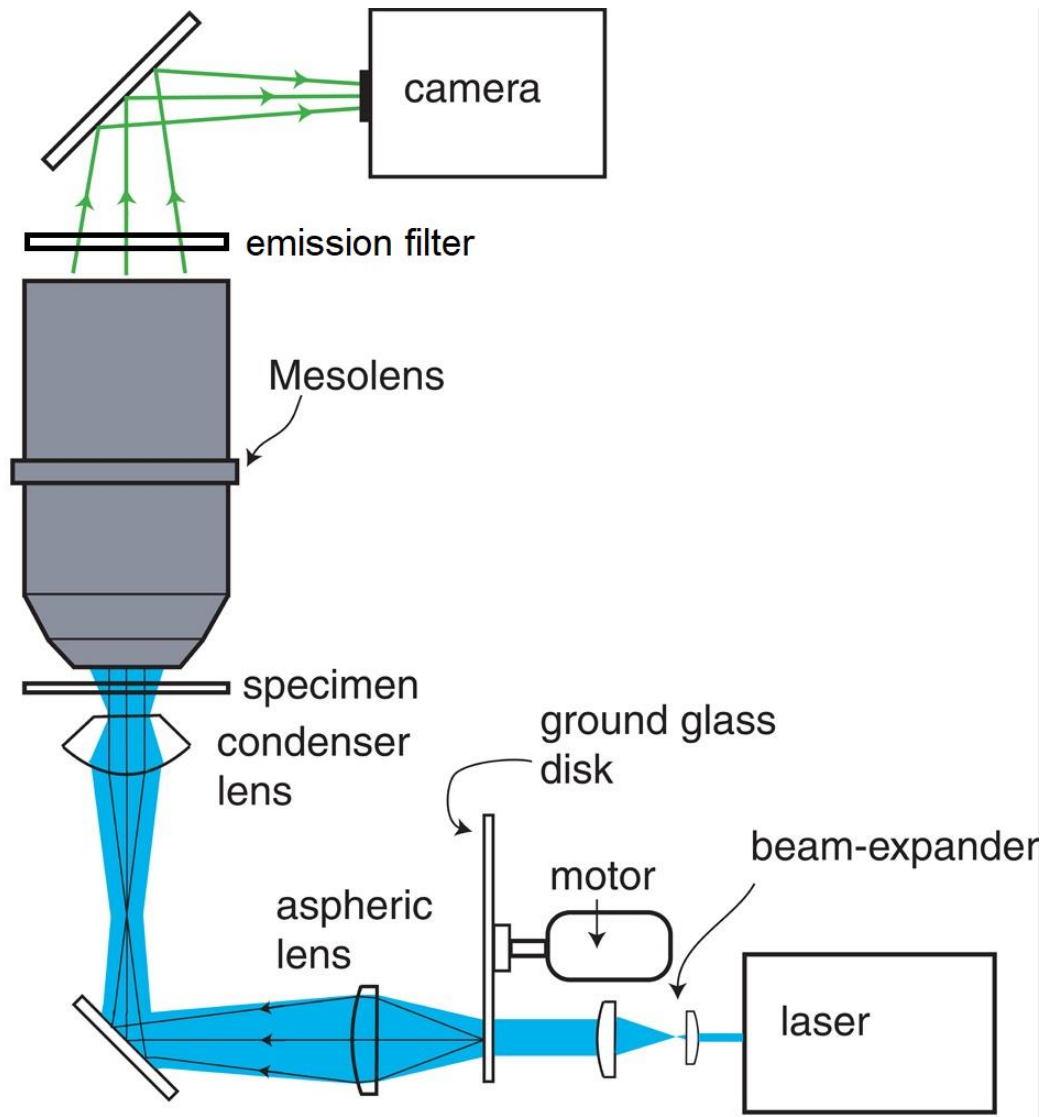


Figure 2.1: Experimental setup to generate speckle and uniform illumination. The laser emitted light at 488 nm at 4 mW peak power at the sample. The beam was expanded to a maximum diameter of 5 mm and illuminated the 1500 grit ground glass diffuser. The diffuser was imaged by the 0.6 NA aspheric lens onto the back aperture of the Mesolens condenser. A stationary diffuser resulted in speckle illumination of the sample while a rotating diffuser illuminated the sample uniformly. The sample was then imaged by the Mesolens onto a camera detector. The triple band emission filter was part of the commercial Mesolens system and transmitted light at  $470\pm 10$  nm,  $540\pm 10$  nm and  $645\pm 50$  nm. Not shown in this diagram are two mirrors that are placed before and after the beam expander to guide the laser beam.

For HiLo imaging with the Mesolens, the chosen mode was always 9x chip-shift for acquisition of images with the highest possible resolution. In this mode, the sampling rate was 4.46 px/ $\mu\text{m}$ , corresponding to a 224 nm pixel size, satisfying Nyquist sampling. The sampling rate

of the image was determined by imaging a 1 mm graticule (Graticule Ltd., Tonbridge, England) and equating the known distance in  $\mu\text{m}$  to a distance in pixels in ImageJ (J. Schindelin *et al.*, 2012). The minimum frame time of the VNP-29MC camera was 200 ms resulting in acquisition time for one full FOV image with 9x pixel shift of 1800 ms excluding time to transfer the image data from the camera to the PC which usually took on the order of 10 seconds. In practice, acquisition of one image took 12-15 seconds, including transfer of data and beginning of new image capture.

### 2.2.3 Data processing

To process the speckle and uniform images, a MATLAB (R2016b version 9.1.0.441655, 64bit, MathWorks, Inc.) script was written that performed HiLo imaging in the same manner as described in Chapter 2.2.1. This allowed more control over individual parameters compared to using the existing ImageJ plugin (optical sectioning factor, low frequency scaling and cut-off frequency) and opened the possibility to use the 'Parallel Processing Toolbox' of MATLAB to use a graphics processing unit (GPU) for processing. Two versions of the script were used: One used the 'Parallel Processing Toolbox' of MATLAB processing partially on the GPU. This was only possible with small images due to the memory limitation of the graphics card. The other version did not use the GPU but could process the full FOV Mesolens data. The non-GPU and GPU versions can be found in the Appendix 8.1 and 8.2 respectively. User-made functions were used to generate the low pass, high pass, and band pass filters. These can be found in Appendices 8.3.1, 8.3.2 and 8.3.3.

Because of the large file size of Mesolens images, it was necessary to process z-stacks of specimens on a server as the memory required to open and process such large files is on the order of 100s of GB, typically not available on Desktop PCs. The server used was a Dell PowerEdge R740 with 1TB RAM and an NVIDIA Quadro P4000 GPU with 8GB video memory.

## 2.2.4 Measuring the optical sectioning strength of the HiLo mesoscope

To determine the optical sectioning strength of the HiLo method, a thin fluorescent layer (R. Amor *et al.*, 2015) was set at a tilt by wedging a microscope slide under one end of the specimen microscope slide, thus a known height difference between the two ends of the specimen slide was introduced. The resulting image then showed the fluorescent layer as a narrow strip as shown in Figure 2.2b and Figure 2.2c, coming into focus in the centre of the field of view and going out of focus towards the left and right. Since the length of the sample slide is also known, a measured FWHM in the lateral direction can be translated into an axial FWHM, thus giving an experimental measure of the optical section thickness. This method was adapted from existing literature (W. B. Amos *et al.*, 2011).

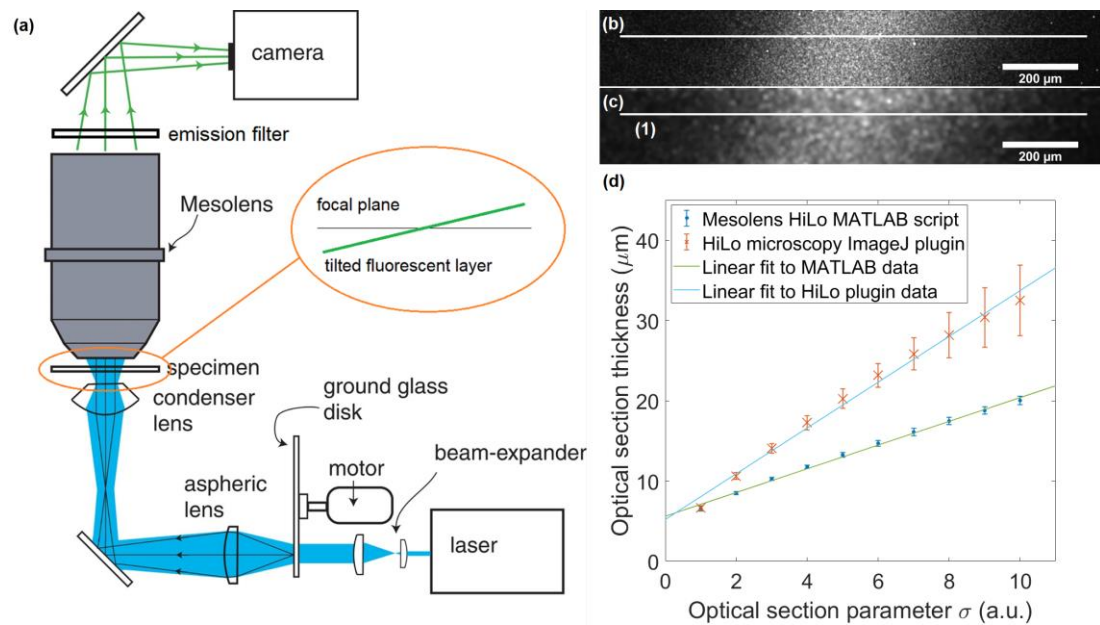


Figure 2.2: Comparison of optical sectioning strength. A tilted layer of fluorescent dye was processed with the HiLo ImageJ plugin and the MATLAB script. (a) shows the experimental setup depicting the fluorescent layer tilt in the inset. The tilt is exaggerated to make clear that only a narrow strip in the centre was in focus. An example of the HiLo processed layer is shown for (b) the plugin and (c) the MATLAB script with the optical sectioning parameter  $\sigma$  set to 1 for both processing modalities which corresponded to approximately the same optical section thickness. The thickness as a function of  $\sigma$  (d) was obtained by processing the same data of the tilted fluorescent layer with the plugin and the MATLAB script and calculating the average full width at half-maximum (FWHM) of Gaussian fits to five horizontal intensity line plots through the processed images. The  $\sigma$ -value in (d) is

the same as in equation (14) which controls most parameters in the algorithm. (1) in (c) shows an example of such a horizontal line plot, the line is made thicker to ease visualisation but was only one pixel thick for the measurement. The two processing modalities reached a minimum section thickness of  $6.6 \pm 0.3 \mu\text{m}$  (plugin) and  $5.2 \pm 0.3 \mu\text{m}$  (MATLAB) at the lowest setting for  $\sigma$ . The difference in optical section thickness between the ImageJ plugin and the MATLAB script is due to different scaling of the  $\sigma$  parameter in the MATLAB script compared to the HiLo ImageJ plugin. The graininess is an example of artefacts that can occur when speckle structure translated through to the final image. This could be avoided in thicker samples or by setting  $\sigma$  to higher values, i.e., thicker optical sections.

To prepare the thin fluorescent layer, first a  $170 \mu\text{m}$  thick microscope cover slip (22 mm x 22 mm, #1.5, Thermo Fisher Scientific) was rinsed in dry acetone (Acetone 20066.330, VWR Chemicals). It was then submerged in an APTMS-acetone (3-Aminopropyltrimethoxysilane, 281778-100ML, Sigma Aldrich) solution for six hours (0.2 mL APTMS, 9.8 mL of dry acetone). After this period, the cover slip was rinsed three times in dry acetone and blow-dried with compressed air. The cover slip was put in a  $10 \mu\text{M}$  solution of fluorescein salt (Fluorescein sodium salt, 46960-25G-F, Sigma Aldrich) in distilled water. Care was taken to only let one side of the cover slip get in contact with the fluorescein solution to avoid having two thin fluorescent layers (one on either side). The bath was carefully wrapped in aluminium foil and left overnight in a dark place. The next day, the cover slip was rinsed with distilled water twice and again blow-dried with compressed air. Finally, the cover slip was mounted on a microscope slide with the dye-coated surface in contact with the slide and was sealed with nail varnish. Imaging was done with glycerol immersion.

### 2.2.5 Mouse hippocampal neuron specimen preparation

The mouse hippocampal neuron specimen was prepared from C57BL/6J pups (1-2 days old) by Dr Aimée Franssen as described previously (K. McNair *et al.*, 2006; J. Gan *et al.*, 2011) and fluorescently stained (N. Z. Abdul Rahman *et al.*, 2016; L. Ritchie *et al.*, 2018). All experimental procedures were performed in accordance with UK legislation including the Animals (Scientific Procedures) Act 1986 and with approval of the University of Strathclyde Animal

Welfare and Ethical Review Body (AWERB). In short, neurons were fixed in ice-cold 4% paraformaldehyde (PFA). The sample was then incubated with a primary anti-mouse antibody (anti- $\beta$ III-tubulin (1:500), Sigma-Aldrich) and fluorescently labelled using a secondary antibody (anti-rabbit AlexaFluor 488 (1:200), Thermo Fisher Scientific). The fixed and stained sample was mounted onto a glass microscope slide (VWR, UK) using Vectashield mounting medium (H-1200, Vector Laboratories) and imaging was performed with glycerol immersion on the Mesolens.

#### 2.2.6 5-day-old zebrafish larva specimen preparation

The zebrafish specimens were prepared by Dr W.B. Amos. The zebrafish were fixed in ethanol: glacial acetic acid at a 3:1 ratio at 4°C for 72 hours, then washed in 100% ethanol and rehydrated by passing them through a series of ethanol/water mixture containing 90%, 75% and 50% ethanol (10 minutes in each) before washing in phosphate-buffered saline (PBS) and transferring to 0.001% (w/v) acridine orange (A1301, Thermo Fisher Scientific) in PBS until strongly coloured (30 minutes). The larvae were then washed gently in PBS for 30 min to remove excess stain before dehydration in the same series of ethanol solutions used in reverse for 5 minutes each. The dehydrated specimens were washed three times in absolute ethanol (dried with molecular sieve) and then transferred via xylene, changed twice, and left in xylene for two hours and checked for transparency. They were tumbled gently overnight in a solution Fluoromount (E. Gurr, 1951) (Fluoromount is no longer available commercially: it is recommended to use Histomount (Thermo Fisher Scientific) as similar substitute) before mounting in a single-cavity slide under a standard coverslip, with the specimen left uncovered to facilitate the evaporation of the xylene solvent and more mountant being added to reduce shrinkage. Imaging was performed with glycerol immersion on the Mesolens.

### 2.2.7 Pollen grain specimen preparation

The *Taraxacum* pollen specimen was prepared by Prof Gail McConnell.

To obtain the pollen grains, first the florets were removed from the flower heads of dandelion (*Taraxacum*) which were then stored in glacial acetic acid. Pollen grains were released from the florets by vigorously stirring the suspension, sieving out large particles and then centrifuging at 3000 rpm in 50 ml tubes. Afterwards pollen grains could be extracted from the pellet. The pollen grains were resuspended twice in distilled water and then resuspended again in 10% sodium hydroxide (NaOH) in glass centrifuge tubes. After stirring with a glass rod to disperse the pellet, the tubes were heated to 90°C for several minutes. Afterwards, 30-40 ml of distilled water was added to each tube and placed in the centrifuge again. This water wash was repeated twice after which the pollen pellet was resuspended in a 9:1 (by volume) mixture of acetic anhydride and concentrated sulphuric acid and heated to 90°C again for 5 minutes. Then the pellet resuspended and centrifuged in distilled water three times.

Lastly, the pollen grains were dehydrated in ethanol, passed into xylene, and finally mounted on a cover slip in Fluoromount (Fisher Scientific). This method produces a high concentration of pollen grains in a thin layer between cover slip and glass plate that are strongly autofluorescent. The pollen grains can be excited with UV, blue and green light and emit strongly in the red.

### 2.2.8 *Daphnia magna* (waterflea) specimen preparation

The *Daphnia magna* specimen was prepared by Dr W.B. Amos as follows.

Live cultures *Daphnia magna* were obtained from a commercial source, supplying aquarists, rinsed clear of debris, and killed in 50% ethanol. They were then stored in 70% ethanol for

days or weeks until needed. They were stained in 0.5% eosin Y (alcohol and water soluble) (Fisher Scientific) in 70% ethanol and stored in darkness for days or months until required. The specimens were destained in several changes of 70% ethanol until they appeared pink and transparent rather than bright red and then dehydrated in a series of ethanol solutions, with two changes of absolute ethanol followed by two changes of xylene. The stain is totally insoluble in xylene. They were then transferred to capped vials with a viscous solution of hydrophobic resin (Gurr's Fluoromount) and allowed to sink, over several hours, to the bottom of the vial, after which they were picked out individually with a wide-mouthed glass pipette and placed on cavity slides and kept warm on a hotplate for a day or two, so that the xylene solvent could evaporate off. More Fluoromount was added repeatedly until the mountant surface remained slightly convex. More mountant and a coverslip were added and an M8 steel nut was placed on top of the coverslip as a weight so that excess mountant was pressed out from under the coverslip to the sides over a period of hours and the beads of excess mountant were trimmed away with a scalpel when hardened.

## 2.3 Results

### 2.3.1 HiLo mesoscopy optical section thickness

To obtain a measure of the optical sectioning strength of the HiLo mesoscopy method, a thin layer of fluorescent dye on a coverslip was imaged while tilted with respect to the image plane of the Mesolens.

Imaging the coverslip at a tilt achieved that the fluorescent dye was in focus in the centre of the field of view and went out of focus towards the sides of the image. With a known tilt angle and thus a known z-height difference across the width of the image, the section

thickness was calculated. Gaussian curves were fitted to five intensity plots through the processed images and the average was taken to obtain the full width at half maximum (FWHM) as a measure of the section thickness.

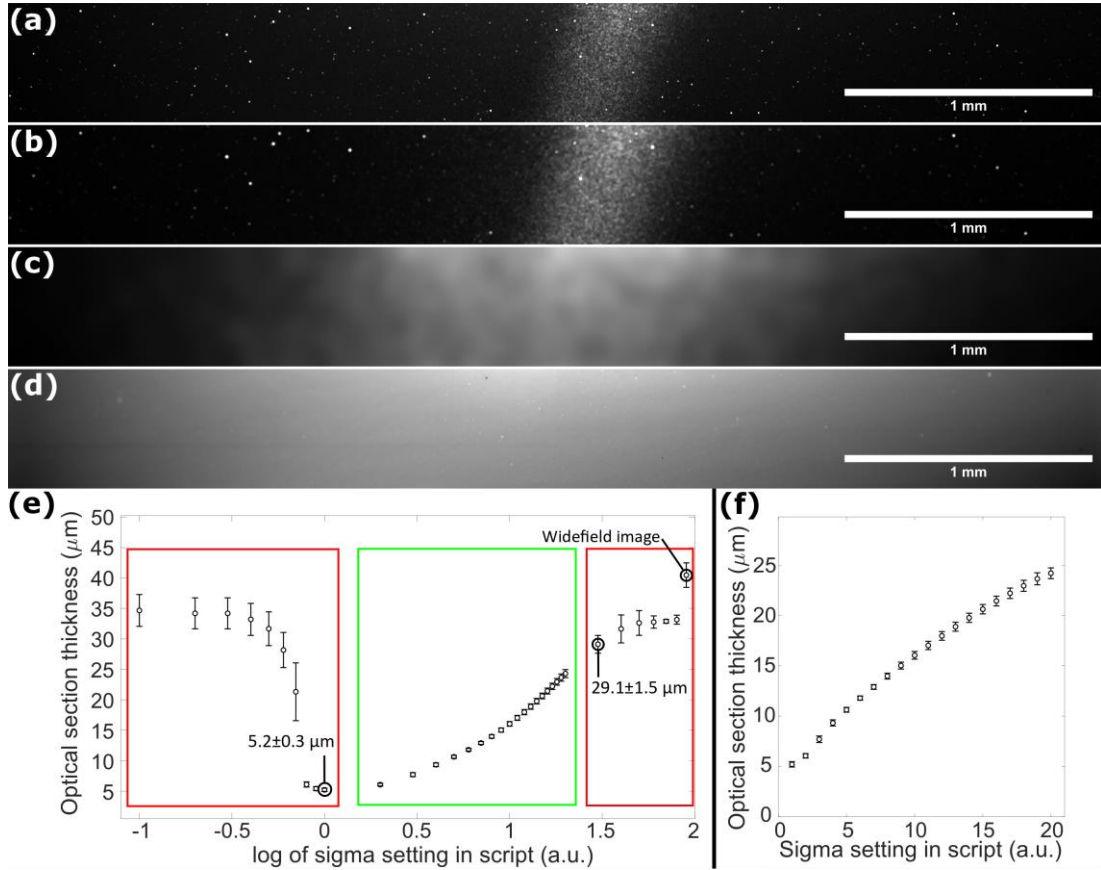


Figure 2.3: HiLo mesoscopy sectioning strength. (a)-(c) are HiLo processed images of thin layer of fluorescent dye tilted at an angle of  $1.28^\circ$  as described in Chapter 2.2.4 with measured average full width at half maximum of  $5.2 \pm 0.3 \mu\text{m}$  with sigma equal to 1,  $6.1 \pm 0.2 \mu\text{m}$  with sigma equal to 2 and  $29.1 \pm 1.5 \mu\text{m}$  with sigma equal to 21 respectively, (d) is the widefield image and (e) is a measure of the resulting optical section thickness across a wide range of sigma values in the script. X-axis is on a log scale to better visualise each datapoint. The low values for sigma resulted in contrast evaluation masks that are too small to contain enough imaged speckle to accurately measure the contrast of said speckle (left-hand red box). For high values of sigma, the sectioning curve flattened off and slowly approached the measured thickness of the widefield image corresponding to no sectioning (right-hand red box). The script was adapted to have user inputs for sigma between 1 and 20 (a.u.) to cover the meaningful section thickness range (centre green box) resulting in the plot shown in (f).

Figure 2.3 shows the result of HiLo processing the images taken of the tilted fluorescent layer and quantification of the section thickness. Section thickness was on par with confocal laser



scanning microscopy. However, CLSM had an acquisition speed of approximately 5 minutes for a single frame of the full FOV, while the camera offered an acquisition speed of approximately 10 seconds corresponding to 30 times faster than CLSM, including saving the file to the computer hard drive. The minimum section thickness was  $5.2 \pm 0.3 \mu\text{m}$ . It could be seen, that below the section thickness parameter value corresponding to  $5.2 \pm 0.2 \mu\text{m}$ , the curve flattened off and for mask sizes that did not include sufficiently many speckle grains to accurately determine local contrast, proper Gaussian fits became impossible and the optical section measurements became meaningless (Figure 2.3e, left-hand red box). Similarly, for section parameter values corresponding to  $29.1 \pm 1.5 \mu\text{m}$  and larger, the curve flattened and eventually approached the same measured thickness as the widefield image corresponding to no optical sectioning (Figure 2.3e, right-hand red box). The sigma value in the script was thus scaled to the values corresponding to the meaningful range (green box in Figure 2.3e) including the value corresponding to  $5.2 \pm 0.3 \mu\text{m}$  as the base line when sigma was set to 1 such that increasing sigma in integer steps of 1 between 1 and 20 resulted in the plot in Figure 2.3f. In terms of spatial frequency, the smallest possible value for sigma would correspond to  $2.08 \mu\text{m}^{-1}$  because that is the spatial frequency present in the digital image corresponding to the length of two pixels which is the maximum spatial frequency that a digital image can include. However, the above-mentioned rescaling was necessary because the minimum achievable speckle size was on the order of  $8 \mu\text{m}$  making the afore-mentioned minimum spatial frequency unusable for the filters described in Chapter 2.2.1., After re-scaling, the spatial frequency corresponding to sigma equal to 2 was one fifth of that frequency, i.e.,  $0.41 \mu\text{m}^{-1}$ . Increasing sigma in integer values divided the corresponding spatial frequency by a factor of five each time, i.e., for sigma equal to 3, the corresponding spatial frequency was  $0.08 \mu\text{m}^{-1}$  and so on.

### 2.3.2 Pollen grain imaging with HiLo mesoscopy

Specimens were imaged and processed with values for sigma and beam diameter incident on the diffuser resulting in coarser or finer speckle pattern depending on the specimen thickness. The optimal section thickness parameter depended primarily on the specimen thickness as speckle contrast degraded in thick specimens like the *Daphnia*. Whereas thin specimens like the pollen grains had high contrast speckle illumination. Figure 2.4 shows a comparison between the *Daphnia* and pollen grain sample to illustrate how the unprocessed raw data looks with both fine and coarse speckle illumination. The *Daphnia* specimen in Figure 2.4a was illuminated with a fine speckle pattern, however, the pattern cannot be seen due to the dense labelling and thickness of the specimen. Figure 2.4b shows the same specimen with coarse speckle. The illumination pattern is clearly visible which is the desired effect for the HiLo process to generate the weighting function from the difference image. The value of sigma must be chosen according to the speckle size, in the case of the *Daphnia* specimen, sigma was 4, corresponding to a spatial frequency of  $0.016 \mu\text{m}^{-1}$ . This increased the size of the sampling window for the local speckle contrast evaluation to  $\sim 60 \mu\text{m}$ , thus ensuring that multiple speckle grains were inside the evaluation kernel. The pollen grain in Figure 2.4c was uniformly illuminated and the image in Figure 2.4d was with fine speckle illumination. This specimen could be processed with sigma set to 2.

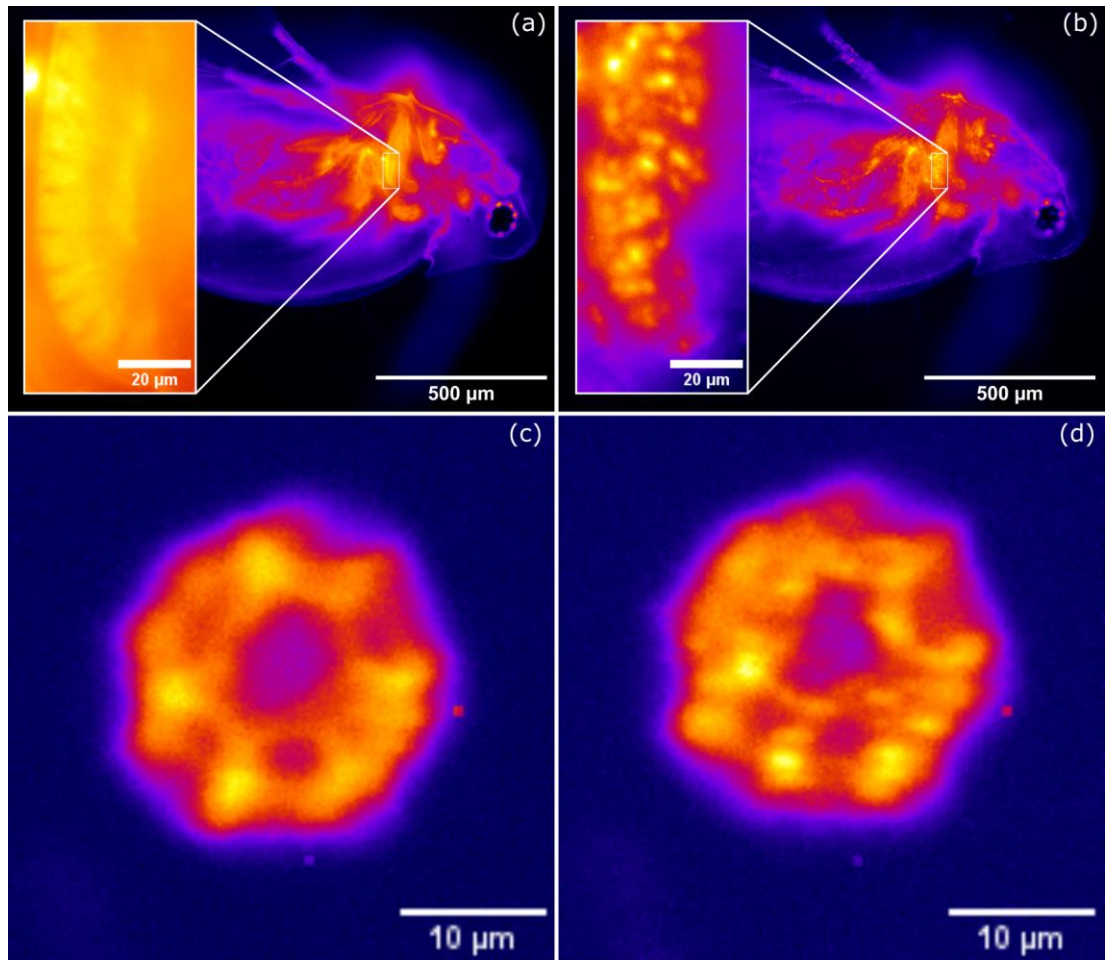


Figure 2.4: Illustration of the speckle illumination contrast degradation compared between pollen grain and *Daphnia*. (a) and (b) show the *Daphnia* specimen with a very fine speckle illumination (a) and a coarse speckle illumination (b). The insets are zoomed in on the indicated area to show the speckle structure more clearly. It can be seen in (a) that the contrast in the speckle illumination is not visible due to the sample thickness whereas the inset in (b) with coarse speckle has contrast at the expense of lack of detail. In comparison, the pollen grain in (d) has contrast with a fine speckle illumination. (c) shows a uniform illumination of the same pollen grain at the same depth as shown in (d).

Figure 2.5 shows a pollen grain specimen sectioned at the sigma value 2 corresponding to  $6.1 \pm 0.2 \mu\text{m}$  section thickness. The low frequency scaling was kept at unity and the x-z views showed the rejection of out-of-focus signal. Comparison to widefield as well as deconvolution of the widefield image performed with Huygens Deconvolution software are shown. Figure 2.5c shows the grey values of the line profile indicated in Figure 2.5b.

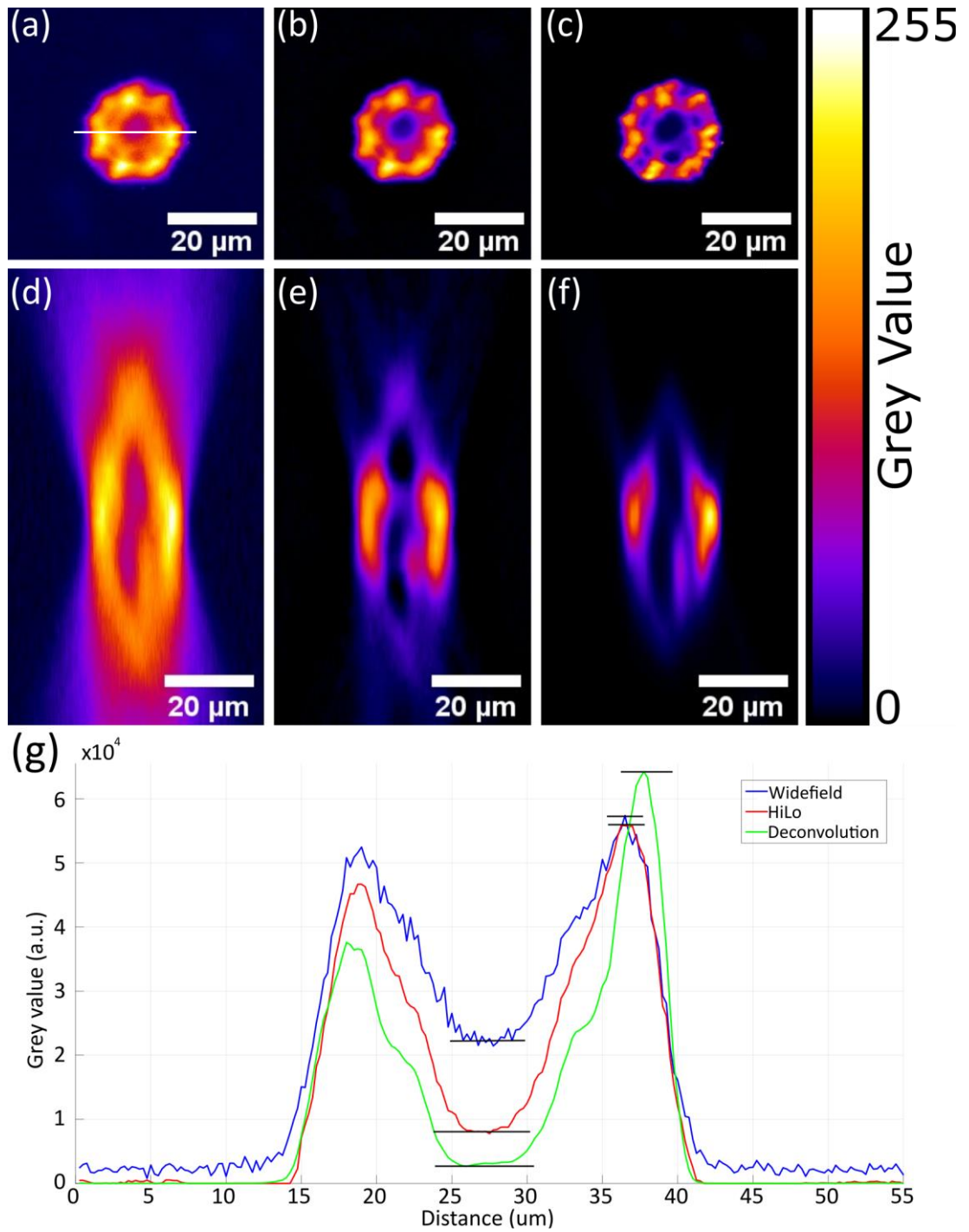


Figure 2.5: *Taraxacum* pollen grain images and quantification of signal-to-background improvement. Shown are x-y views of a single pollen grain in (a) widefield, (b) HiLo, and (c) deconvolution. Out-of-focus background is noticeably reduced after both HiLo processing and deconvolution. Deconvolution was performed on the widefield image. (d-f) shows the widefield, HiLo and deconvolution x-z views, respectively, of the same pollen grain. All images have 'Fire' lookup table applied to better visualise the data. (g) are the plots of the single line indicated in white in (a) in the x-y views through the centre of the Pollen grain. Improvement of signal-to-background was determined by dividing the peak intensity by the intensity in the trough for widefield, HiLo and deconvolution

resulting in 2.6, 6.9 and 22.9 respectively. Improvement in lateral resolution could also be observed in the deconvolved image.

Quantification of the background rejection was performed by dividing the peak intensity by the low intensity in the trough indicated by the black lines in Figure 2.5c. The widefield curve peak-to-trough ratio was 2.6 while HiLo and deconvolution were 6.9 and 22.9 respectively. This measurement was performed for a single pollen grain only. Ideally, for a quantitative, statistically relevant analysis of the sectioning strength, many pollen grains should have been analysed at different positions in the FOV.

Deconvolution achieved more than three times higher peak-to-trough ratio than HiLo. Pollen grains are easy to image in small ROIs allowing for rapid imaging and processing for parameter tuning and evaluation of the results while offering a well-known structure to ensure the absence of artefacts after processing.

### 2.3.3 *Daphnia* imaging with HiLo mesoscopy

As expected from other work in the microscopic domain (J. Mazzaferri *et al.*, 2011), it was found that the speckle pattern for the structured illumination image needed to be coarser when imaging thicker specimens (more than  $\sim 100\ \mu\text{m}$  thick). In the ideal case, the transverse size of an imaged speckle grain was determined by the illumination NA (D. Lim *et al.*, 2008, 2011). However, for thicker specimens the imaged grain size was increased to approximately 20 pixels ( $\sim 5\ \mu\text{m}$  at 9x chip shifting) to maintain high contrast in the difference image for the in-focus regions of the image. This was achieved by changing the variable beam expander such that the beam incident on the diffuser was smaller in diameter, thus creating a coarser speckle pattern in the specimen. The choice of the section thickness parameter had to be made according to the coarseness of said pattern such that several imaged grains would fit in the sampling window for contrast evaluation, so no artefacts of speckle structure

translated through to the final image. As stated in Chapter 2.2.1, the sampling window size, the cut-off frequency and the bandpass filter frequency are all derived from the user input optical section parameter. The smallest window size possible for the contrast evaluation is a 3x3 pixel kernel which would set the bandpass filter at the highest spatial frequency that can be displayed in an image, i.e.,  $\frac{1}{2pixel}$ . However, as mentioned in Chapter 2.3.1, such fine speckle illumination was impractical which led to the scaling of the optical section parameter in the MATLAB script. The fixed relation between the parameters, however, remained intact. The details of the implementation can be found in Appendix 8.1.

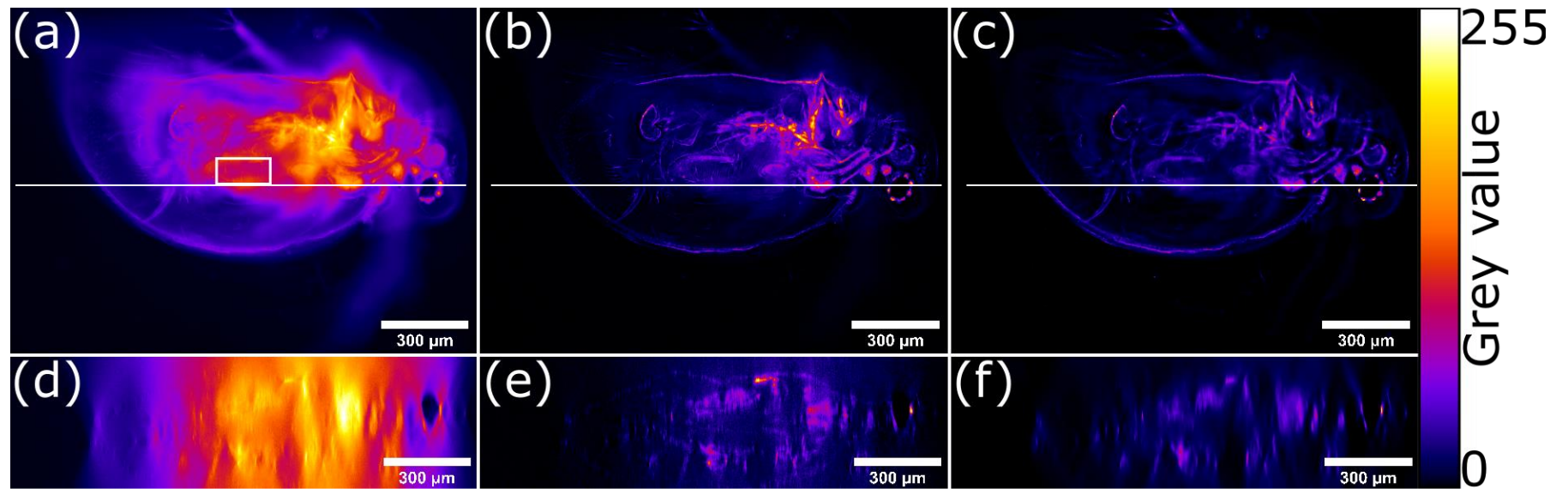


Figure 2.6: Widefield image of *Daphnia* and after processed with HiLo and deconvolution. The top panel shows XY views of widefield (a), HiLo processed (b) and deconvolution (c). The bottom panel are XZ views of widefield (d), HiLo processed (e) and deconvolution (f). The white line in (a), (b) and (c) shows the location of the vertical section in (d), (e) and (f) respectively. This sample was  $\sim 300\ \mu\text{m}$  thick resulting in strong out-of-focus background in the widefield image. The XZ views show significant reduction of out-of-focus background for both HiLo and deconvolution. The images were median filtered to remove hot pixels and brightness adjusted between the minimum and maximum values afterwards to ensure that the whole bit depth was used. To further investigate the fine detail, an ROI, indicated in (a) by the white box, is shown in Figure 2.7.

Eosin-stained *Daphnia* were imaged and processed with the HiLo mesoscopy MATLAB script. The results are shown in Figure 2.6. The *Daphnia* specimen was approximately 300  $\mu\text{m}$  thick making optical sectioning essential for volumetric reconstruction and analysis. The strong background signal made contrast evaluation difficult as naturally with increased background, the signal-to-background ratio, i.e., the contrast, decreased for the speckle illuminated image. However, imaging the specimen with coarser speckle illumination increased contrast at the cost of increased mean distance between neighbouring speckle grains. The section thickness parameter was adjusted accordingly in the script to a value of 4 corresponding to  $8.7 \pm 0.1 \mu\text{m}$  section thickness as per the section thickness measurements performed for Figure 2.3f. Again, for comparison, widefield images and deconvolution images (performed with Huygens) are shown. Deconvolution was more effective at removing the out-of-focus contribution of the PSF. The datasets shown here were consistently deconvolved for 60 iterations which Huygens had set as default. The ROI indicated in Figure 2.6a is shown in Figure 2.7 including a line profile showing that deconvolution preserved the structure of the widefield image while removing background and reducing noise compared to the widefield image. However, the expected sharpening of fine detail typically achieved by deconvolution was lacking. HiLo seemingly increased the brightness in the left half of the image in Figure 2.7a. While the structure itself could be seen in both widefield and deconvolution, it was much dimmer there. The HiLo processed data also appeared to have more noise compared to deconvolution, most likely due to the lack of denoising routines which are employed by the Huygens deconvolution software.



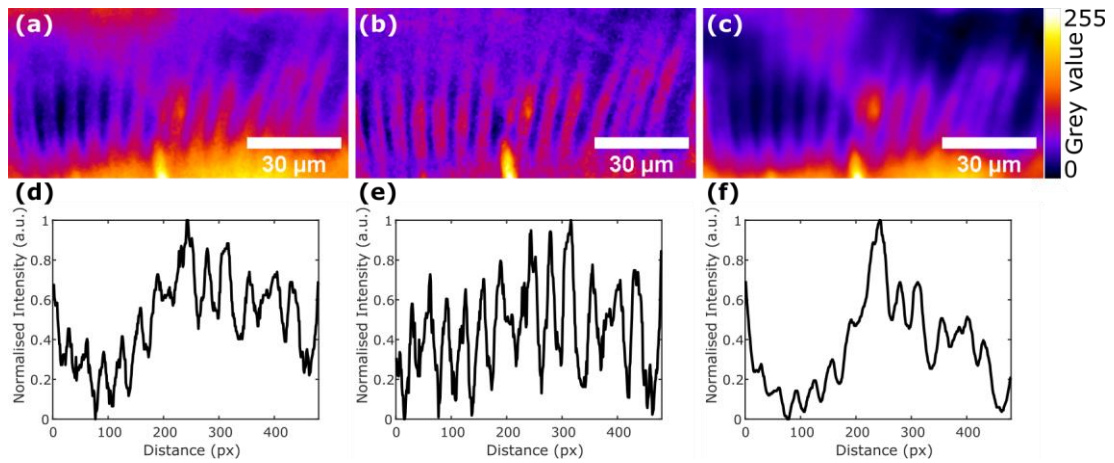


Figure 2.7: Digital zoom of the ROI indicated in Figure 2.6a showing fine detail preservation in thick specimens. (a) shows widefield, (b) HiLo processed and (c) deconvolution images with corresponding line plots (d-f) horizontally through the centre of each image in (a-c). Widefield and deconvolution are almost identical albeit some denoising in the deconvolved image. The HiLo processed data appeared to have more high frequency noise compared to deconvolution but seemed to have recovered some of the fine detail in the left half of the image better than deconvolution.

#### 2.3.4 12-day-old zebrafish imaging with HiLo mesoscopy

The  $\sim 150\ \mu\text{m}$  thick zebrafish stained with Acridine Orange was imaged and HiLo processed in MATLAB with section thickness parameter of 4, same as for the *Daphnia* specimen data. The results are shown in Figure 2.8. This was the lowest value for the combination of sample thickness and choice of speckle coarseness where no artefacts were observed in the final image. The exposure time of the camera detector was 400 ms for each of the nine sensor positions. The FOV was cropped to roughly the size of the zebrafish (3.2 mm x 1.2 mm).

The zoomed-in eye showed improved contrast. Individual cells were clearly visible as well as the broader structure of the surrounding tissue. Figure 2.8 shows a transmission illumination widefield image (the uniform image also used for processing) compared to an optical section from the 61-image z-stack at approximately  $100\ \mu\text{m}$  depth into the sample. An improvement in contrast was evident across the whole field of view and zoomed-in regions of interest revealed fine detail that was not clearly visible in the widefield image.

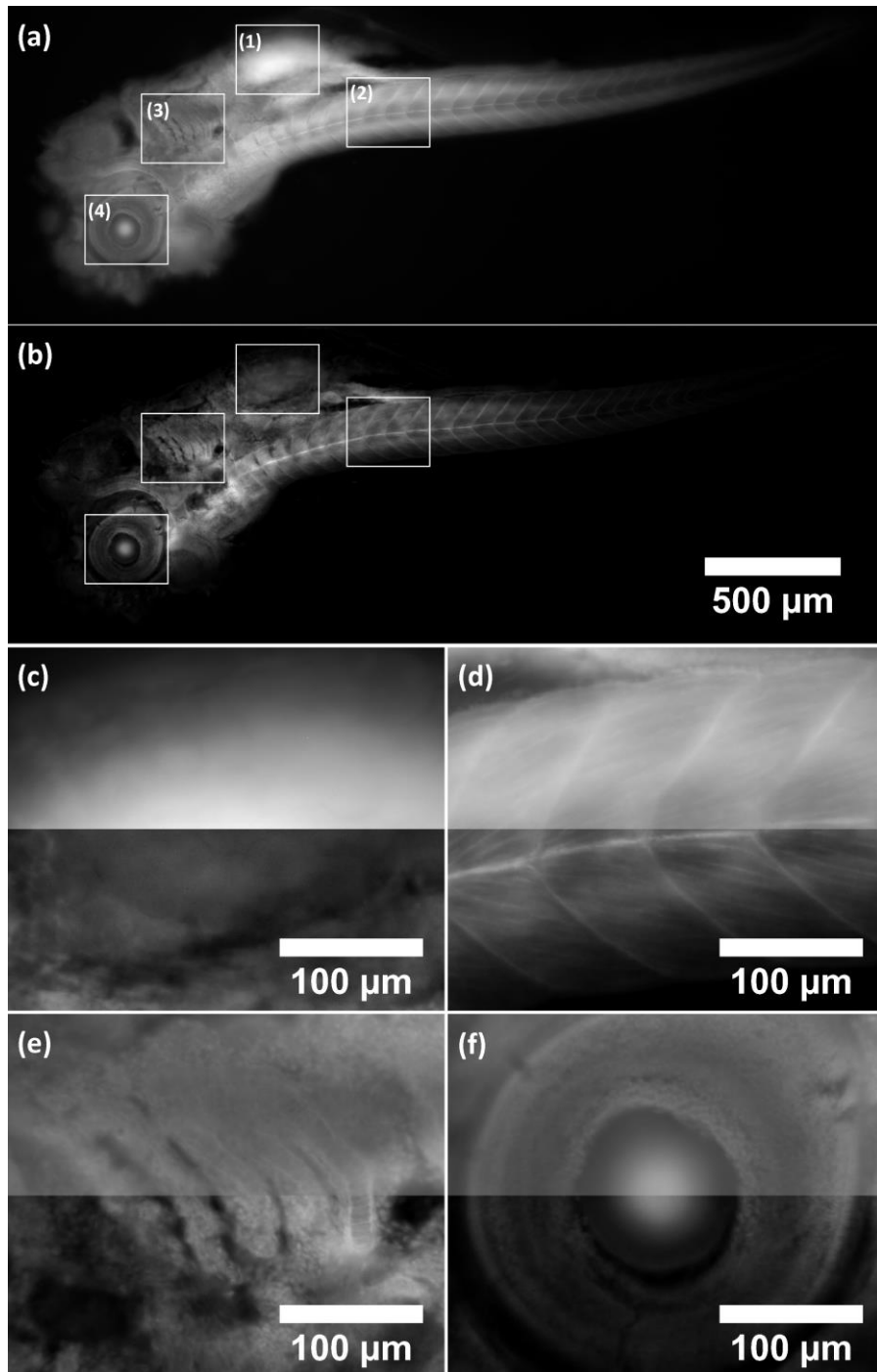


Figure 2.8: Standard widefield image (a) compared to Mesolens HiLo-processed optical section (b) of zebrafish stained with Acridine Orange. Insets (c-f) show zoomed-in regions of interest (1-4) where the widefield and HiLo image were merged (top half is widefield, bottom half is HiLo image). Contrast improvement was evident across the whole image and regions of interest showed fine detail that was barely noticeable in the widefield image. Optical sectioning parameter was set to 4, corresponding to  $8.7 \pm 0.1 \mu\text{m}$  section thickness. With the parameter set lower than that, there were artefacts forming in the final image. There was inhomogeneous brightness with the parameter set to 4 but no artefacts of residual speckle structure could be observed. Setting the parameter higher would have resulted in an unnecessarily thick section.

### 2.3.5 Mouse hippocampal neuronal specimen imaging with HiLo mesoscopy

Lastly, the neuron specimen was imaged and processed with the HiLo script with the section thickness parameter set to 1 again and fine speckle pattern illumination. The images were of the full FOV of the Mesolens and the stack size was 25 slices with 3  $\mu\text{m}$  steps. The script was able to process full FOV Mesolens data without running into memory problems only without using the GPU. As a result, processing time was on the order of an hour for 25 slices. Figure 2.9 shows a widefield and HiLo processed image from the middle of the 75  $\mu\text{m}$  image stack. The widefield stack had strong out-of-focus background above and below the focal plane which can be seen in Figure 2.9c. The HiLo processed data had reduced out-of-focus background across the full FOV and it can also be seen in the XZ view in Figure 2.9d that the specimen had a tilt across the FOV. The fact that the Neuron specimen was thin meant that the XZ views shown in Figure 2.9c and d were very flat due to the ratio of FOV to axial extend. To aid visualisation of the tilt, the XZ views in Figure 2.9c and d have been expanded in the z-direction by a factor of 7.

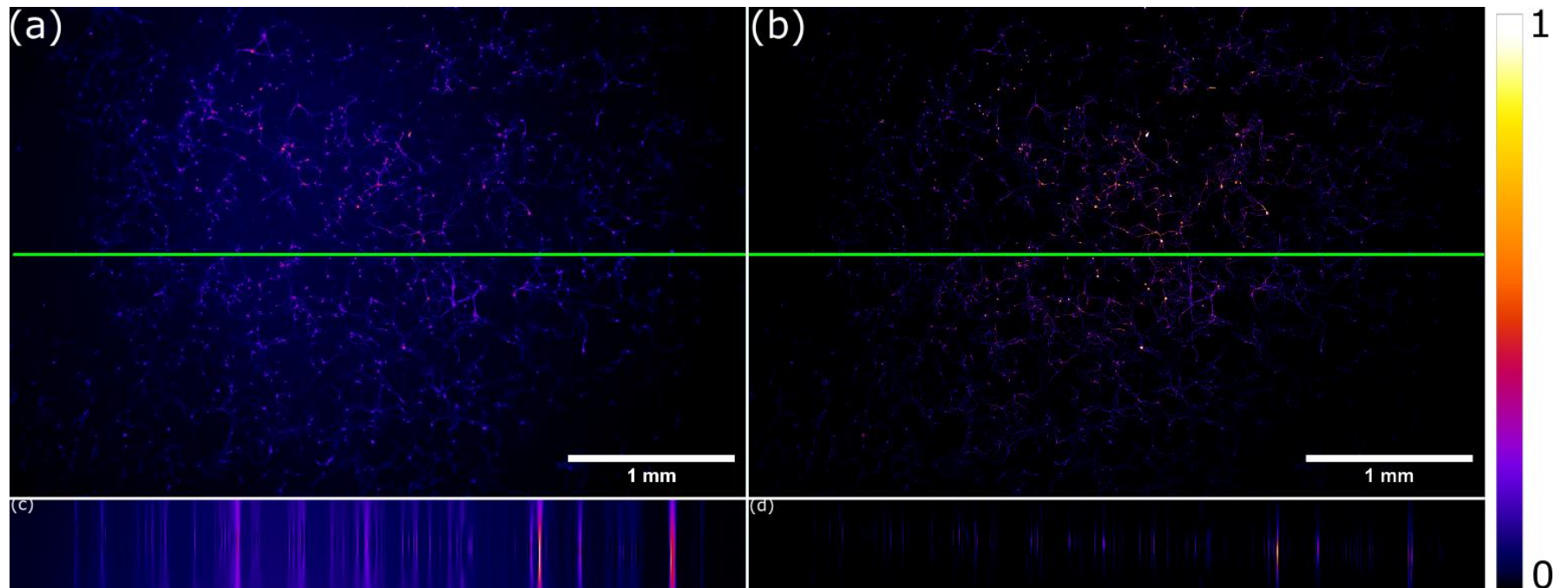


Figure 2.9: Full field of view HiLo processed image compared to widefield image of the mouse hippocampal neuron specimen. The widefield image (a) with its XZ view (c) compared to the HiLo processed image (b) with its XZ view (d). The HiLo processed image has background rejection across the full FOV of the image. It should be noted here that the sample had a slight tilt from the top left corner to the bottom right corner. To better illustrate this tilt, the XZ views in (c) and (d) have been expanded in the z-direction by a factor of 7 using ImageJ. The sample was also very thin, the image stack only covered an axial distance of 75  $\mu\text{m}$ , hence the XZ views are very elongated. This data show that HiLo processing can be applied to full FOV Mesolens data with uniform sectioning across the FOV and without the need to tile the image and potentially generate stitching artefacts during processing.

## 2.4 Discussion

It has been shown here that a fast widefield optical sectioning method for the Mesolens using HiLo microscopy could generate a section thickness of  $5.2 \pm 0.3 \mu\text{m}$ . The measurement was performed in the centre of the FOV only and, although it is reasonable to assume that it would remain constant over the full FOV, additional data could be taken investigating the edge of the FOV as well. The section thickness is on par with CLSM with the Mesolens, which can generate sections of  $5 \mu\text{m}$  thickness, however, HiLo microscopy achieved higher acquisition speed. The camera can acquire a single image in 1.8 seconds whereas a single CLSM image of comparable size takes on the order of 5 minutes. In practise, one must account for the time required to save the data from the camera buffer to the computer, which increased the overall acquisition time for the camera to approximately 10-15 seconds. The lateral resolution remained unaffected by HiLo mesoscopy because the high spatial frequencies, i.e. high resolution content, of the final image is obtained directly by high pass filtering the uniform image and background rejection is only performed on a low frequency complement image. Since the uniform image is a standard widefield camera image, no fine detail is lost (J. Mazzaferri *et al.*, 2011). However, the final image had amplified high frequency noise compared to the standard widefield image. This method presented a speed advantage over CLSM at comparable sectioning strength of  $\sim 5 \mu\text{m}$ , being 30 times faster in raw data acquisition. A MATLAB was written rather than using the existing ImageJ HiLo plugin. Although the plugin performed well when it was initially tested with small datasets, it was slow ( $\sim 16$  times slower than the current MATLAB implementation) when processing large Mesolens data and in some cases the data could not be processed at all due to memory limitations (even when using a server for processing with 1 TB of memory). Using a home-built script further allowed to change parameters like optical sectioning factor, scaling factor

and filter frequencies more freely while knowing what impact each had on the final image. The main speed limitation of widefield acquisition on the Mesolens was not the camera exposure but rather handling of the data itself. At full FOV, camera images are approximately 500 Mb large. Each image needed to be transferred from the camera buffer to the PC's hard drive before a new image could be acquired. As a direct result, reducing camera exposure time by 80% (1000 ms to 200 ms) only reduced acquisition time for a 25-image z-stack from 32 minutes to 27 minutes (~15% time reduction). The chip shifting mechanism of the VNP-29MC was necessary to obtain Nyquist sampled images but shifting the detector chip through nine positions meant that exposure time for one frame was 1800 ms (9 times 200ms) at minimum. The fastest practical exposure setting was 200 ms, as below this exposure time the readout of the CCD detector array increased frame time to 200ms regardless. A single detector array of sufficiently small pixel size would potentially increase acquisition time but would not get around the data handling constraints. Furthermore, no detector with such high pixel number and sensor size compatible with the Mesolens is commercially available at present and custom-built detectors would come at very high cost. One approach for such a custom-built detector could be to build it with larger industry standard pixels of e.g. 6.5  $\mu\text{m}$  and make the entire detector larger. This would in turn make it necessary to reduce the magnification of the Mesolens system and more importantly the detector would have to be curved since at this size correcting the optical elements in the lens to achieve a flat field would be practically impossible.

Despite these drawbacks, HiLo mesoscopy is an excellent alternative to CLSM for the Mesolens and offers some advantage over LSM. Unlike LSM, HiLo obtains uniform section thickness over the full FOV comparable in sectioning strength to CLSM. The setup for HiLo is simpler with just a diffuser in an otherwise ordinary transmission illumination setup. LSM would require side-on illumination, potentially casting lateral shadows across the FOV at

optical section thickness upwards of 30  $\mu\text{m}$  for Gaussian beams. LSM also requires specialised specimen chambers whereas HiLo can operate with the same specimen preparation procedures already in place for the other imaging modalities currently used with the Mesolens.

It has been discussed (J. Mazzaferri *et al.*, 2011) that the out-of-focus background in thick specimens presented a problem for HiLo imaging by reducing in-focus speckle contrast and hence making it more difficult to distinguish in-focus from out-of-focus regions in the image. To maintain high speckle contrast, a coarser speckle illumination pattern was used here. Rather than decreasing the illumination NA, a variable beam expander was used in the illumination beam path. By changing the beam diameter illuminating the diffuser, the speckle coarseness could be adjusted to suite the specimen and maintain sectioning capability, albeit with thicker sections. Although the sections were thicker than the axial resolution, approximately 10  $\mu\text{m}$  for a section parameter of 5, sectioning was still superior to what a Gaussian light sheet is capable of on this FOV. The above-mentioned contrast issue affected section thickness only since lateral resolution was determined by the microscope system.

The results showed that deconvolution was superior in reducing out-of-focus signal and had the additional benefit of improving lateral resolution in the *Taraxacum* specimen. However, the *Daphnia* data showed that deconvolution struggled to maintain resolution improvement in thick specimens. Although background rejection was still superior to HiLo, deconvolution software (in this case Huygens) comes at significant cost on the order of £10,000 whereas writing a HiLo script is comparably simple, or one could use the existing ImageJ plugin for HiLo processing.

## 3 Light Sheet Mesoscopy (LSMe)

### 3.1 Introduction

After the implementation of the HiLo mesoscopy approach with the Mesolens, an illumination system was conceived to generate a light sheet that would have a sufficient Rayleigh range to cover the FOV of the Mesolens of  $4.4 \times 2.9 \text{ mm}^2$ . This presented a challenge because a Gaussian light sheet that could cover that distance would be on the order of  $30 \text{ }\mu\text{m}$  thick, which is an order of magnitude larger than the Nyquist sampling rate ( $3 \text{ }\mu\text{m}$ ) for the Mesolens axial resolution of  $\sim 7 \text{ }\mu\text{m}$ . The current state of LSM has already been described in Chapter 1.5.

To circumvent this problem, it was attempted to generate a two-photon strip that could be scanned through the sample akin to mesoSPIM. This approach would allow near isotropic resolution on the Mesolens, provided the strip could be focused to approximately  $1 \text{ }\mu\text{m}$ , without sacrificing lateral resolution or the need for a rolling shutter because the two-photon excitation would generate fluorescence only within the focal strip due to the nature of the nonlinear absorption process. A solution without a rolling shutter was a necessity because no commercially available camera that can accommodate the combination of resolution and FOV of the Mesolens provides a rolling shutter functionality. A lower pixel number camera could have been used. However, this would have resulted in an undersampled image and ultimately defeated the purpose of using the Mesolens. The disadvantage of this approach compared to a static light sheet is the need to scan the strip across the field of view to form a light sheet over the exposure time of the camera for each of the 9 sensor positions during the pixel shifting. This would involve optomechanical components to perform the scanning,



complicating the setup. This approach failed during its initial attempts which will be explained in more detail in Chapter 3.3.1.

Since the two-photon method did not work well, a Gaussian single photon illuminator was coupled into the Mesolens to investigate the viability of a simple light sheet approach without the need to scan the beam. The advantage of a static light sheet was the simplicity of the setup. While the drawback was the much weaker optical sectioning, it still provided optical sectioning and out-of-focus attenuation compared to epi-fluorescence microscopy.

## 3.2 Methods

### 3.2.1 Two-photon light sheet setup

Figure 3.1 shows the experimental setup for the two-photon light sheet setup. A pulsed infrared (IR) laser (Fianium, 1064 nm, 1 MHz repetition rate, 150 fs pulse length, 1.1 W average output power) was attenuated using a half-wave plate (AHWP10M-980, Thorlabs) and polarising beamsplitter cube (CCM1-PBS253, Thorlabs) and guided through a beam expander, consisting of two plano-convex lenses, an  $f=50$  mm (LA1131-B-ML, Thorlabs) and an  $f=250$  mm (LA1461-B-ML, Thorlabs), to expand and collimate the beam to 12 mm diameter. The expanded beam was used to fill the back aperture of an  $f=22.2$  mm cylindrical lens (LJ1638L1-B, Thorlabs) held by a kinematic mount (KM100C, Thorlabs) to create a focused line. A cuvette filled with fluorescent dye solution of Safranin O (1.05 mg in 3 mL distilled water) was placed in the focus of the cylindrical lens or objective lens and was imaged side on, orthogonal to the laser beam propagation direction to estimate the fluorescence excitation and the sheet thickness or spot size. The detection optics were a 10x 0.45 NA objective lens, an  $f=35$  mm plano-convex lens (LA1027-A-ML, Thorlabs) and a monochromatic CMOS camera (UI-3060-CP-M, IDS Imaging Development Systems GmbH).

An alternative setup was built to generate a focused spot by replacing the  $f=22.2$  mm cylindrical lens with a  $4\times 0.1$  NA objective lens (CFI Plan Achro 4x, MRL00042, Nikon). Additionally, the short focal length lens L1 in Figure 3.1 used to build the beam expander was exchanged for an  $f=25.3$  mm plano-convex lens (LA1951-B-ML, Thorlabs). The  $f=250$  mm lens L2 in Figure 3.1 as above (LA1461-B-ML, Thorlabs) remained in the setup, but its position was adjusted to accommodate the shorter focal length of the  $f=25.3$  lens. The setup was otherwise identical to the one for the line focus.

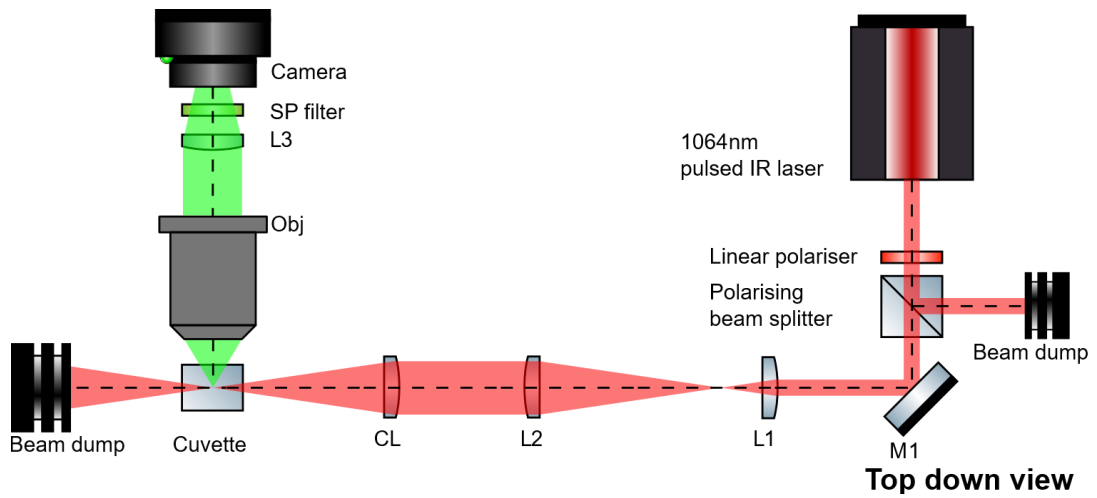


Figure 3.1: Experimental setup for two-photon light sheet generation. The pulsed IR laser was attenuated using a linear polariser in combination with a polarising beam splitter and a beam dump. The attenuated beam was reflected by mirror M1 into the beam expander comprised of lenses L1,  $f=50$  mm, and L2,  $f=250$  mm. The collimated, expanded beam filled the back aperture of the cylindrical lens CL,  $f=22.2$  mm, and was then focused inside the cuvette filled with Safranin O solution. Fluorescent signal was collected with a  $10\times 0.45$  NA objective lens, Obj, and imaged through SP filter, a 550 nm short pass filter, onto the detector by L3,  $f=35$  mm, of a CMOS camera.

### 3.2.2 Single-photon Gaussian light sheet setup

The Gaussian light sheet was generated using a 488 nm continuous wave (CW) laser (Sapphire LP/LPX 488, Coherent). The beam had an initial diameter (FWHM) of 1 mm and was expanded using a beam expander comprised of a pair of 25.3 mm (LA1951-A-ML, Thorlabs) and a 250 mm (LA1461-A-ML, Thorlabs) focal length plano-convex lenses, resulting in a collimated

beam with 12 mm beam diameter. The expanded beam was guided by several mirrors (BB1-E02, Thorlabs) and onto a vertically positioned breadboard towards the specimen stage of the Mesolens such that the illumination was orthogonal to the detection beam path of the Mesolens and remained stationary while the sample stage moved through x, y and z. A  $f=300$  mm cylindrical lens (LJ1558RM-A, Thorlabs) was used to form the light sheet in the focal plane of the Mesolens resulting in a sheet 12 mm wide (measured perpendicular to both the illumination beam and Mesolens detection direction) with  $\sim 30$   $\mu\text{m}$  FWHM thickness at the focus, diverging to  $\sim 40$   $\mu\text{m}$  FWHM at the edges of the FOV, 1.5 mm to either side of the focus, which agreed well with the theoretical value from equation (19). The sheet thickness was measured using a Thorlabs beam profiler (BP209-VIS, Thorlabs) positioned on the Mesolens specimen stage in the absence of a sample. Furthermore, a fluorescent bead sample (yellow-green fluorescent beads, 500 nm diameter) was used to ascertain the signal attenuation along the z-axis. This method allowed to identify the axial location where the detected signal dropped to zero.

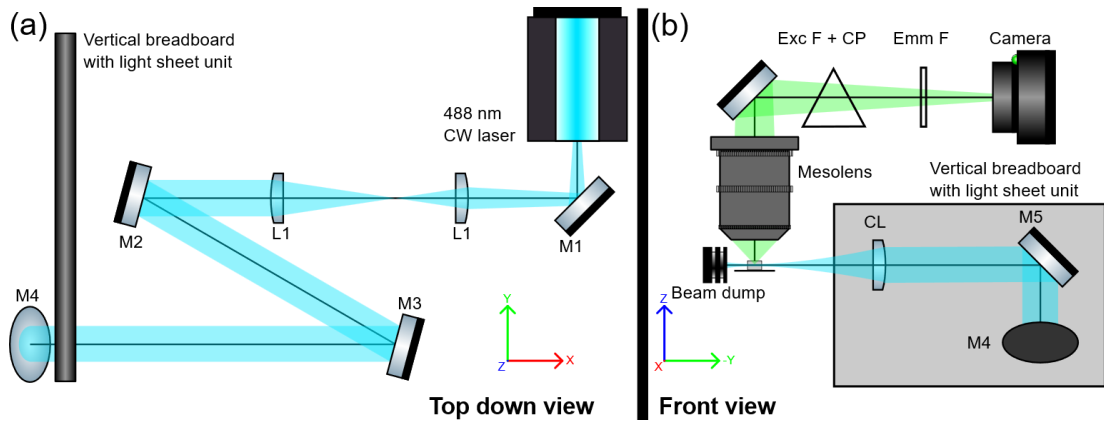


Figure 3.2: Experimental setup for Gaussian light sheet mesoscopy on the Mesolens. (a) shows a top-down view of the setup. The output of the Coherent Sapphire 488 nm laser (cyan coloured beam) was guided with mirror M1 into a beam expander, L1,  $f=25.4$  mm and L2,  $f=250$  mm. The collimated beam was reflected by mirrors M2 and M3 onto mirror M4 which reflected the beam upward aligned with the vertically mounted breadboard containing the light sheet unit. (b) is the front view (see cartesian coordinate system for reference) of the setup. The mirror M5 guided the expanded beam into the back aperture of the cylindrical lens CL,  $f=300$  mm. The light sheet was formed in the focal plane of the Mesolens which collected fluorescence signal (green coloured beam) and formed

the image on the detector chip of the camera (VNP-29MC -M/C, Vieworks). The excitation filter and compensator plate, Exc F +CP, as well as the emission barrier filter, Emm F, were in the Mesolens frame.

Figure 3.2 shows schematically how the Gaussian light sheet was coupled into the Mesolens. A dedicated illumination path was built for the side-on illumination with a large breadboard vertically mounted for the light sheet unit. This was necessary due to the height of the Mesolens focal plane with respect to the optical table of approximately 200 mm. In the top-down view in Figure 3.2a mirror M5 would be on top of mirror M4 and the cylindrical lens CL would also be visible further along the beam path. For the sake of simplicity of the diagram, however, all optical elements from the front view are omitted in the top-down view, except for mirror M4.

Although the light sheet data did not require any post-acquisition processing, to open the large z-stacks the same server was used as before (see Chapter 2.2.3). This was necessary since the largest z-stack acquired with the light sheet setup was on the order of 400 GB, which greatly exceeded the memory that is available on a standard desktop workstation.

### 3.2.3 Fluorescent bead sample

The fluorescent bead sample was prepared by diluting green-fluorescent 500 nm beads (yellow-green (505/515), F8813, Thermo Fisher Scientific, UK) in a two-component resin mix (Biothan 2 MD 1785 N with Biodur M 330, Silitech AG) in a ratio of 1:2.5 resin to hardener and left to harden in a glass cuvette while de-aerating under vacuum to avoid the formation of enclosed air bubbles. Two different dilution ratios were made up, one with dilution 1:1,000 for a densely populated bead sample and 1:10,000 for a sparse bead sample. The cuvette was put on its side and in contact with a coverslip using immersion oil as a medium, thus refractive index matching the coverslip, cuvette, and resin for imaging with the Mesolens with oil immersion using the light sheet illumination setup detailed in Chapter 3.2.2. exciting

the bead sample at 488 nm and detecting at 520 nm. The 75 x 75 x 0.17 mm<sup>3</sup> coverslip was a necessary addition in the imaging process due to the size of the Mesolens front element. If the cuvette would have been attempted to be imaged without the coverslip, the immersion oil would have quickly flowed down the sides of the cuvette and the front element would have lost the immersion. Figure 3.3 illustrates the imaging setup with a side view. The image is acquired through the side wall of the cuvette as it lay on its side on the specimen stage

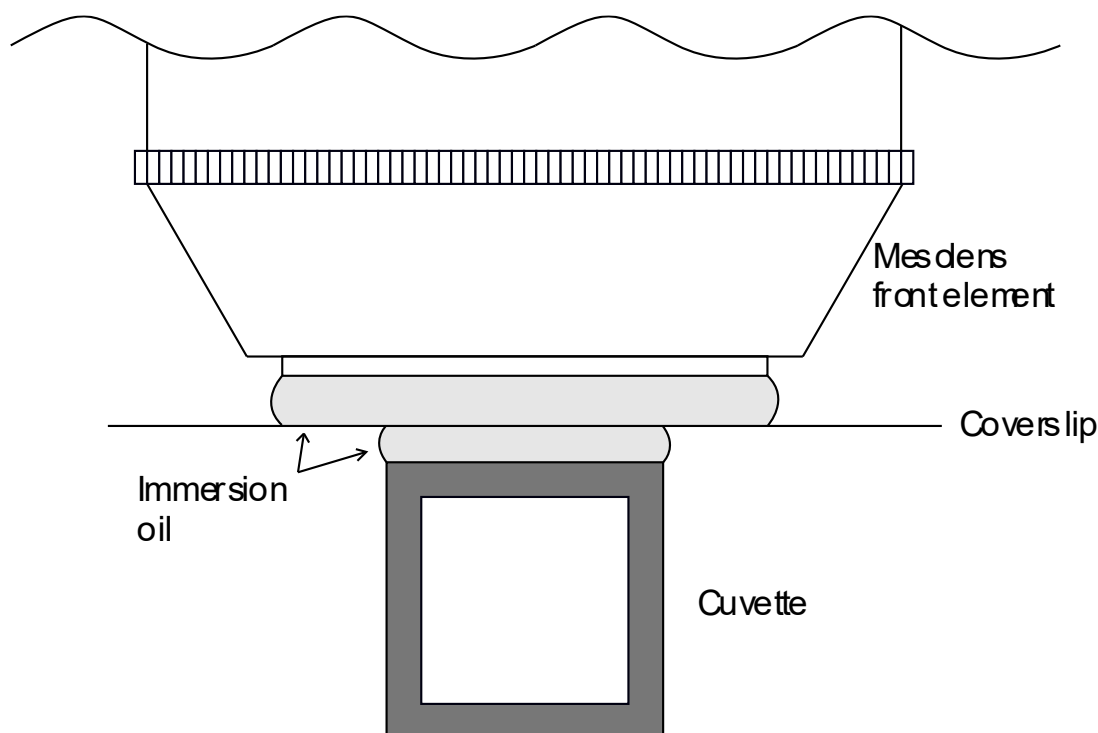


Figure 3.3: Illustration of the cuvette imaging setup on the Mesolens. The cuvette lay on its side and was imaged through its side wall that is pointing up. Immersion oil was used to make a refractive index matched contact between the coverslip and the cuvette and the coverslip and the Mesolens front element. The coverslip was necessary because the front element is larger than the cuvette and this would have otherwise led to the immersion oil flowing down the sides of the cuvette and thus the immersion would have been lost.

### 3.2.4 Fluorescent dye solution

A 1 mM stock solution of Safranin O (Sigma-Aldrich Company Ltd., Gillingham, UK) was made by dissolving 1.05 mg Safranin O dye in 3 mL distilled water and stored in a plastic cuvette sealed with Parafilm tape (Sigma-Aldrich Company Ltd., Gillingham, UK) to prevent

evaporation. The stock solution was further diluted to 100  $\mu$ M in a glass cuvette for imaging and sealed with Parafilm tape. The cuvette was 5 cm tall to ensure that the Parafilm sealing would not block or scatter the excitation or detection beam during imaging. The imaging volume was restricted to the bottom 1 cm of the cuvette while the parafilm sealing did not extend further than the top 2 cm of the cuvette.

The cuvette was then placed in the focal point of the objective lens or cylindrical lens in the two-photon setup described in Chapter 3.2.1.

### 3.2.5 Mouse pancreas specimen

The mouse pancreas sample was harvested from a wildtype mouse, C57 BL/6, by my colleague Katrina Wesenraft. The harvested pancreas was fixed with 4% paraformaldehyde (PFA), washed for 30 minutes 3 times with PBS, then dehydrated with Methanol (MeOH), and rehydrated in MeOH. The specimen was then treated with RNase with a concentration of 100  $\mu$ g/mL for 3 hours. It was then stained with 100  $\mu$ M Propidium Iodide (PI) overnight. Another wash cycle (3 times, 30 minutes) was done before the pancreas specimen was embedded in 1% low melting point agarose for ease of handling. The tissue was dehydrated through a MeOH series, and the specimen was cleared in benzyl alcohol benzyl benzoate (BABB) of ratio 1:2 benzyl alcohol:benzyl benzoate for 5 days.

For imaging with light sheet illumination, the pancreas sample was placed in a 3mm high square frame cut from a high-quality quartz cuvette (cut cuvette pieces were kindly provided by Prof W.B. Amos) to ensure the side on illumination passes through optically flat surfaces into the specimen. The frame was placed on a large glass slide and sealed around the outside edges with clear nail varnish before the agarose embedded pancreas sample was put inside. The volume was filled with BABB and a large #1.5 borosilicate glass cover slip (75 mm x 75 mm) was carefully put on top, avoiding bubbles, and sealed with clear nail varnish at three

of the edges, leaving one side clear for the excitation beam path. The prepared sample was imaged with the Mesolens with Type DF oil immersion.

### 3.3 Results

#### 3.3.1 Two-photon Gaussian light sheet

A spot focus was imaged orthogonally to the beam propagation direction to measure the spot size. In addition, a beam profiler (Scanning-Slit Optical Beam Profiler, BP209-VIS, Thorlabs) was used to measure the spot size directly. It was found that the minimum fluorescence emission profile (FWHM) that could be measured was  $10.46 \pm 0.23 \mu\text{m}$ . The full width at  $1/e^2$  intensity was calculated as  $17.76 \pm 0.39 \mu\text{m}$ . The results are shown in Figure 3.4.

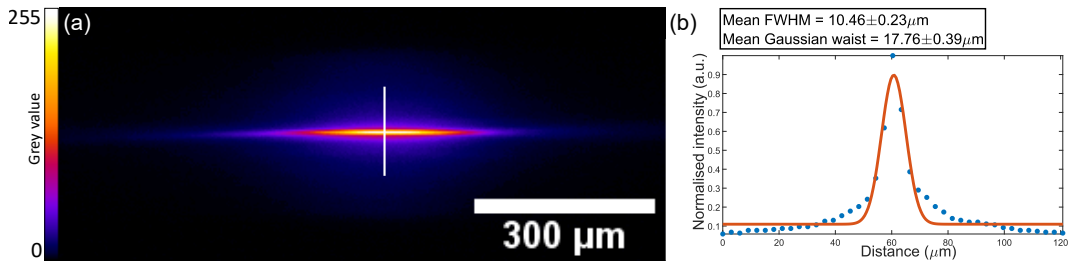


Figure 3.4: (a) Two-photon excitation image of the Safranin O filled cuvette in the spot focus setup. (b) Intensity profile indicated by the white vertical line in (a) including mean measurement of full-width at half-maximum (FWHM) and Gaussian waist, or 13.5% intensity width. Measurement was averaged over nine adjacent, parallel lines between two maximum intensity points in (a).

The strip focus using the  $f=22.2 \text{ mm}$  cylindrical lens resulted in very dim fluorescence and could only be imaged with a large noise floor due to the high camera gain required. Fitting Gaussian plots was only possible after filtering the image with a  $3 \times 3$  pixel kernel median blur and the measured FWHM and Gaussian waist diameter were  $23.34 \pm 2.21 \mu\text{m}$  and  $39.64 \pm 3.75 \mu\text{m}$ , respectively. The image and example line plot are shown Figure 3.5.

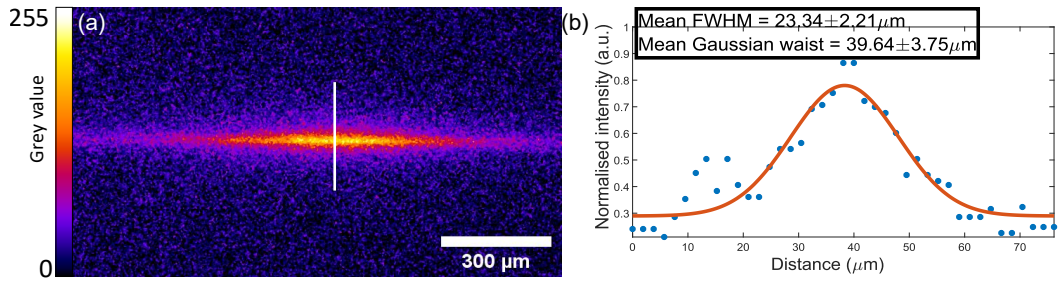


Figure 3.5: Two-photon strip focus imaged orthogonally to the propagation direction of the illumination beam. The image (a) is dominated by camera noise due to the low fluorescence response. (b) shows the intensity plot indicated by the vertical line in (a).

### 3.3.2 Single photon Gaussian light sheet

To evaluate the detection PSF axial profile of a single photon Gaussian light sheet the beads in resin inside the cuvette were imaged. The light sheet had a thickness (FWHM) of  $\sim 30 \mu\text{m}$  in the center of the FOV of the Mesolens and diverged to  $\sim 40 \mu\text{m}$  (FWHM) at the edge of the FOV at  $\sim 1.5 \text{ mm}$  from the center as expected from equation (11). The light sheet remained within  $3 \mu\text{m}$  of the Mesolens focal plane over a z-range greater than  $1.8 \text{ mm}$  (movement of the Mesolens specimen stage). It was found that in practice z-travel of the specimen stage of more than  $2.4 \text{ mm}$  resulted in the front element of the lens sticking to the coverslip, most likely due to surface tension. The side view of the imaging setup in Figure 3.3 shows that the coverslip had only loose contact with the cuvette which did not pose a problem unless the specimen stage moved the sample up to the point where the coverslip stuck to the front element of the Mesolens. This led to the limited z-travel of  $2.4 \text{ mm}$  mentioned above. The mouse pancreas sample showed that the sheet was scattered out of the focal plane of the lens after a z-travel range of approximately  $2 \text{ mm}$ . Parts of the sheet remained in focus and it could not be determined if this was due to the cuvette surface or additive misalignment in the system.



The light sheet was measured with a beam profiler at the specimen position relative to the cylindrical lens. The measured FWHM was  $\sim 30\ \mu\text{m}$  at the beam focus and  $\sim 40\ \mu\text{m}$  at a distance of 1.5 mm from the beam focus corresponding to the edge of the field of view.

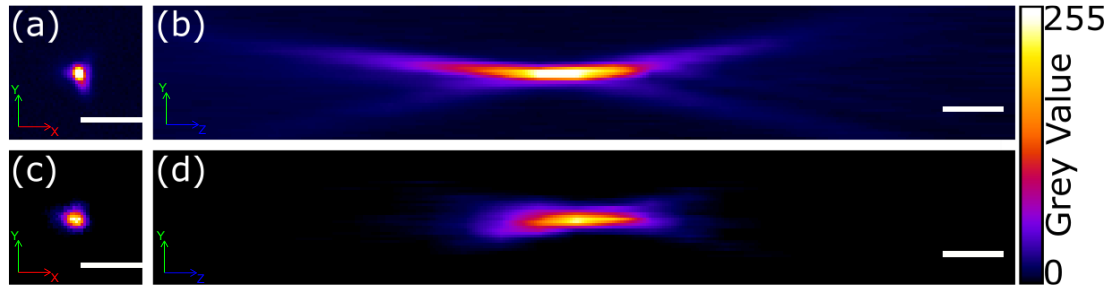


Figure 3.6: Images of 500 nm green-fluorescent beads. Epi-fluorescence XY (a) and YZ (b) views compared to LSM XY (c) and YZ (d) views, where z is the optical axis of the Mesolens. These images were cropped from the Mesolens full FOV to show only one sub-resolution bead. The ‘Fire’ lookup table (LUT) was chosen to better visualise the out-of-focus region of the PSF. Epi-fluorescence images were acquired with LED illumination at 490 nm (CoolLED pe4000) and LSM excitation was a Coherent 488 nm laser and oil immersion was used in both cases. There is residual aberration in panel (b) which could negatively impact the bead measurement, however, the axial extend of the epi-fluorescent bead (b) is clearly larger than that of the LSM bead (d) while lateral extend of epi and LSM (a and c respectively) was comparable. Scale bar in all four panels is  $5\ \mu\text{m}$ .

An attempt was made to estimate the section thickness inside the bead sample by measuring the axial extend of a single bead. Comparing a YZ view of a bead sample imaged in epifluorescence to the same sample imaged in LSM, it could be seen that the PSF extended much further in the z-direction in the epi-fluorescence image. The z direction here is the optical axis of the Mesolens and the images are cropped from the full FOV to show a single sub-resolution limit bead. The recorded signal from the light sheet illuminated bead sample was only larger than 0 within a z-range of  $\sim 30\ \mu\text{m}$  which agreed well with the beam profiler measurement. Figure 3.6 shows the comparison of a single bead between epi illumination and light sheet illumination. However, measuring the PSF in this manner would only provide a measure of the axial resolution. To estimate the optical section thickness, several beads should have been imaged from different positions in the FOV and then laterally integrating each slice a measure of the optical section thickness could have been obtained. The beam

profiler already provided an accurate measure of the light sheet thickness, but the above-mentioned approach should be implemented in the future. There was asymmetry in the epi-illumination PSF in Figure 3.6b which was most likely caused by residual coma aberration in the system. This contributed to larger lateral PSF for the epi-illumination measure when compared to the light sheet illumination. However, the PSF comparison was aimed at the axial extend to obtain a measure of the light sheet thickness rather than comparison of lateral resolution which was unaffected by the choice of illumination.

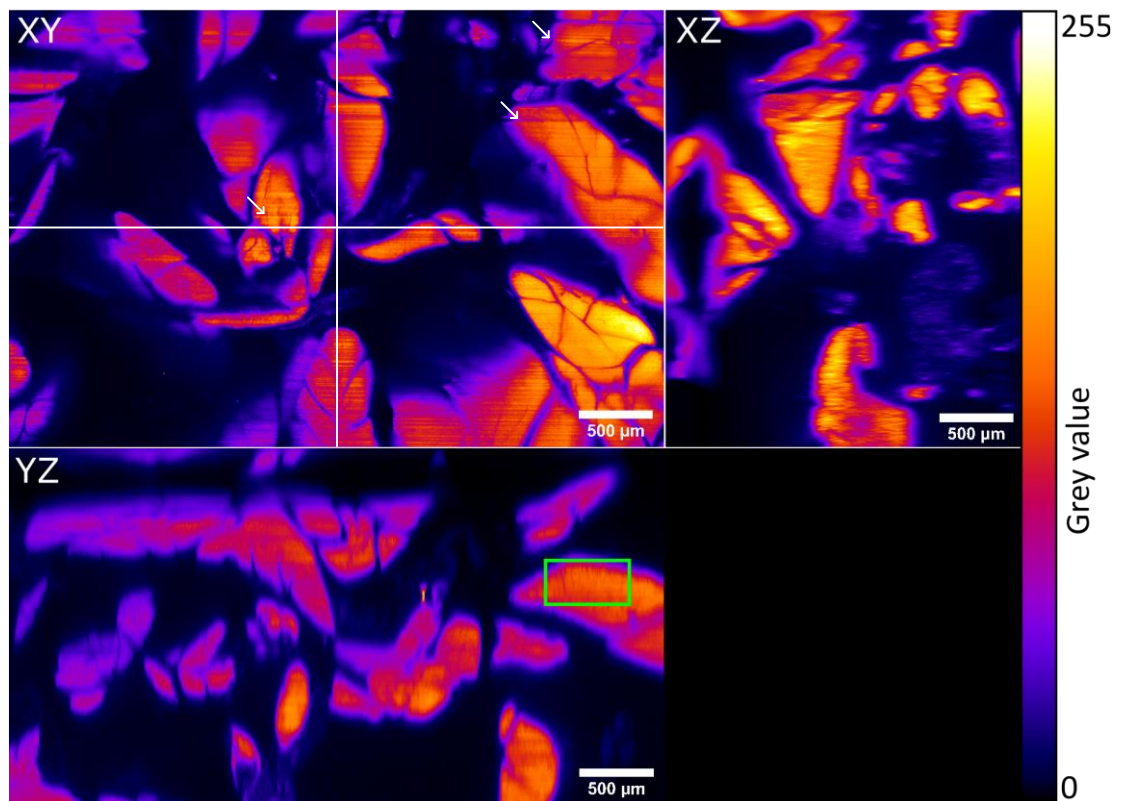


Figure 3.7: XY, YZ and XZ views of a *propidium iodide* (PI) stained mouse pancreas obtained with the LSM illuminator. The dataset is  $4.4 \times 2.9 \times 2.4 \text{ mm}^3$  in size at  $0.224 \times 0.224 \times 3 \text{ } \mu\text{m}^3$  voxel size. Orthogonal view slices are in the centre of the stack from either side, at the position of the vertical and horizontal white line respectively. The *Fire* lookup table (LUT) was chosen to enhance contrast and emphasise background rejection. The light sheet illumination propagated from right to left in XY and YZ, striping artefacts and fluorescence response intensity drop-off are noticeable across the images whereas no drop-off is visible in XZ. White arrows show example of striping artefacts, however, they occur across the entire FOV.

Figure 3.7 shows an image of the mouse pancreas prepared as described in Chapter 3.2.5 with the single photon Gaussian light sheet and detected using the Mesolens and Vieworks camera. The dataset was acquired over the 2.4 mm distance described at the beginning of this chapter in 3  $\mu\text{m}$  steps resulting in a stack of 800 images. The entire dataset was 386.6 GB in size and represents the maximum practical size of a 3-dimensional dataset on the Mesolens MkII camera system (except for time series, which, in theory, has no upper limit in terms of size). In comparison, the prototype CLSM Mesolens system, which imaged a 6 mm x 6 mm x 3 mm volume generated datasets of approximately 639 GB (G. McConnell *et al.*, 2016). Individual pancreas lobes could be clearly identified and void regions between lobes show no out-of-focus signal. Signal attenuation across the FOV (sheet propagation direction in the XY and XZ images is right to left) as well as striping artefacts, shown with white arrows in Figure 3.7, are clearly visible.

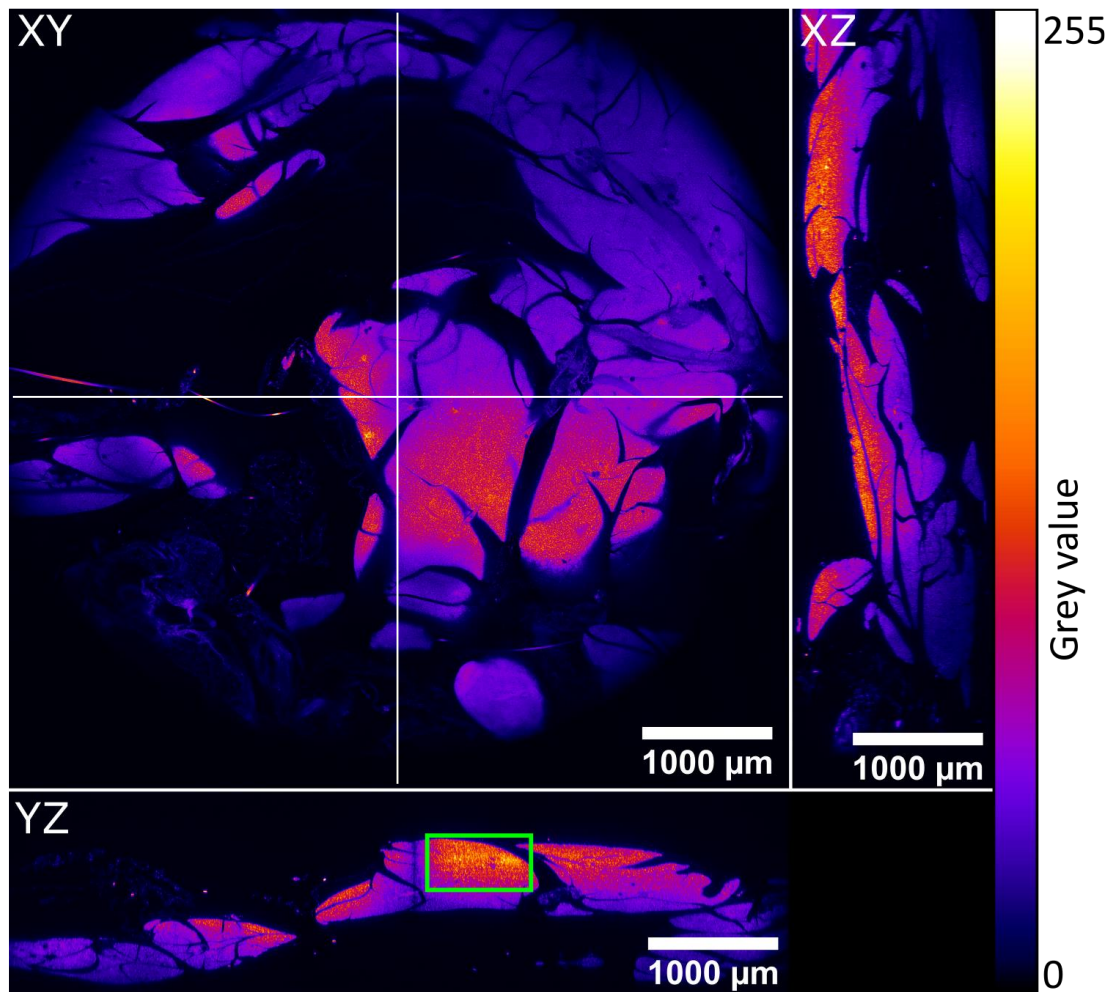


Figure 3.8: Confocal mesoscopy dataset of the same mouse pancreas specimen as Figure 3.7. XZ and YZ views show the excellent sectioning strength of confocal microscopy. White horizontal and vertical line show the position of the YZ and XZ views respectively.

Figure 3.8 shows the same pancreas specimen imaged with the Mesolens in CLSM mode by my colleague Katrina Wesencraft. Sampling for this dataset was 2 pixel/ $\mu\text{m}$  in the lateral dimension and 4  $\mu\text{m}$  steps in the axial dimension and three-frame averaging per image. The superior sectioning capability can be clearly seen around the edges of the lobes, in the YZ and XZ views, the CLSM data is sharply in focus whereas in the LSM data the edges are blurred. This indicates contribution to the image from out-of-focus light. Furthermore, there are no obvious artefacts in the CLSM data. The signal attenuation with increasing depth, however, is evident here, showing the limitation of CLSM for imaging thick specimens.

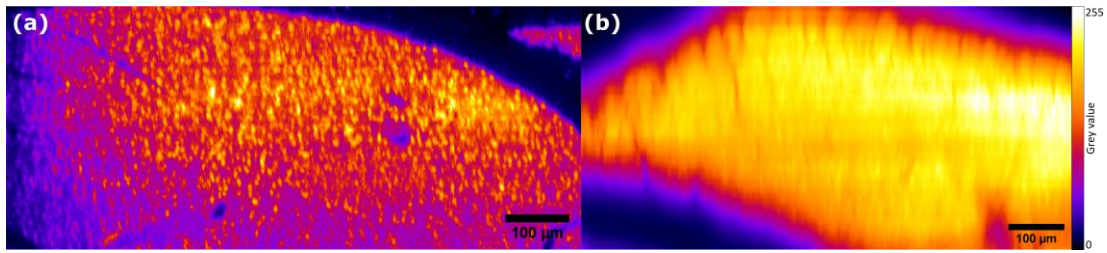


Figure 3.9: Cropped insets of the YZ views indicated by the green boxes in Figure 3.7 and Figure 3.8 respectively. The regions are comparable in size and axial position in the specimen, however, since these are two different datasets, the regions are not an exact match. (a) is from the CLSM dataset. Individual nuclei stained with PI are clearly visible showing the thin optical sectioning capability of CLSM. (b) is the light sheet data. Individual nuclei cannot be resolved. This is due to the light sheet being an order of magnitude thicker than the Mesolens axial resolution.

Figure 3.9 shows the ROIs from the YZ-views in Figure 3.8 and Figure 3.7 (green boxes) as (a) and (b) respectively. The CLSM data showed that individual nuclei stained with PI could be resolved both laterally and axially whereas this was not the case in the light sheet dataset. The light sheet thickness of 30  $\mu\text{m}$  evidently generated too much out-of-focus background to resolve nuclei.

The LSM z-stack comprised of 800 images used in Figure 3.7 took on the order of 4.5 hours to acquire. The data was acquired at 200 ms exposure time per frame at 9 times pixel shift leading to 1800 ms per slice, which is the minimum exposure in terms of imaging speed because the sensor readout is the limiting factor in this case (see Chapter 1.8 for more detail on the camera limitation). In comparison, the CLSM z-stack comprised of 390 images used in Figure 3.8 took on the order of 130 hours. The different number of slices has two reasons; Firstly, the CLSM stack had 4  $\mu\text{m}$  z-steps instead of 3  $\mu\text{m}$  for the light sheet stack. Secondly, the z-range of the CLSM stack was only 1560  $\mu\text{m}$  compared to the 2400  $\mu\text{m}$  of the light sheet stack. Normalising to the same number of z-slices, the speed advantage of light sheet over CLSM on the Mesolens can thus be estimated to approximately 60 times depending on imaging conditions.

### 3.4 Discussion

It was clear beforehand that a Gaussian light sheet with a Rayleigh range that covered the Mesolens FOV would be considerable thicker than the depth of field (DOF) of the Mesolens, on the order of 30  $\mu\text{m}$  compared to the Mesolens DOF of 7  $\mu\text{m}$ . However, in optically clear but densely labelled specimens like the mouse pancreas shown in Figure 3.7 it has been shown to have significant attenuation of background fluorescence. Although the light sheet generated here was an order of magnitude thicker than would be desired, it was still a viable addition to the Mesolens system and offered some advantages over epifluorescence widefield imaging. While optical sectioning was weak, it was still superior to no optical sectioning and the light sheet approach was limited in imaging speed only by the camera, same as epifluorescence. However, the side-on illumination did result in striping artefacts common to single sided light sheet illuminators.

The two-photon light strip approach was unsuccessful in its current implementation. The fluorescent response from the strip illumination was dim to the point where it was practically indistinguishable from background noise in the camera image. Even the spot focus from the pulsed IR laser only resulted in a weak fluorescent signal. The data indicated that the focus of the beam was much larger than should theoretically be possible. The measured fluorescence response indicated a beam diameter on the order of more than 10  $\mu\text{m}$  using the 4x 0.1 NA objective lens, where it could be expected from equation (10) to have a spot size an order of magnitude smaller. This would also explain the weak signal resulting from the non-linear absorption process the fluorescent dye molecules undergo during two-photon excitation.

Ultimately, it could not be determined why the two-photon approach had such underwhelming results. The laser itself had the expected output of 1.1 Watt average power

at 1 MHz repetition rate which would be sufficient peak intensity to achieve high fluorescence response in Safranin Orange dye even in a larger excitation volume such as a strip of a few  $\mu\text{m}$  thickness and 4 mm wide.

Nevertheless, the approach has still merit. Firstly, it could bring the Mesolens close to isotropic, sub-micron resolution with a swept focused infrared line for two-photon excitation of fluorescence. Secondly, unlike in the mesoSPIM approach, the two-photon approach would not require a rolling shutter that moved synchronously with the strip because the fluorescence response would be limited to the focal volume of the swept strip due to the non-linear absorption process of two-photon excitation. Thus, the diverging beam that generates fluorescence in the mesoSPIM method that must be blocked by the moving shutter would be negligible when using two-photon excitation. Therefore, the two-photon approach could be implemented with the Vieworks camera on the Mesolens. This limitation was important when considering methods for the Mesolens because very few cameras are commercially available that can accommodate the combination of large FOV and sub-micron lateral resolution. At the time of writing this thesis there were three cameras available from Vieworks in addition to the VNP-29 series used in this work that may be suitable for LSM. One is the VNP-200MX-M/C 30 (VN-200MX-M/C 30 was also available which uses the same chip as the VNP-200MX-M/C 30 and had the same specifications) with a pixel size of  $4.5\ \mu\text{m}$ , sensor size of  $7920 \times 6004$  pixels, and 3.4 fps at 9x pixel shift. The second is the VN-25MX-M/C 72 with  $4.5\ \mu\text{m}$  pixel size,  $5120 \times 5120$  pixel sensor size, and 8 fps at 9x pixel shift. Lastly, the VNP 604MX-M/C 6 H has a  $3.76\ \mu\text{m}$  pixel size,  $14192 \times 10640$  pixel sensor size and 1.5 fps at 4x pixel shift. All these cameras could accommodate the Mesolens optical parameters at varying maximum FOV (sensor size) and acquisition time.

The specimen preparation using the two-component resin outlined in Chapter 3.2.3 was attempted for small volumes which proved to be problematic. Small volumes of the resin-

hardener mix, when placed in the cut cuvette pieces used for specimen preparation in Chapter 3.2.5, could not be de-aerated successfully. The air trapped in the small volume would result in the mixture overflowing the small cuvette piece during this step resulting in hardened resin blobs on the outside of the cuvette walls, thus making reliable orthogonal illumination impossible. After hardening the small volumes would also still contain trapped air bubbles rendering the specimen useless for imaging. According to the manufacturer datasheet the hardening process can be accelerated by heating the mixture up to 120°C which can reduce the effect of trapped air bubbles, however, generating small volume resin pieces would still pose a problem due to the need to de-aerate the small volume.

The single-photon Gaussian light sheet performed as expected from theory. To achieve a Rayleigh range that covered the FOV of the Mesolens the light sheet thickness had to be on the order of 30  $\mu\text{m}$ . From the beam profiler measurement, the optical section was estimated on the order of 30  $\mu\text{m}$  at the center of the FOV and 40  $\mu\text{m}$  at the edge of the FOV which is a distance of 1.5 mm from the center. The axial resolution remained unaffected because the sheet FWHM is four times larger than the DOF of the Mesolens. Although a simple Gaussian light sheet on the Mesolens does not produce improved axial resolution, this approach significantly reduced out-of-focus background in thick specimens making widefield imaging on the Mesolens viable for large, cleared samples with a speed advantage over CLSM, taking a few seconds for one image rather than 20 minutes, and the possibility to image with reduced photobleaching and phototoxicity compared to both epifluorescence microscopy and CLSM. The imaging speed advantage should be weighed against the superior sectioning strength of CLSM evident in Figure 3.8. Furthermore, the apparent change in image brightness in the direction of propagation of the illumination light sheet resulted in false representation of the sample brightness, however, a similar effect could be observed in the



CLSM data, albeit in depth rather than laterally, where the z slices deeper in the sample appeared dimmer than those at the top close to the coverslip.

The data show that a simple Gaussian light sheet is inferior to CLSM with respect to the sectioning strength, however, imaging speed on the order of a few seconds, depending on the exposure time of the camera, compared to 20 minutes for a three-frame-average image for CLSM on a comparable FOV. Furthermore, the photodose to the specimen to acquire the same signal is lower as is to be expected for LSM because the excitation is limited to the focal volume of the lens. In case of the Gaussian light sheet on the Mesolens, the sheet is an order of magnitude thicker than the focal plane, however, the excitation volume is still smaller than it is for CLSM. The proposed implementation of a two-photon excitation light strip that can be scanned over the FOV would theoretically be capable of reaching sub-micron axial resolution while simultaneously avoiding the shortcomings of the single photon Gaussian light sheet with respect to inhomogeneous brightness and striping artefacts. Submicron axial resolution across the full FOV of the Mesolens would even outperform non-diffracting beam light sheets. Ultimately, the approach had to be abandoned due to time constraints but should be revisited.

One could reduce the thickness of the Gaussian light sheet as well as the FOV of the Mesolens to generate a smaller and thinner light sheet, however, this would then beg the question why to use the Mesolens in the first place if not to use the full FOV. The alternative is to specifically develop a propagation-invariant light sheet for the Mesolens. This is work currently underway by one of my colleagues, Eliana Battistella.

# 4 Blind-SIM Mesoscopy (BlindMe)

## 4.1 Introduction

In this chapter, the possibility of implementing super resolution microscopy on the Mesolens using blind-SIM is presented, a method developed in the group of Rainer Heintzmann. Commonly used super resolution techniques are explained and deconvolution is presented in more detail including the underlying theory to show why blind-SIM was chosen to be used with the Mesolens.

### 4.1.1 Deconvolution

Deconvolution is the reverse operation of convolution which, in microscopy, is the blurring of the object by the PSF of the microscope system leading to the diffraction limited resolution of that system (D. A. Agard, 1984). In theory, knowing the PSF and the recorded image one can employ deconvolution to reconstruct the original object. However, in practice images are also subject to noise, which, due to its random nature, can never be exactly known. Furthermore, reconstruction algorithms are limited by computing power. More specifically, to accurately restore the object for every pixel, every other pixel would have to be considered which is computationally expensive. Additionally, inverse filtering the degraded image with the PSF would involve dividing by zero. Instead, deconvolution is performed by estimating a solution which is then degraded by the PSF and compared to the original image thus changing the inverse problem into a forward problem, circumventing division by very small values or by zero. This process is repeated a set number of times to minimise the difference between the degraded estimate and the raw data. Different algorithms have been developed over the

years to address noise and computing efficiency. The theory of deconvolution is explained in more detail in Chapter 4.2.

#### 4.1.2 Super resolution microscopy

Super resolution microscopy techniques have gained popularity owed to their ability to detect details in images that lay outside the diffraction limit of the microscope system used to acquire the raw data and in fact increase the resolution beyond what is possible with classical light microscopy. From a biology standpoint, SR microscopy is of interest because biochemical processes happen on the scale of molecules which are much smaller than the diffraction limited resolution of light microscopy. However, other imaging techniques capable of nanometer resolution like electron microscopy cannot be used with live specimen. This is the niche that SR microscopy tries to fill.

The most used techniques are stochastic optical reconstruction microscopy (STORM), photo-activated localisation microscopy (PALM), stimulated emission depletion (STED) microscopy and structured illumination microscopy (SIM).

STORM and PALM are known as single molecule localisation microscopy (SMLM) techniques and do not increase the resolution of the acquired images, but rather achieve their resolution improvement by processing several thousand images into one single image where each emitter is localised to  $\sim 10$  nm (E. Betzig *et al.*, 2006). This is possible because in each image only a subset of fluorescent molecules emits light and can then be localised using statistics. Therefore, imaging speed of the camera is of paramount importance, as well efficiency to manage the available photon budget. The performance of STORM and PALM depends on the number of collected photons.

In principle these two techniques function in the same manner, they require specific fluorophores that periodically emit light resulting in a blinking of single molecules in the final

image time series. Choosing the exposure correctly and collecting many images, on the order of  $10^4$ , one can say with confidence that each point light source corresponds to a single molecule. Through localisation algorithms the time series is then condensed to a single image with nanometre scale resolution.

STED is a point scanning technique with two beams; One excitation beam that is focused to a point at the sample to excite fluorescence in a small volume (S. W. Hell *et al.*, 1994). The second beam, the depletion beam, is shaped to a toroid which is centred around the focal point of the first beam. This toroid-shaped beam has a wavelength above the emission wavelength and stimulates the fluorescent molecules to relax to the ground state. This way, a volume around the focus of the excitation beam is not emitting fluorescence during detection and thus the detected signal is located to a smaller volume. This reduced emission volume is made smaller as the thickness of the toroid is increased, which in turn depends on the power of the depletion beam (T. A. Klar *et al.*, 2000). Resolutions on the order of 10s of nanometres are possible using STED. However, being a point scanning technique, STED is slow, even more so if the emission volume is on the order of 30 nm in the lateral dimension since this requires scanning more pixels, in fact at least 100 times more pixels in this example. For the Mesolens this disadvantage makes STED impractical to use due to the already large field of view and resolution of the system. However, there are practical limitations for the Mesolens that make STED impossible to implement. Firstly, the Mesolens scanning system is prone to mirror jitter, resulting in lateral artefacts when imaging at the diffraction limited resolution. Secondly, the Mesolens specimen stage undergoes z-drift of a few microns during long image acquisitions. An increase in the resolution of the CLSM imaging modality on the Mesolens by an order of magnitude is currently unattainable.

As described in Chapter 1.6, SIM is a super-resolution technique for widefield microscopy. It makes use of the formation of moiré patterns when two patterns of similar spatial frequency

overlap which then create a beating pattern of half the spatial frequency of the underlying patterns (M. G. L. Gustafsson, 2000; M. G. L. Gustafsson *et al.*, 2008). In the context of fluorescence microscopy, the two high frequency patterns are the distribution of the fluorescent molecules and an illumination pattern, usually a grating, that is projected into the sample. Carefully choosing the spatial frequency of the projected pattern close to the diffraction limit of the microscope allows for the observation of spatial frequencies that are outside the detection bandwidth of the microscope. Because the grating pattern is well known since it was deliberately chosen, the resulting images can be computationally processed to determine the underlying fluorophore distribution with a resolution two times better than the microscope diffraction limited resolution. The downside of SIM is the accuracy of the patterned illumination; thick or scattering samples are difficult to image with SIM because the illumination pattern becomes degraded which in turn reduces the effectiveness of the reconstruction algorithm. SIM does provide super-resolution, but it is not straightforward to implement with the Mesolens. Structured illumination would have to be introduced in the back-aperture plane of the condenser because the back focal plane of the objective is not accessible in the current Mesolens design. As a direct result, thick samples could not be imaged because the grating contrast would quickly deteriorate due to scattering.

This is where blind-SIM has an advantage. The illumination pattern as well as the underlying object are estimated and deconvolved in turn reaching a solution for both the pattern and the object (R. Heintzmann *et al.*, 2006; A. Jost *et al.*, 2015). The method works with degraded diffraction grating illumination and with random speckle illumination. A random speckle illumination setup has already been implemented with the Mesolens for the HiLo work described in Chapter 2 making blind-SIM a straightforward approach to try super-resolution microscopy on the Mesolens. The main disadvantage of blind-SIM is that it requires on the

order of 100 images with different illumination patterns to obtain one final image making it unsuited for live cell imaging with the Mesolens, however, the alternative methods outlined above cannot be used for live cell imaging on the Mesolens either and would require extensive work on the optical setup already in place.

## 4.2 Theory

An image formed by a microscope is a representation of the actual object at a finite resolution. In fluorescence microscopy, the resolution of a given microscope system is limited by the NA of the objective lens.

The process of blurring the object, or specimen, is described mathematically by the convolution of the object with the PSF of the microscope.

$$g(x, y, z) = o(x, y, z) \otimes h(x, y, z) \quad (21)$$

Where  $g(x, y, z)$  is the recorded image,  $o(x, y, z)$  is the true object,  $h(x, y, z)$  is the microscope point spread function and  $\otimes$  is the convolution operator. The inverse operation of this process is called deconvolution and computational deconvolution in image processing refers to the attempt to restore, at least in part, the object from the image by reversing the degrading effect of the PSF.

Convolution and thus deconvolution are rather complex operations, therefore, computational deconvolution makes use of the fact that convolution and deconvolution in the spatial domain become simple point by point multiplication and division in the frequency domain. Taking the Fourier transform of both sides of equation (19) yields

$$G(u, v, w) = O(u, v, w) * H(u, v, w) \quad (22)$$

Where  $G(u, v, w)$ ,  $O(u, v, w)$ ,  $H(u, v, w)$  are the Fourier transforms of  $g(x, y, z)$ ,  $f(x, y, z)$  and  $h(x, y, z)$  respectively and  $*$  is the multiplication operator. The Fourier transform of the point spread function is called the optical transfer function (OTF).

In theory, dividing the Fourier transform of the image by the OTF would restore the undegraded object, however, in practice this does not work. Firstly, a real image is subject to noise which contributes to the equation but cannot be exactly known and thus cannot be corrected. Equation (20) with added noise becomes

$$G(u, v, w) = O(u, v, w) * H(u, v, w) + \sigma(u, v, w) \quad (23)$$

where  $\sigma(u, v, w)$  represents the random noise associated with the image taken with the microscope system and should be understood as a combination of several noise sources (D. A. Agard, 1984). Any image taken with a camera has photon noise arising from the random times at which individual photons arrive at the detector. Photon noise can be modelled as a Poisson distribution. Furthermore, camera detectors are subject to Gaussian noise from dark current and sensor readout as well as hot and cold pixels, often referred to as salt and pepper noise.

Secondly, the OTF attenuates high spatial frequencies, i.e., it becomes very small, which in turn would result in very large values when used as a denominator. The highest frequencies in an image are typically random noise which would render any image, obtained by this simple approach of inverse filtering, useless.

Instead, deconvolution algorithms use iterative minimisation to converge to a solution. First, an initial estimate image of the object is made, usually this is simply the raw image. This initial estimate is then blurred by the PSF and the result is compared to the raw image. A new estimate is made taking the difference between the raw data and the previous estimate into account. This process is repeated, minimising the difference between blurred estimate and

original raw data, a set number of iterations or until a difference threshold is reached. This process is shown schematically in Figure 4.1. The function that estimates the difference between estimate and raw data is called the cost function.

$$cf = (g - f)^2 \quad (24)$$

With  $cf$ , the cost function,  $g$ , the raw data and  $f$ , the iteratively updated estimate of the algorithm.

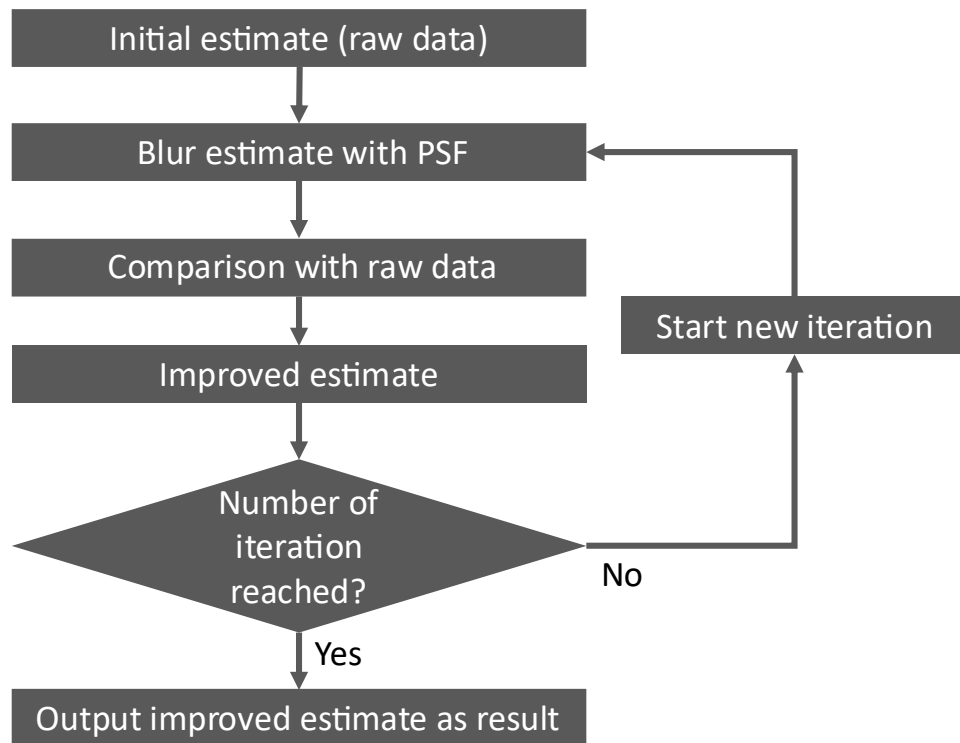


Figure 4.1: Simplified overview of an iterative minimisation deconvolution process. An initial estimate of the object is made which is blurred with the degrading function, in this case the microscope PSF. Subsequently, the error between blurred estimate and raw data is minimised over a set number of iterations and a final estimate is output as the result.

The iterative minimisation can be subjected to regularisation via boundary conditions to obtain a more accurate estimate. Specifically, in image restoration the result can be constrained to be smooth, since the object or specimen can be assumed to be relatively



smooth, and strictly non-negative, since negative values for pixel values in an image are physically meaningless.

A drop in intensity from maximum to zero from one pixel to the next might be a good estimate mathematically and thus result in a small cost function but would not accurately represent a real specimen. Smoothness constraints avoid such sharp edges and steep inclines, assuming a real object would get dimmer and brighter gradually rather than abruptly. In a way, such constraints work against the minimisation by forcing a smoother function to the data which would not go through all data points exactly but be a more reasonable representation of the object. To balance this trade-off, smoothness regularisation has an associated weight parameter that governs how much impact the constraint has on the final estimate. The regularisation is built into the minimisation algorithm as a term added to the cost function from equation (22). This term is also referred to as a penalty.

$$cf = (g - f)^2 + \lambda * p \quad (25)$$

With  $cf$ ,  $g$  and  $f$  as in equation (24),  $p$ , the regularisation term, also referred to as penalty and  $\lambda$ , the weight of the regularisation term on the cost function, typically a value much smaller than one. It can be seen from equation (25) that an algorithm that is built to minimise the cost function,  $cf$ , would be required to minimise not only the difference term,  $g-f$ , but also the regulariser term,  $\lambda * p$ . Thus, the regulariser can be used to promote or even enforce limitations on the form of the solution. In the context of deconvolution, the regulariser takes a form that promotes smoothness in the solution. The forms relevant for this work are explained in more detail in Chapter 4.2.1

Positivity constraints set the estimate equal to an auxiliary function which is then used as the estimate to compare to the raw data. The form of this auxiliary function can be very simple, e.g., the new estimate could be squared to force all values non-negative or only negative

numbers could be squared or the absolute value could be taken. Regardless of the type of auxiliary function employed, positivity constraints, unlike smoothness, obviously cannot be weighted.

In any case, constrained deconvolution is computationally more expensive than unconstrained deconvolution since there are more operations involved to reach a new estimate on every iteration. Furthermore, smoothness constraints require more iterations to converge to a solution with comparable minimisation difference value than unconstrained deconvolution since, as stated above, smoothness constraints work against the minimisation scheme to some extent. However, both smoothness and positivity constraint impose limitations on the estimated solution of the deconvolution that give more accurate results as they are a way to convey knowledge of the true underlying object to the algorithm. The regularisation options available in the blind-SIM toolbox used for the analysis of the data presented here will be discussed in more detail in the next section.

#### 4.2.1 Blind-SIM

In principle, blind-SIM deconvolution generates the result the same way as regular deconvolution via iterative minimisation. However, in addition to estimating the object and minimising the error between blurred estimate and raw data, the random speckle illumination is also estimated, blurred with the PSF, and is applied as illumination to the object estimate from which a second comparison is made to the raw data. Thus, two minimisation schemes are running in an alternating fashion a set number of total iterations, object iterations and illumination iterations. Figure 4.2 shows schematically the blind-SIM process.

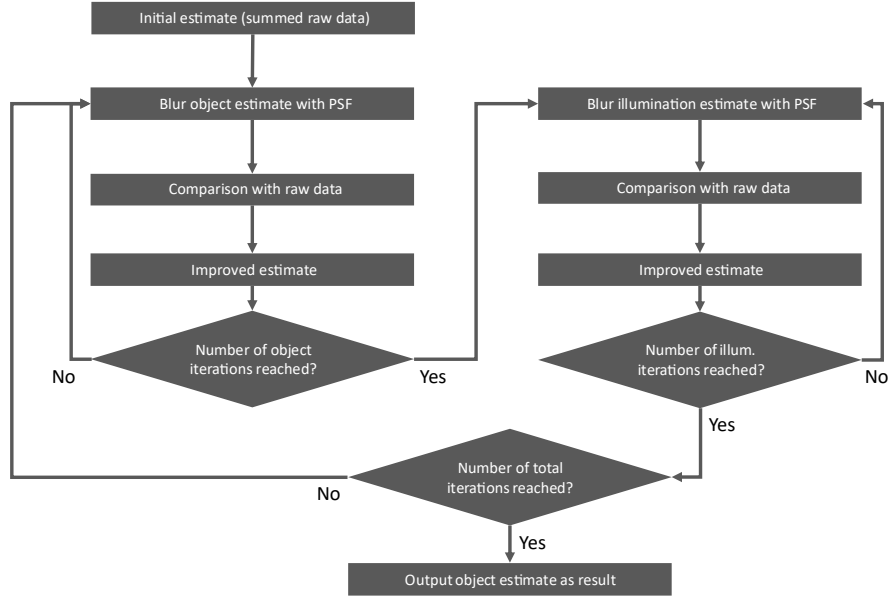


Figure 4.2: Schematic of the blind-SIM deconvolution algorithm. Fundamentally, blind-SIM deconvolution performs the same operations as regular deconvolution as depicted in Figure 4.1, however, both object and illumination are estimated in an alternating fashion resulting in a higher resolution final result.

Blind-SIM deconvolution can be subjected to the same constraints as regular deconvolution to enforce smoothness and positivity since it uses the same minimisation schemes. The available options for regularisation and positivity constraints vary in the mathematical form, i.e., the form the  $p$ -term in equation (23) takes as well as the type of auxiliary function for the positivity constraint. Available options for regularisation (smoothness constraint) were Good's Roughness (GR), Gradient Squared (GS), Total Variation (TV), Entropy (ER), Kevran (after Kervrann, but misspelled), and Laplacian.

Good's Roughness gives the regulariser term the form of the squared gradient divided by the absolute value of the estimate (I. J. Good *et al.*, 1971; P. J. Verveer *et al.*, 1999).

$$cf = (g - f)^2 + \lambda * \frac{|\nabla f|^2}{|f|} \quad (26)$$

Clearly, the penalty on the cost function is greater when the absolute value is smaller, so GR regularisation allows larger gradients where there is high signal but penalises fluctuation where there is low signal, i.e., background.

Gradient Squared regularisation has the form of simply the square of the gradient (A. Jost *et al.*, 2015).

$$cf = (g - f)^2 + \lambda * |\nabla f|^2 \quad (27)$$

Compared to GR regularisation, GS regularisation does not distinguish between regions of high or low signal.

The Total Variation regulariser results in the cost function of this form (L. I. Rudin *et al.*, 1992; F. Soulez *et al.*, 2012; A. Jost *et al.*, 2015).

$$cf = (g - f)^2 + \lambda * \sqrt{|\nabla f|^2 + \varepsilon^2} \quad (28)$$

Total Variation regularisation has been shown to preserve edges while denoising the image, however, textured data would also be smoothed (N. Dey *et al.*, 2006).  $\varepsilon$  is separate parameter in addition to the weight parameter,  $\lambda$ , in some regularisers to add a fixed value to the term and can be set independently from  $\lambda$  in the algorithm's implementation to control the impact the regulariser has on the cost function.

Entropy regularisation incurs a logarithmic penalty on the cost function (M. Arigovindan *et al.*, 2013).

$$cf = (g - f)^2 + \lambda * \ln(\varepsilon + (|f|^2 + SumOfHessianSquare)) \quad (29)$$

Where the *SumOfHessianSquare* is given by (M. Arigovindan *et al.*, 2013):

$$SumOfHessianSquare = \frac{\partial^2}{\partial x \partial x} f + \frac{\partial^2}{\partial y \partial y} f + \frac{\partial^2}{\partial x \partial y} f \quad (30)$$

Kervrann regularisation uses an adaptive window approach to regularise the smoothness of the estimate result. The implementation does not take the form of a simple penalty term as for the aforementioned regularisers and has been reported elsewhere (C. Kervrann *et al.*, 2007, 2008). For simplicity it was not repeated here.

Laplacian regularisation takes the form of a graph Laplacian matrix (J. Pang *et al.*, 2017).

$$cf = (g - f)^2 + \lambda * \sum_{(i,j) \in E} w_{ij} (f(s_i) - f(s_j))^2 \quad (31)$$

With  $(i,j)$ , the indices of neighbouring image patches,  $E$ , the edges connecting the neighbouring image patches,  $w_{ij}$ , the weight between patches, and  $(s_i, s_j)$ , the image patches. The regularisation term becomes small when neighbouring image patches have similar intensities while connected by large weights, thus local smoothness minimises the regulariser and the cost function.

Positivity constraints can also be added as another penalty term. However, the blind-SIM algorithm uses an auxiliary function that replaces the estimate. The auxiliary function was reported to be the square of the estimate (A. Jost *et al.*, 2015) but the application used to obtain the results shown in Chapter 4.4 offered a range of alternatives.

Firstly, a negative square auxiliary function could be chosen, which only squared negative input values and kept the estimate otherwise unchanged.

Next, a hyperbolic auxiliary function took the estimate as an input and gave the hyperbolic cosine as output.

Lastly, a piecewise fit auxiliary function gave a positive output by fitting piecewise curves when the input was negative.

Although the blind-SIM algorithm performs the same tasks as deconvolution, it is computationally more expensive for several reasons. Due to the nature of the speckle

illumination, blind-SIM requires on the order of 100 raw images with different translations or rotations of the same illumination pattern in each image to ensure that the entirety of the sample has been illuminated. In practice, summing all raw images results in an image that is equivalent to a widefield image which is also used as an initial estimate for the first round of object iterations. Furthermore, each iteration involves both object and illumination iterations for all raw images for a single output image. However, the patterned illumination has the effect that object and illumination are no longer independent and improved estimate of one allows for more accurate estimate of the other and vice versa. Clearly, this process is most effective when the speckle illumination coarseness is at the resolution limit of the microscope system.

## 4.3 Methods

### 4.3.1 Experimental setup

The setup used for HiLo mesoscopy shown in Chapter 2.2.2 has been used for random speckle illumination with minor adjustments and is shown schematically in Figure 4.3. The same diffuser affixed to the DC motor was used to generate the random speckle pattern, however, the motor was not used to turn the diffuser. Instead, the diffuser was rotated a small amount by hand to obtain a slightly different illumination pattern from one image acquisition to the next. The laser used was a Coherent Sapphire 488 continuous wave (CW) laser emitting at 488 nm and 4mW power. The beam was expanded to 12 mm, collimated, and guided onto the ground glass diffuser (DG20-1500, Thorlabs). The resulting speckle pattern was imaged by a 0.6 NA aspheric lens (ACL5040U-A, Thorlabs) onto the back aperture of the condenser lens thus illuminating the sample with a random speckle pattern that could be changed by rotating the diffuser. Images were acquired with the same CCD camera (VNP-29MC, Vieworks) used in the previous chapters.

To process the data with the blind-SIM toolbox, the same server described in Chapter 2.2.3 was used. This allowed tiled deconvolution to run for several hours or overnight without occupying a dedicated workstation. The GPU in the server could process tiles up to  $512 \times 512$  pixels of an image series with 100 images.

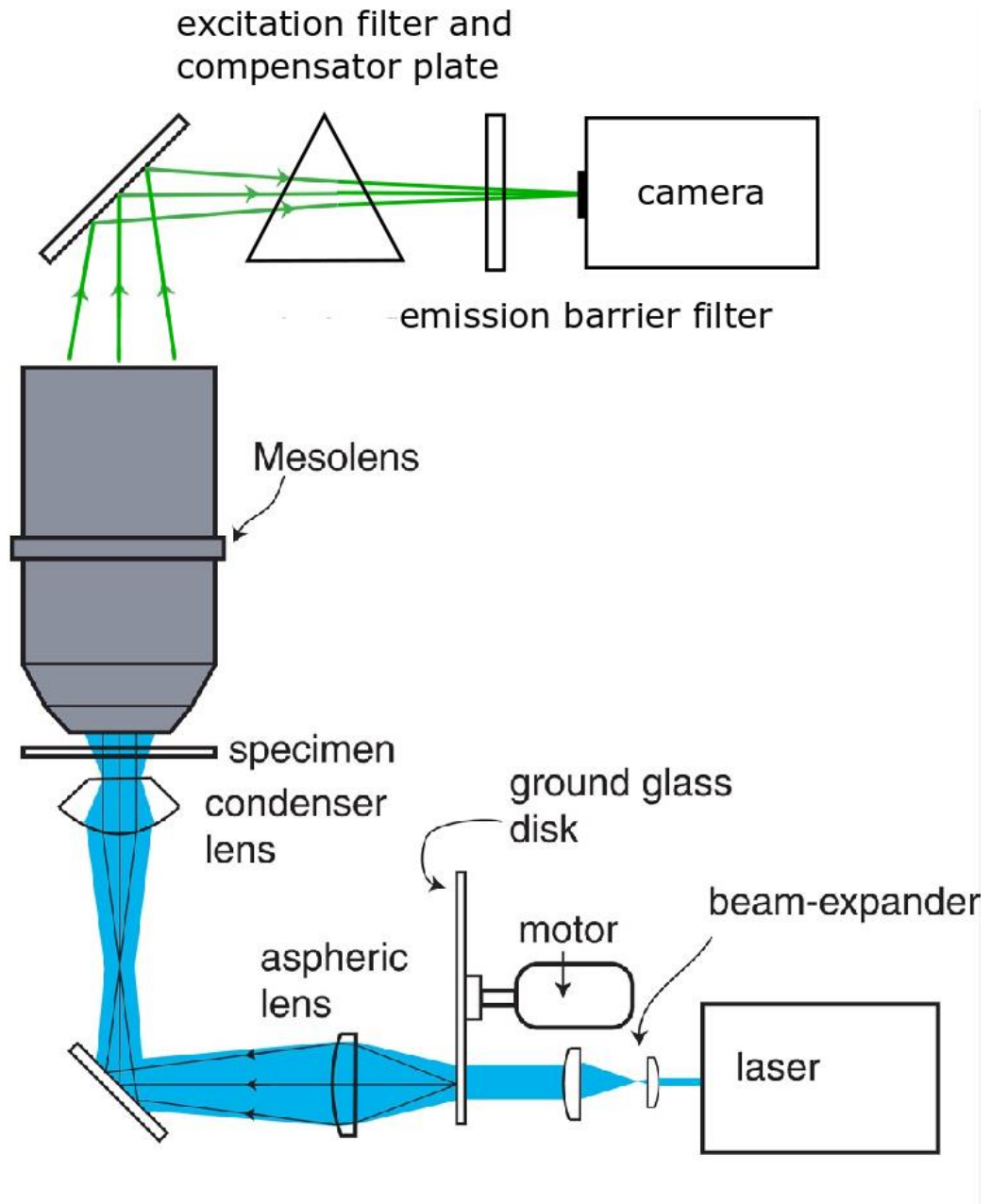


Figure 4.3: Experimental setup for random speckle illumination.. The ground glass diffuser disk was rotated by hand to obtain a different illumination pattern for each image acquisition. Apart from not using the motor to rotate the diffuser, the setup was identical to the one detailed in Chapter 2.2.2.

### 4.3.2 Blind-SIM toolbox graphical user interface (GUI)

The blind-SIM toolbox developed by Rainer Heintzmann and Aurelie Jost for the MATLAB script language has been implemented in an application with a graphical user interface (GUI) for convenient data analysis. The GUI consists of tabs which break the process up logically for the user. The 'data' tab is shown in Figure 4.4.

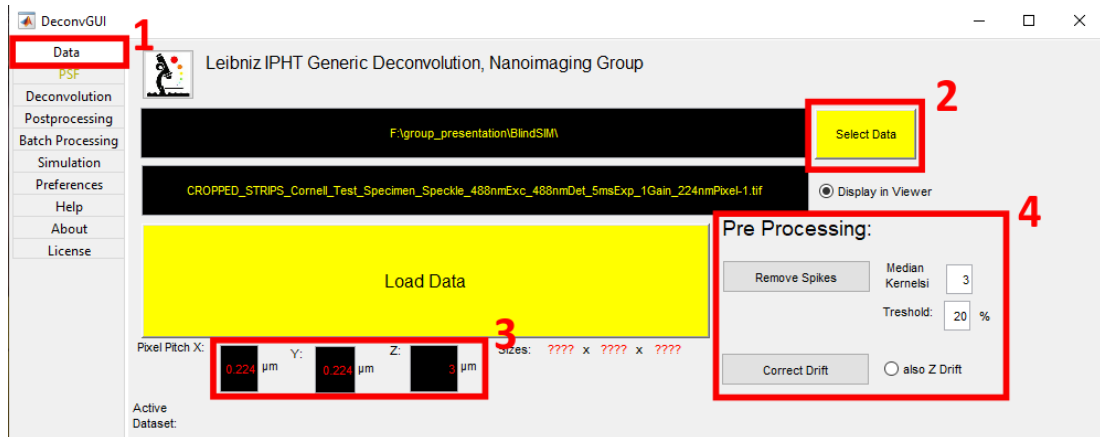


Figure 4.4: The 'Data' tab (1) of the blind-SIM toolbox GUI. The 'data' tab allowed loading and pre processing of data into the toolbox. The data was loaded via a standard file explorer which was launched by clicking 'Select Data' (2). If any metadata was found in the loaded image, the pixel scale (3) was filled automatically, otherwise the user must fill it manually. Pre-processing (4) allowed for hot pixel removal and drift correction.

Firstly, the data was loaded into the application via a standard file explorer window common in most modern applications. Any metadata the loaded data had was used to fill in the scale information, if none was found the user must fill these in manually. Hot pixel removal and drift correction were available as pre-processing steps. Hot pixels were removed using a median filter which size could be specified for all pixels that were closer than the specified threshold to saturation, i.e., the maximum possible value of the image loaded (e.g., 255 for an 8bit image).

After loading and pre-processing, the user was required to give the parameters for the PSF of the microscope system in the 'PSF' tab shown in Figure 4.5.



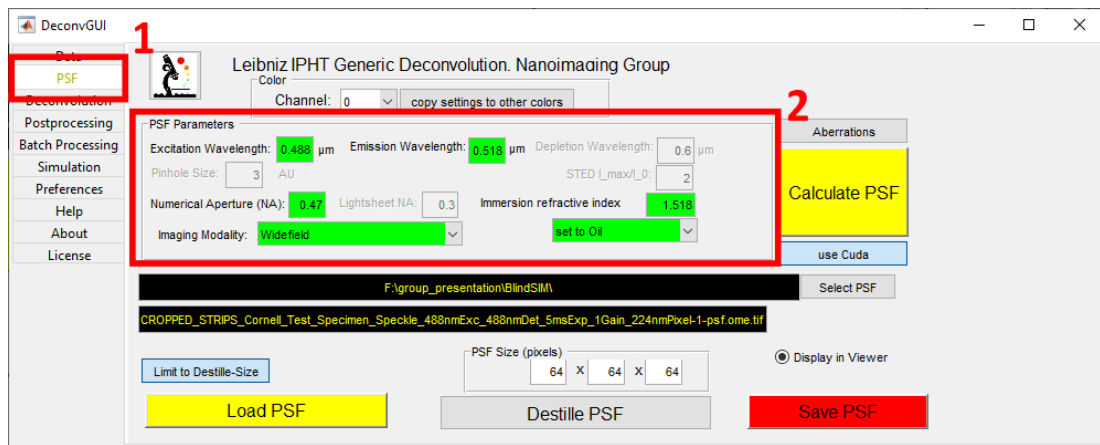


Figure 4.5: The 'PSF' tab (1) of the blind-SIM toolbox GUI. The 'PSF' tab required the user to input the microscope numerical aperture (NA) as well as excitation and emission wavelength, immersion medium and type of imaging (2) to accurately calculate a theoretical PSF. Only parameters necessary for a given type of imaging, in this case widefield, had to be given, parameters that were only relevant for other modalities were greyed out (e.g. 'pinhole size').

Putting in correct parameters was necessary to accurately calculate a theoretical PSF which was the chosen method for all processing performed. The GUI also had the option to include aberrations in the PSF generation or to distil a PSF from bead images, however, these options were not used as they would have included experimenting with and fine tuning many more parameters which was outside the scope of this work.

The 'deconvolution' tab contained the core functionality of the toolbox and is shown in Figure 4.6. The user had access to two-dimensional and three-dimensional deconvolution using different noise models, iterative minimisation, regularisers and positivity constraints. Noise model could be chosen between Gaussian and Poisson. Regularisation for smoothness and positivity constraint could be chosen as stated in Chapter 4.2.1.

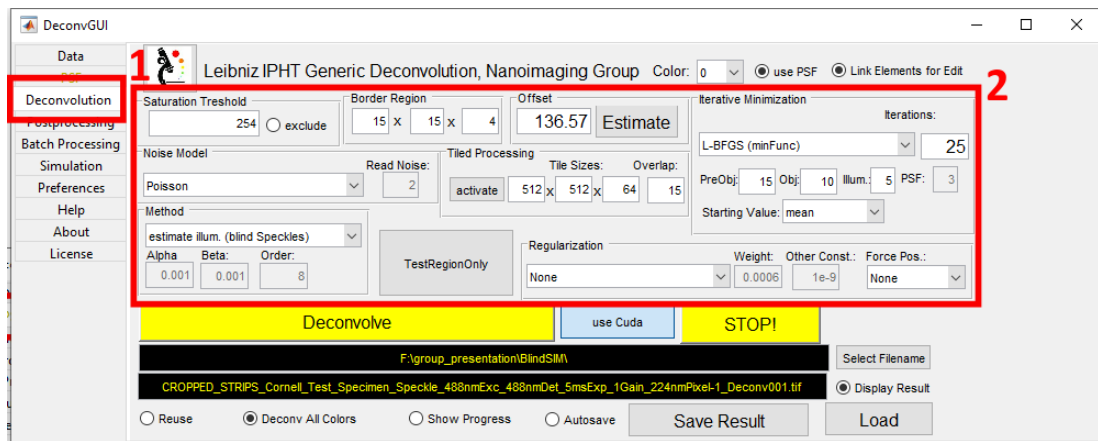


Figure 4.6: The 'deconvolution' tab (1) of the blind-SIM toolbox GUI. The core functions of the toolbox were executed in this tab. The user had access to all deconvolution parameters (2), some of which were optional; Saturation threshold, border region, offset, tiled processing and regularisation were not necessary to perform deconvolution. Only a noise model, method and iterative minimisation had to be chosen to perform a deconvolution. However, including optional parameters resulted in final images with more efficient background reduction as well as less noise and suppression of artefact formation.

Due to the high number of possible parameters many combinations are possible. Furthermore, in the case of blind-SIM the user can set the number of total iterations, object iterations and illumination iterations. Object and illumination were estimated one after the other a total number of times equal to the total number of iterations.

Lastly, the user had access to the 'post-processing' tab shown in Figure 4.7. For the purposes of this chapter, mean projections along the time axis were performed on the raw data to acquire widefield-equivalent images for comparison to the blind-SIM processed data and as a source image to perform 2D deconvolution, also to compare to the blind-SIM data.

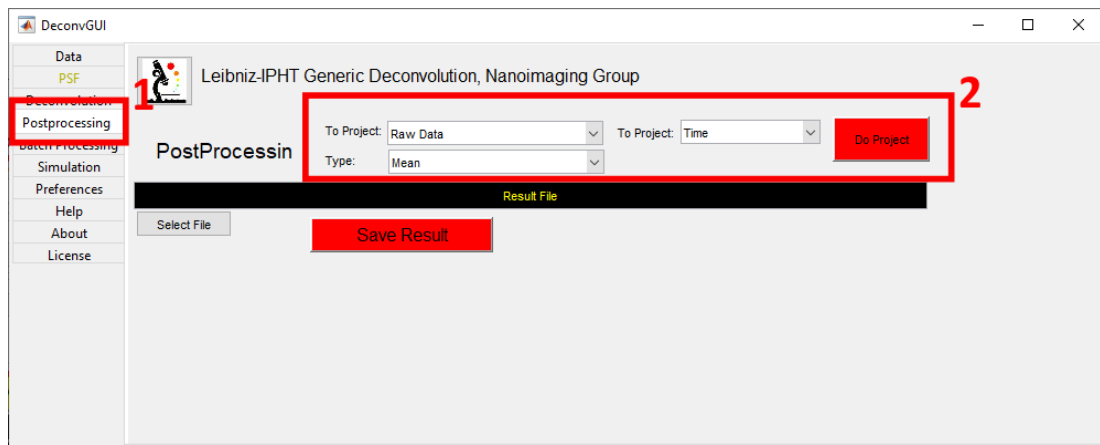


Figure 4.7: The 'post-processing' tab (1) of the blind-SIM toolbox GUI. Several types of projections along a chosen axis could be performed and then saved. Mean projections along the time axis were performed on the raw to acquire widefield-equivalent images for comparison.

To process a dataset with the blind-SIM method, several hundred images of the same z-slice are needed with different speckle illumination for each image. The setup used for HiLo mesoscopy shown in Chapter 2.2.2 was used to obtain these images. After each image, the diffuser was rotated a very small amount by hand before the next image was taken. 100 images of a given z-slice were obtained this way and then loaded into the application. The raw data properties were entered to ensure that the PSF generation would be accurate, most importantly the voxel size, detection NA, immersion medium and emission light wavelength.

### 4.3.3 MeT5A cell sample preparation

The MeT5A cell sample was prepared by my colleague Lisa Kölln.

The MeT5A cells were grown in RPMI-1640 447 media (Corning), supplemented with 10% (v/v) fetal bovine serum (FBS) (Labtech), 100 µg/ml 448 penicillin-streptomycin (Gibco), 1mM sodium pyruvate (Gibco), 2mM L-glutamine (Gibco) and 2mM 449 HEPES buffer solution (Gibco). All cells were kept at 37° and 5% CO<sub>2</sub> in a humidified atmosphere.

The cells were seeded 24 hours prior to imaging and then fixed in 4% Paraformaldehyde (PFA) at 37°C for 15 minutes. After fixation, the cells were washed twice in Phosphate Buffered

Saline (PBS) and incubated for 30 minutes at room temperature in IF buffer (PBS+2.5%, FBS+0.3%, TX 100). The cells were then stained with fluorescein phalloidin at concentration 1:100 simultaneously and then incubated again at room temperature for 60 minutes. Afterwards the cells were washed three times in with PBS and mounted in gelvatol onto a glass cover slip for imaging.

## 4.4 Results

As laid out in Chapter 4.3.2, the number of possible combinations to perform deconvolution is five positivity constraints and seven smoothness constraint regularisers for both the Gaussian and Poisson noise model, i.e. 35 combinations for each noise model. Unfortunately none of the available options can be categorically ruled out. However, testing a given minimisation method without any optional parameters, i.e., without regularisation and positivity constraint, gave a good indication of the potential quality that could be achieved when additional parameters were included. More to the point, if a minimisation method failed during processing, no amount of regularisation and positivity constraint produced results.

Qualitative assessment of the available algorithms using the same *Taraxacum* specimen as in Chapter 2.2.7 as a primary fluorescent specimen was possible by visually assessing the results. Also, artefacts could be spotted easily and, if possible, avoided by altering the parameters of the algorithm, e.g. the number of iterations.

Several image series of Actin network specimens were processed. Actin networks are commonly used to show the capability of super-resolution techniques due to their fine structure and overlapping features. They are also known for generating artefacts when using super-resolution algorithms which can be difficult to distinguish from genuine features of the specimen.

Lastly, the blind-SIM results were compared to the widefield data and regular 2D deconvolution.

#### 4.4.1 *Taraxacum* Pollen grain

Pollen grain was chosen as the first fluorescent specimen because its structure is well known, and artefacts can be spotted easily. Furthermore, a single grain is sufficiently small to process an image series in a few minutes. This was an important concern since using many different combinations of parameters was necessary to compare the results visually. The pollen images here were of the same specimen described in Chapter 2.2.7.

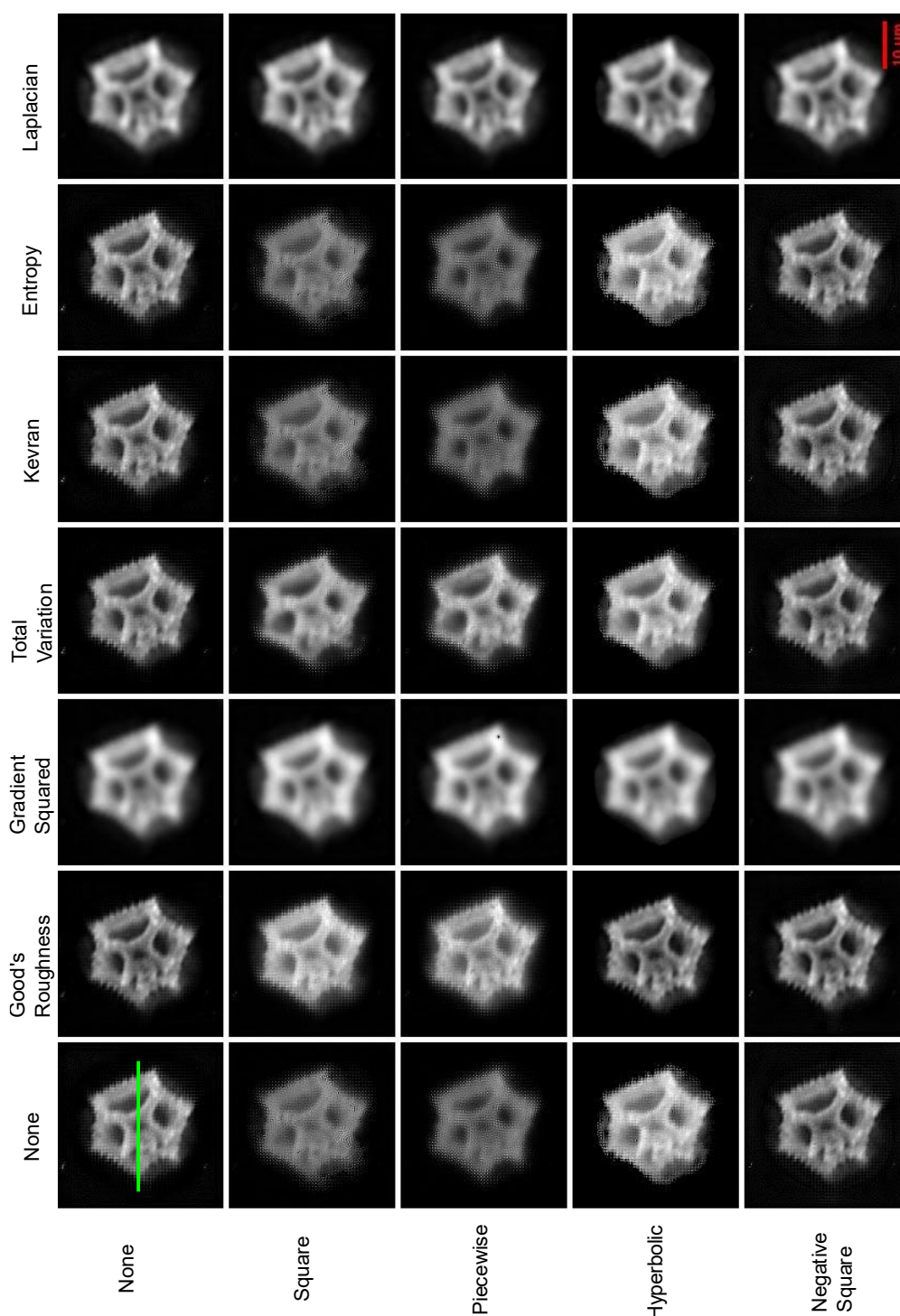


Figure 4.8: Gaussian noise model blind-SIM images of a single pollen grain using combinations of all regularisers and positivity constraint. It can be seen that all regularisers produced artefacts around the outer perimeter of the pollen grain or blurred the image to the point where some of the fine structure around the edge of the pollen grain were no longer visible. Artefact formation varied depending on the choice of regulariser and positivity constraint. In an effort to quantify the image quality, peak signal-to-noise ratio measurements were performed resulting in the table in Figure 4.10. The green line is the location of the line profile used in Figure 4.9. The line position was the same in each panel but is only shown once.

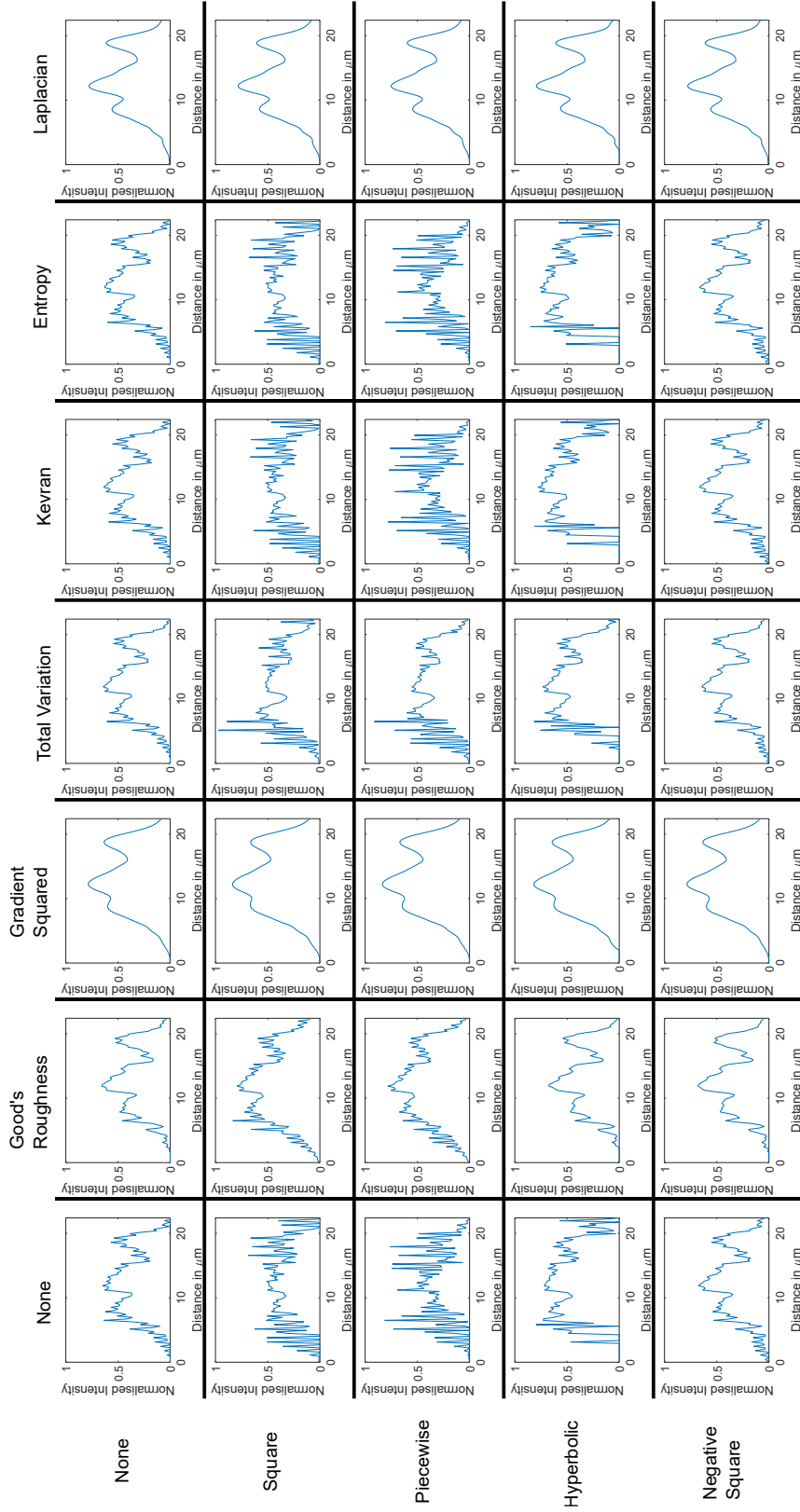


Figure 4.9: Line plots obtained from the data in Figure 4.8, the position of the line is indicated by the green line. Gradient Squared and Laplacian regularisers blurred the image and square, piecewise, and hyperbolic positivity constraints resulted in images dominated by noise.

There was artefact formation visible in most images that originated in the raw data. It is a re-occurring issue with the Mesolens camera image acquisition that a single pixel in the 3x3 grid that the sensor is moved through was brighter than the others. In Figure 4.8 this artefact formation can be seen around the edge of the pollen grain as a recurring pattern of bright and dim pixels. This slightly brighter pixel is usually not noticeable, but the deconvolution evidently exaggerated the effect.

	NoReg	GR	GS	TV	Kevran	Entropy	Laplacian
None	32.34	53.22	72.15	46.06	33.99	33.78	66.97
Square	24.64	42.42	69.50	36.86	24.69	25.12	69.74
Piecewise	26.11	43.27	67.60	34.49	25.85	26.72	71.56
Hyperbolic	31.42	60.51	72.32	42.16	31.57	30.75	69.94
Negative Square	29.04	50.70	72.15	39.28	26.84	30.03	67.13

Figure 4.10: Peak signal-to-noise ratio (pSNR) of the images in Figure 4.8. Values were colour coded for ease of reading. Between 30 and 65 were considered high pSNR, images with less than 30 pSNR were considered noise dominated while images with more than 65 pSNR were considered to have been blurred. This range was determined by using the highest pSNR of the images that had obvious artefact formation to be the lower bound and the lowest pSNR of the images that were blurred to be the upper bound of the range respectively.

For the Gaussian noise model data shown in Figure 4.8 and Figure 4.9, the Good's Roughness regulariser resulted in images that had reduced background and increased fine detail and the above-mentioned artefacts from the raw data were suppressed. The Gradient Squared and Laplacian regularisation resulted in blurred images to the point that the fine structure around the edges of the pollen grain was no longer visible. The remaining combinations resulted in noticeable artefact formation, degrading the image quality. The artefacts appear in the line plots in Figure 4.9 as high frequency, high amplitude signal which is absent in the widefield image.

To obtain a measure of the quality of the image, the peak signal-to-noise ratio (pSNR) was calculated by dividing the maximum intensity in the image by the noise standard deviation. The noise standard deviation was obtained by calculating the mean of the standard deviation of every pixel's immediate neighbourhood using a 3x3 pixel mask.



On visual inspection of the images in Figure 4.8 a pSNR range was then determined using the highest pSNR of the images with obvious artefact formation as the lower bound of the range and the lowest pSNR of the images that were blurred as the upper bound of the range. Images outside this pSNR range between 30 and 65 were considered combinations of regularisers and positivity constraints resulting in poor quality images. The weight parameter  $\lambda$  was 0.01 for all regularisers. Changing this parameter could have a positive effect on the regulariser performance but was ultimately not explored due to time constraints.

Taking into consideration the peak signal-to-noise ratio data from Figure 4.10, Good's Roughness outperformed the other regularisers and with hyperbolic positivity constraint resulted in a pSNR of 60.51. However, hyperbolic positivity constraint produced artefacts when used with any other regulariser, whereas no positivity constraint and negative square positivity constraint resulted in high pSNR values with all regularisers. Going forward with different specimens after the pollen grain, it was reasonable to reduce the number of combinations, ruling out GS and Laplacian altogether, as well as square, piecewise and hyperbolic positivity constraints, only working without regularisation or positivity constraint as an initial step and adding Good's Roughness regulariser and negative square positivity constraint.

Figure 4.11 shows the results using the Poisson noise model. Good's Roughness with no positivity constraint resulted in a pSNR of 64.71 representing the highest pSNR value within the range between 30 to 65 pSNR. To accurately evaluate the quality of these images, a ground truth would be required which was not obtained at the time. A straightforward way of obtaining a ground truth would have been to image the same pollen grain with a high NA lens and compare the processed data to that image. This should be considered in future studies using the blind-SIM method. Figure 4.12 and Figure 4.13 show the line profile through the center of the pollen grain and the obtained pSNR table respectively. The results were

consistent with those from Figure 4.8, Figure 4.9 and Figure 4.10 regarding artefact formation and blurred images. As for the Gaussian noise model processing, the lambda parameter was 0.01 for all regularisers and setting it to different values would have impacted the performance of each regulariser but due to time constraints, no parameter optimisation was performed.

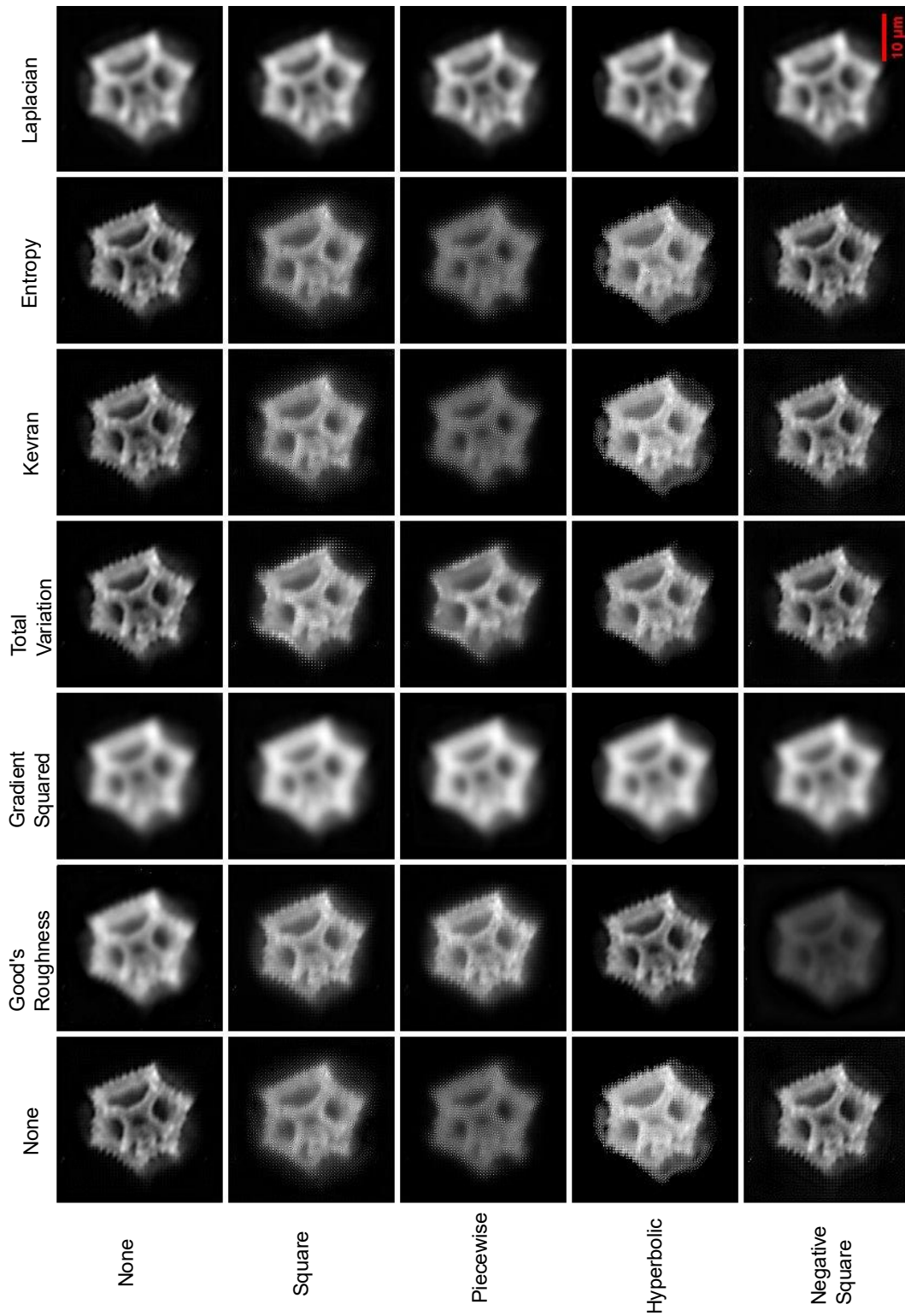


Figure 4.11: Poisson noise model blind-SIM deconvolution with all regularisers and positivity constraints. The Poisson noise model results were consistent with the Gaussian noise model results from Figure 4.8 with one notable exception. The Good's Roughness-negative square combination resulted in an overall dim image with little detail. There is a bright spot visible at the edge of the image which most likely negatively impacted the deconvolution minimisation algorithm for this particular combination of regulariser and positivity constraint.

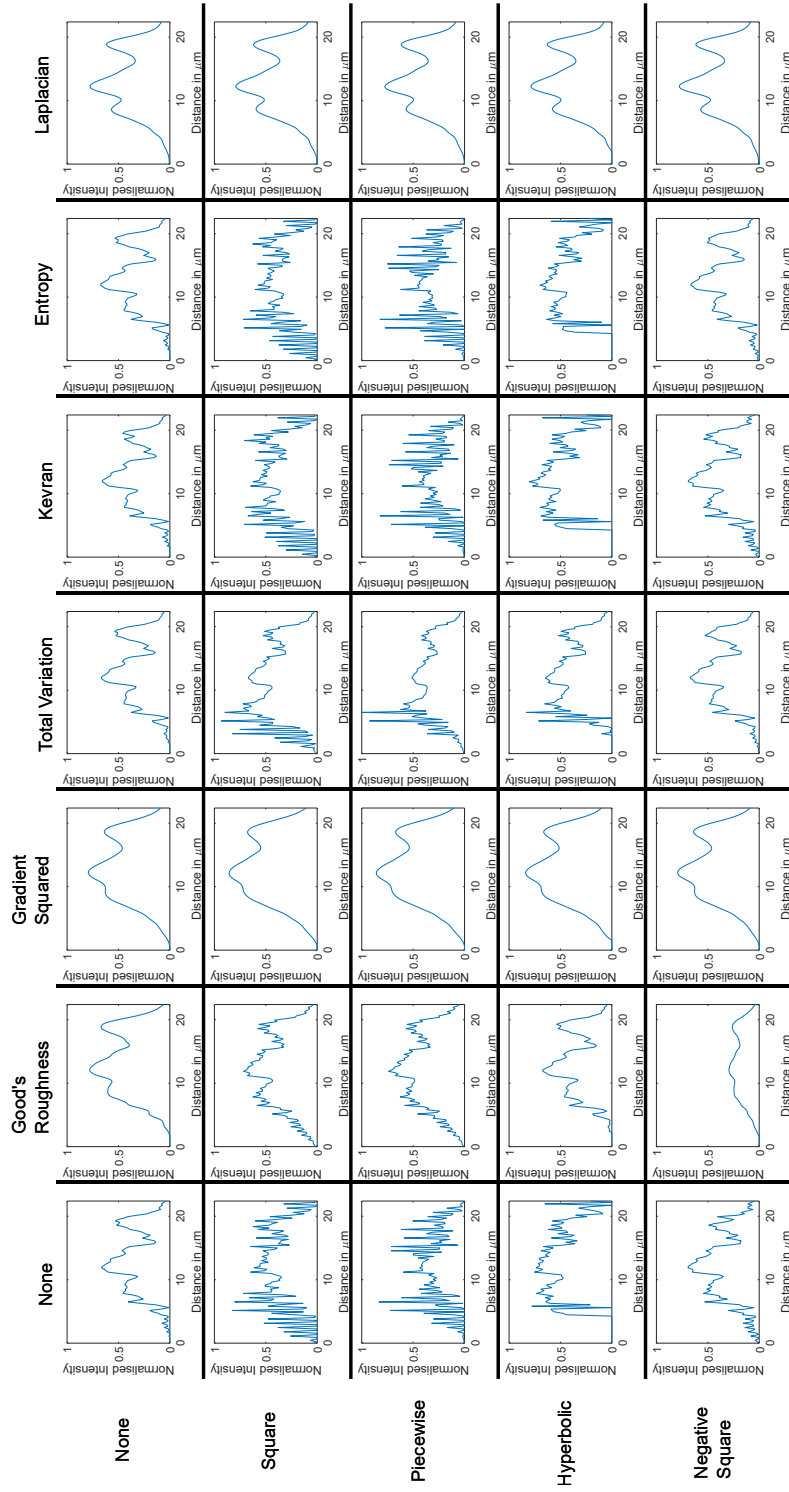


Figure 4.12: Line plots obtained from images in Figure 4.11. Results are consistent with the Gaussian noise model. The line plots of the blurred images resulting from Gradient Squared and Laplacian regulariser were lacking fine detail evident by the smooth shape with little contrast. Artefact formation appeared as high frequency noise in the plots (e.g., square and piecewise positivity constraint with no regulariser). The high frequency noise leads to low pSNR values and blurred images lead to high pSNR values outside the range between 30 and 65 shown in Figure 4.13.

	NoReg	GR	GS	TV	Kevran	Entropy	Laplacian
None	49.67	64.71	74.99	58.85	52.13	53.16	68.45
Square	19.37	49.06	71.51	34.49	19.54	21.03	70.30
Piecewise	25.27	50.54	72.25	49.58	24.56	24.20	71.49
Hyperbolic	28.03	61.00	74.11	53.13	29.01	31.59	70.64
Negative Square	30.74	157.53	74.96	50.32	30.73	44.67	68.75

Figure 4.13: Peak signal-to-noise ratio (pSNR) of the Poisson noise model data in Figure 4.11. As before the colour code was chosen to show pSNR values between 30 and 65 as green. The pattern from Figure 4.10 repeats itself with one notable exception of the GR-neg.sqr-combination. The image had significantly less brightness as well as very little detail after processing which resulted in the higher pSNR value due to the low variability in the intensity. As before, GS and Laplacian resulted in blurred images and square, piecewise, and hyperbolic positivity constraints produced noise and artefacts with most regularisers.

#### 4.4.2 Actin network

An image series of the same focal plane of Actin network of MeT5A cells was acquired in the same manner as was done for the pollen grain sample. As before, the data was processed using all combinations of regularisations and positivity constraints.

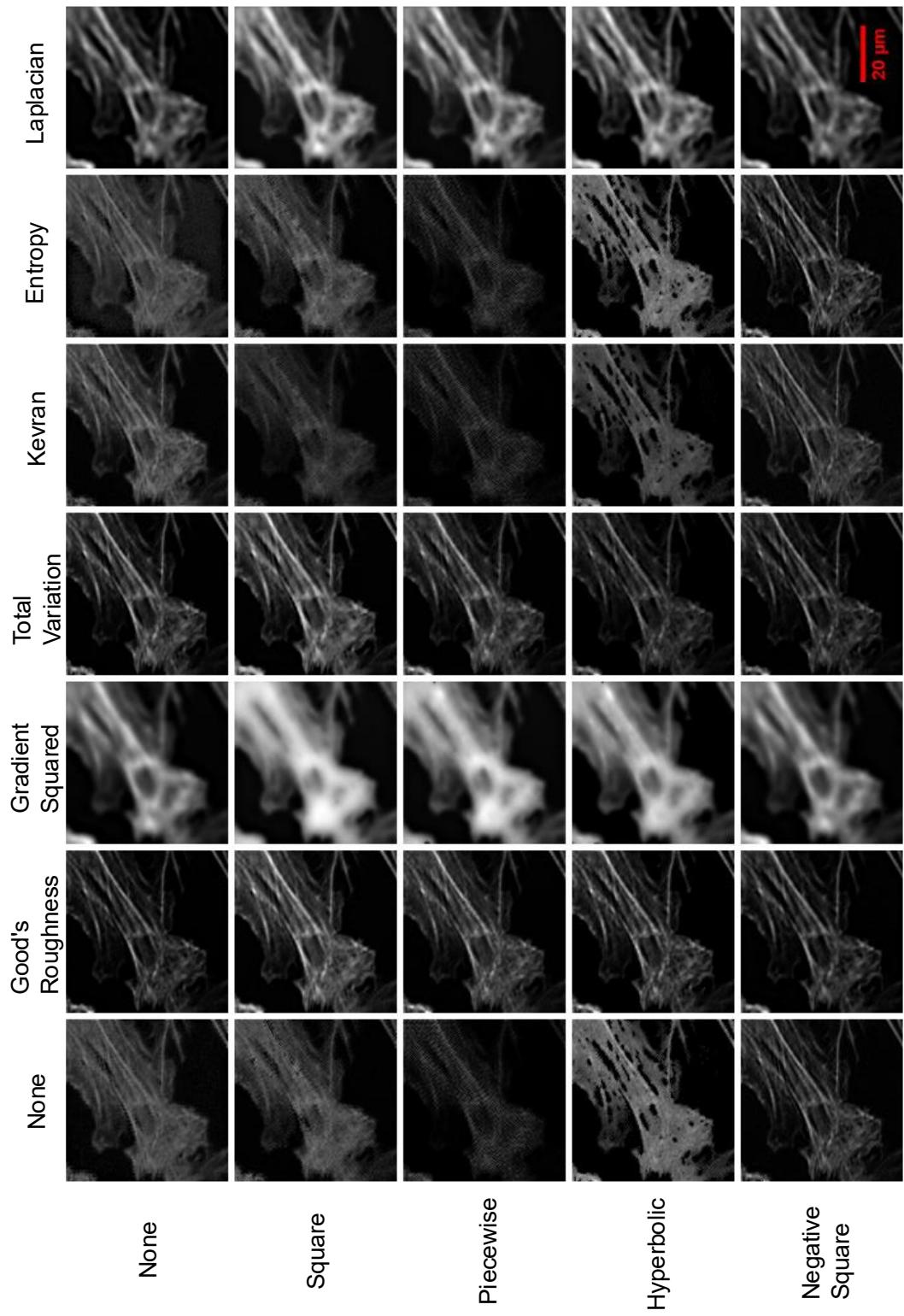


Figure 4.14: Actin network of Met5A labeled with fluorescein phalloidin processed using blind-SIM algorithm with the available range of regularisers and positivity constraints. The specimen was excited using 488 nm laser speckle illumination and 10 nm detection bandwidth centred at 520 nm. The Poisson noise model and L-BFGS update scheme were used. A vertical line was plotted to investigate the contrast and fine detail in the images. The plots are shown in Figure 4.15.

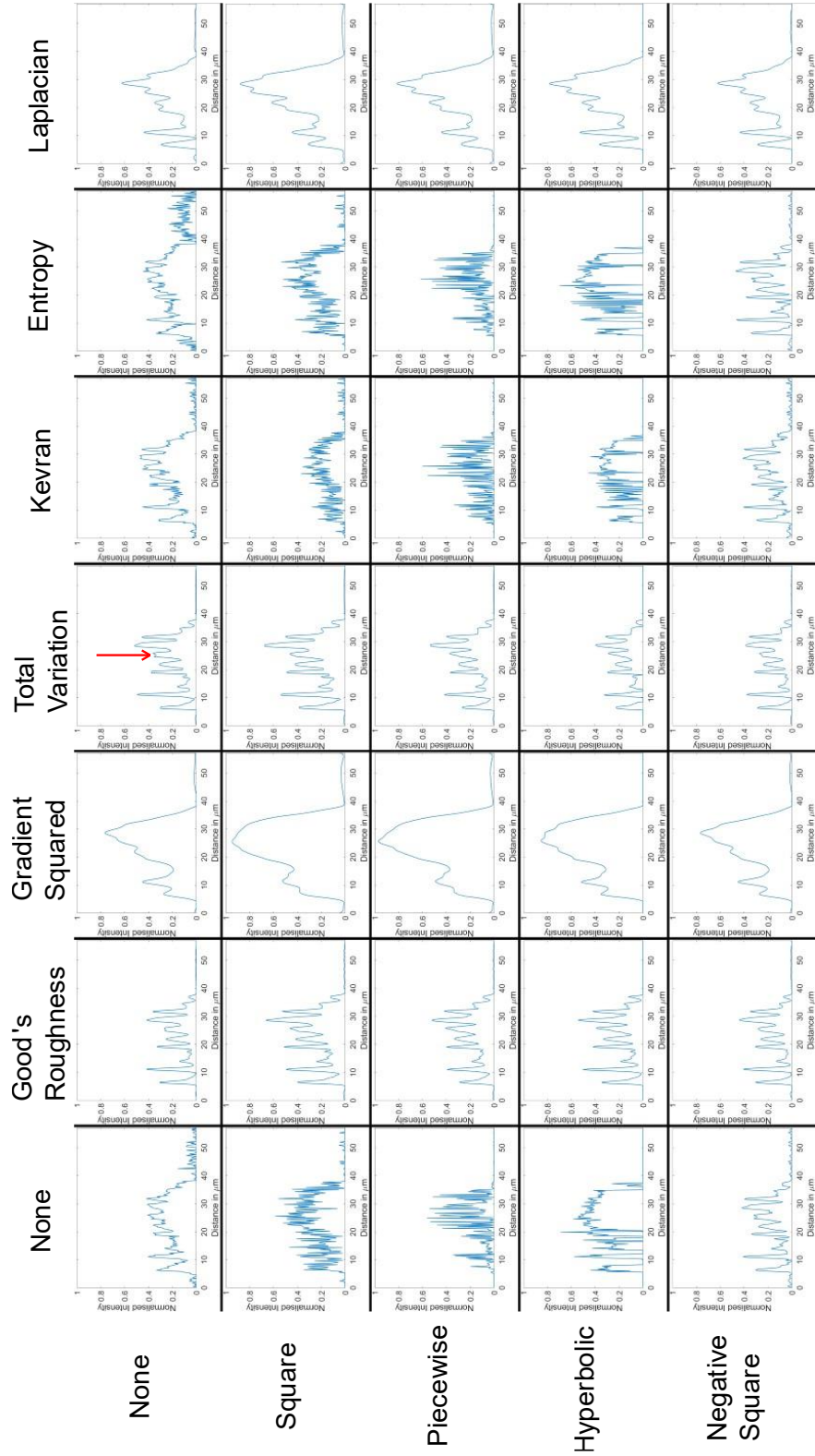


Figure 4.15: Plots of vertical line profiles through the centre of the images shown in Figure 4.14. Gradient Squared and Laplacian regularisers resulted in blurred images lacking all previously visible fine detail. Good's Roughness and Total Variation regularisers achieved narrow peaks and low noise as could also be seen from the peak signal-to-noise ratio (pSNR) when combined with the negative square positivity constraint.



	NoReg	GR	GS	TV	Kevran	Entropy	Laplacian
None	29.86	57.94	89.78	51.83	33.53	24.99	70.58
Square	14.05	45.55	85.58	46.08	19.13	15.61	68.73
Piecewise	16.11	54.02	85.02	59.00	14.29	16.19	71.30
Hyperbolic	17.85	48.06	86.81	67.04	22.50	16.50	58.72
Negative Square	42.99	61.77	89.90	62.80	39.63	38.71	72.64

Figure 4.16: Peak signal-to-noise ratio (pSNR) of the images in Figure 4.14. Color code refers to threshold values between 35 and 65 considered to have high enough SNR. Lower SNR images are dominated by high frequency noise and higher SNR are blurred to the point where fine detail is lost. The reference SNR of the widefield image was 15.21.

The above Figure 4.14, Figure 4.15 and Figure 4.16 show similar results to what was previously found; The Gradient Squared and Laplacian regularisers blurred the image to the point where all fine detail was lost. Kevran and entropy regularisers were dominated by noise except when used with negative square positivity constraint. No regulariser, Good's Roughness and TV achieved the best results in terms of fine detail and pSNR when combined with either no positivity constraint or negative square. The pSNR was only useful in combination with the line plots and processed images as judging from the pSNR alone, Gradient Squared and Laplacian regularisers performed very well resulting in pSNR values of over 80. However, the pSNR is high because the images were uniform and thus had very low noise standard deviation, but they lacked fine detail. Combining the data from the line plots and the pSNR table allowed to determine a small number of combinations for regulariser and positivity constraint that resulted in a pSNR within a range that, as with the pollen data, had as the lower bound the highest pSNR of noisy images and as the upper bound the lowest pSNR of the blurred images. The table has been colour coded with red (combinations that result in either high noise or blurred images) and green (combinations that resulted in images within the range between 30 and 65 pSNR).

Specifically, there is a double peak visible approximately at the 25  $\mu\text{m}$  tick in some of the panels in Figure 4.15 indicated by the red arrow. On close inspection of the line profiles and



the corresponding images, using TV regularisation with no positivity constraint showed the above-mentioned double-peak while maintaining a pSNR of 51.83. Although the pSNR was higher for GR and TV across all positivity constraint, one must consider that there was a trade-off between high pSNR and fine detail preservation. Furthermore, the way the pSNR was calculated, fine detail on the scale of three pixel (i.e., peak-trough-peak) would contribute to noise and lead to lower pSNR.

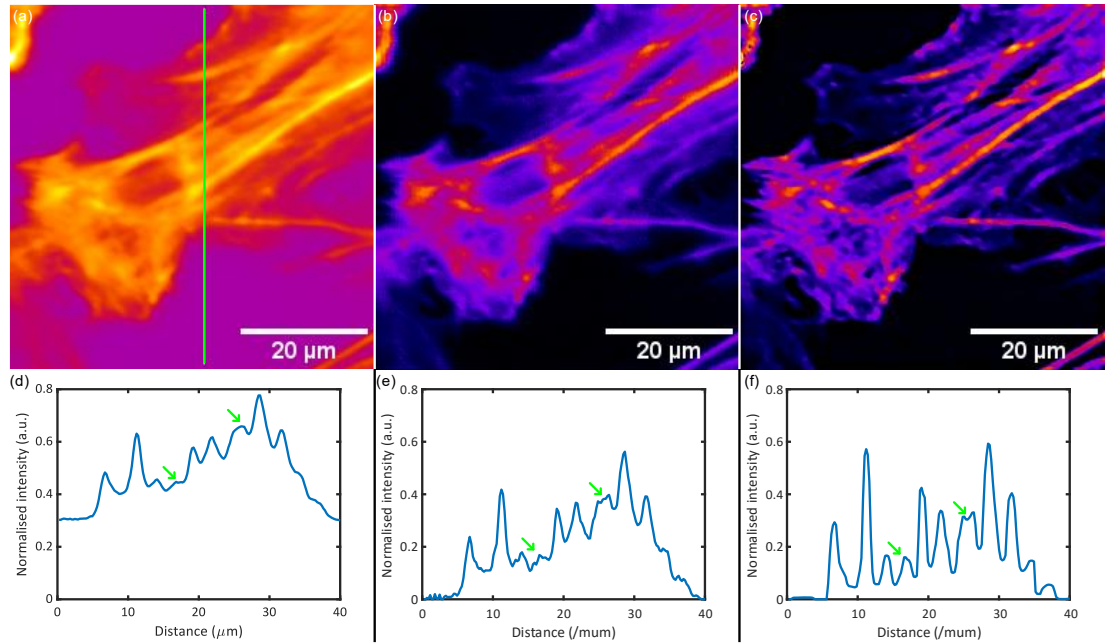


Figure 4.17: Comparison between widefield image, 2D deconvolution and blind-SIM. The widefield image (a) was used as the raw image for the 2D deconvolution (b) and the blind-SIM image (c) is the same as in Figure 4.14 with TV regulariser and no positivity constraint. The 2D deconvolution was also performed with TV regularisation and no positivity constraint at 200 iterations. Blind-SIM was processed at 25 total iterations with 10 object and 5 illumination sub-iterations per iteration. The weight of the regulariser was identical for both 2D deconvolution and blind-SIM at 0.01. Both 2D deconvolution and blind-SIM resulted in an image with reduced background and higher contrast which is shown in the line profiles (d), (e) and (f) that were taken from the images in (a), (b) and (c) respectively at the position indicated by the vertical green line in (a). What appears to be a double-peak indicated by the right green arrow in each plot was only clearly visible in the blind-SIM processed data but could be identified in the 2D deconvolution image also. The left green arrow indicates a single peak that could not be seen in the widefield image but could be identified in both 2D deconvolution and blind-SIM processed data.

Figure 4.17 shows a direct comparison between the widefield image, 2D deconvolution and blind-SIM with emphasis on the above-mentioned double-peak. It was absent in the

widefield data and could be identified in the 2D deconvolution data. However, the blind-SIM data had higher contrast than both widefield and 2D deconvolution which could be seen in the line plots as the blind-SIM data had a higher ratio between the peaks and troughs. Overall, the difference between widefield and blind-SIM was not on the order of two times better resolution that the algorithm was theoretically capable of but background rejection and sharpening could be observed, however, not unlike 2D deconvolution increased the contrast in the image.

As a final assessment, the upscaling of the algorithm was considered, using tiled processing on a larger image series with 2691 x 2337 pixels and 50 slices. The image was processed using the tiling facilities of the blind-SIM toolbox with a tile size of 256 x 256 x 50 resulting in 120 individual tiles to be processed. The complete process took approximately 10 hours to complete with the previously used setting of 25 total iterations, each consisting of 10 object and 5 illumination iterations. The final image showed tiling artefacts in areas where there was more background as well as within cells if a boundary between two tiles lay within it. These artefacts occurred when the solution to the deconvolution converged differently from one tile to the next. However, upscaling to larger images would be possible and requires tiling if GPU processing is desired as no GPU has sufficient memory to hold the data needed for processing large image series. The image is shown below in Figure 4.18. With tiling employed, an arbitrarily large image can be processed, however, the result shown here with the parameters stated above took over 9 hours of processing time and is almost 10 times smaller than a full FOV image of the Mesolens.

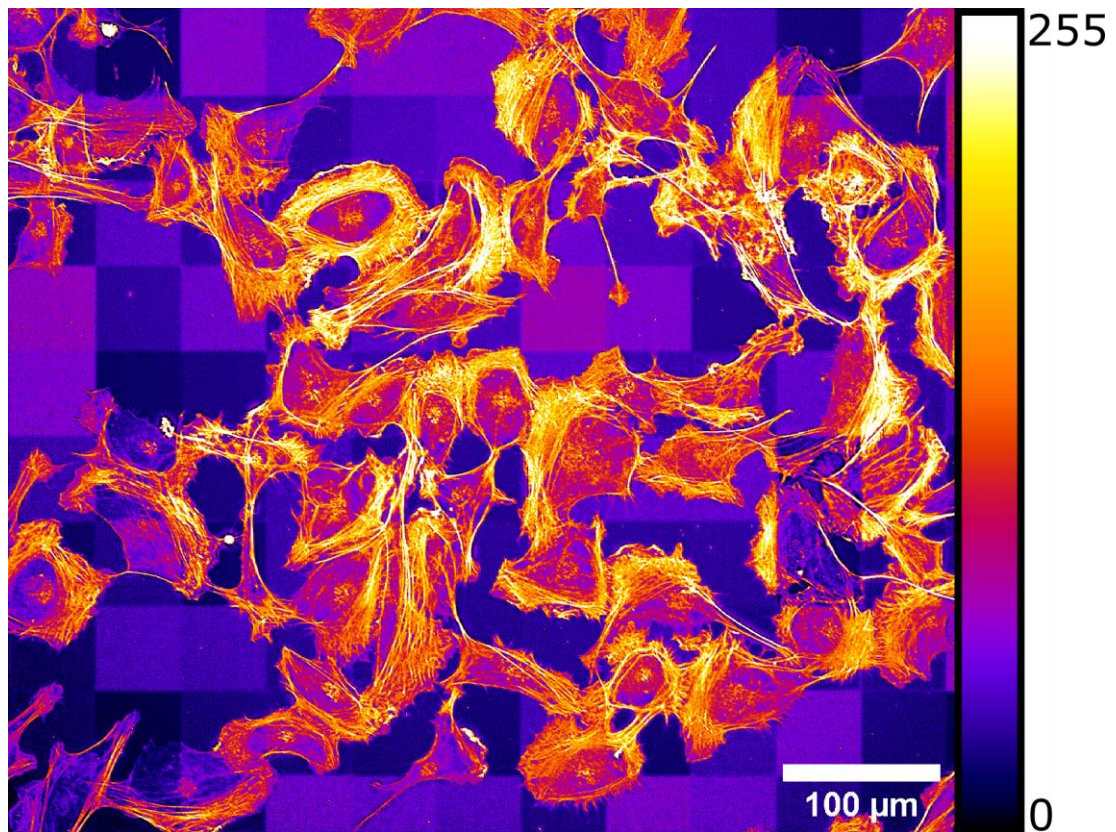


Figure 4.18: Result of tiled processing using the blind-SIM toolbox with a  $2691 \times 2337 \times 50$  image series of the same focal plane of MeT5A cells labelled with fluorescein phalloidin. Tiling artefacts formed between neighbouring tiles showing different brightness in both signal and background. The ‘Fire’ lookup table was chosen to clearly show the artefacts and the contrast was stretched, clipping a large portion of the bright pixels. In the high dynamic range version of the image, the artefacts are less noticeable but still present.

## 4.5 Discussion

Obtaining a ground truth for the data presented here would have helped to accurately quantify the image processing results. As it stands, the pSNR tables could be used as qualitative estimates for image quality but ultimately the range between 30 and 65 pSNR was chosen arbitrarily. In future studies, a ground truth could be obtained in two straightforward ways. Firstly, images of the same specimens could be taken with a high NA lens and then compared to the processed blind-SIM data. Secondly, regular SIM data of the same specimens could be obtained and then compared to the blind-SIM data. Due to time constraints neither of these two approaches could be implemented in this work.

Although the blind-SIM deconvolution algorithm can produce images with a resolution two times better than the diffraction limit, it could not achieve such a resolution improvement with the Mesolens setup. In fact, no resolution improvement could be observed in the processed data. The comparison between widefield data, 2D deconvolution and blind-SIM in Figure 4.17 showed that both 2D deconvolution and blind-SIM had a comparable effect on contrast improvement compared to the widefield image, however, blind-SIM deconvolution took on the order 15 minutes to process whereas 2D deconvolution took on the order of 15 seconds. This 60 times higher computational cost was due to the blind-SIM algorithm requiring on the order of 100 images and estimated both the illumination and object. Considering that the effect of the processing was comparable, the additional computational cost cannot be justified for the current blind-SIM implementation.

All regularisers were applied with the same weight parameter ( $\lambda$ ) of 0.01 which was the default setting in the deconvolution toolbox. It could be possible to obtain images with a high pSNR value within the range between 30 to 65 by tuning the weight parameter of each regulariser, however, parameter tuning would have required additional processing time and ultimately the objective of this work was not to optimise the deconvolution algorithm but to achieve super resolution imaging on the Mesolens. Further optimisation of the deconvolution and regularisation parameters could potentially yield improved results; However, it is unlikely that these would have improved resolution. More likely, the speckle illumination pattern used to acquire the data was too coarse to achieve a higher resolution. It has been shown in previous work (R. Heintzmann *et al.*, 2006; R. Ayuk *et al.*, 2013; A. Jost *et al.*, 2015) that the effective NA of the speckle illumination has a significant effect on the performance of the blind-SIM algorithm. More to the point, the illumination NA should be higher than the detection NA to achieve super-resolved images, e.g., for a detection NA of 0.45 an illumination NA of 0.6 was necessary. This combination is achievable on the

Mesolens, with a detection NA of 0.47 and the condenser NA of 0.6, however, the effective NA of the speckle illumination is also affected by the optics generating the speckle pattern. As stated in Chapter 4.3.1, the beam incident on the diffuser had a diameter of approximately 12 mm while the lens imaging the diffuser had a diameter of 50 mm. Even though that lens had a stated NA of 0.6, due to the small beam diameter compared to the lens diameter, the effective NA was much smaller, estimated on the order of 0.2 NA assuming a half angle of  $\sim 1/3$  the maximum half angle. The beam was expanded as wide as possible without striking any optics mounts or the holder of the diffuser. If new data for further blind-SIM work were to be acquired, the current setup would have to be rebuilt from the ground up, using larger diameter optics than the standard 1-inch optics presently used to build the illumination path. Furthermore, a larger diffuser would be necessary to accommodate the larger optics, which in turn would require rebuilding the mounting and rotation system. At the time of writing, these changes were outside of the scope of this project.

Further, the diffuser used in this work had a polished surface with an associated grit of 1200. While this was the highest grit available for an off-the-shelf diffuser, finer grit is certainly possible and would result in finer speckle illumination.

For the blind-SIM algorithm itself, it was shown here that Mesolens data could be processed, and upscaling did not cause any issues from a computational standpoint. While the computational cost of the algorithm scaled poorly with image size, an arbitrarily large dataset can be processed using tiled deconvolution. The processing time for the dataset with  $2691 \times 2337$  pixels and 50 images used in Figure 4.18 was on the order of 10 hours. Upscaling to full FOV Mesolens data would take several days of processing time for a single deconvolved image, which would make working with z-stacks practically impossible. This poor scaling with image size was to be expected as it already occurred when data was processed using the HiLo method in Chapter 2 and is unlikely to be resolved. Mesolens data is difficult to handle

computationally even with simple tasks, like visualisation. Complex algorithms that are computationally expensive are not practical to use with images of the size that the Mesolens generates.

Furthermore, the tiled processing produced artefacts in the form of brightness variation between tiles in the image. These artefacts occurred because the deconvolution converges to a solution at a different pace depending on the data in each run. Usually this is not noticeable if one processed a different dataset, however, each tile in the large set is processed individually and, more importantly, independently from the other tiles thus creating the 'checkerboard' pattern in the final image. It would be possible to tune the parameters such that the difference in the deconvolution result would be less noticeable but that would require tiled processing many times with slight alterations in the parameters which was deemed impractical due to the long processing time each run required.

Ultimately, any further work on super resolution mesoscopy using blind-SIM would focus on optimising the illumination to achieve a resolution improvement before any parameter optimisation would be performed. Nevertheless, optical sectioning was achieved, albeit not distinguishable from 2D deconvolution which was computationally much more efficient and thus preferable over blind-SIM if only optical sectioning is desired or achievable.

# 5 Conclusions and Future Work

## 5.1 Conclusions

### 5.1.1 HiLo Mesoscopy

With HiLo mesoscopy a viable optical sectioning method alternative to CLSM was demonstrated with the Mesolens with an acquisition speed of 30 seconds per full FOV HiLo image pair data compared to 15 minutes per three-frame-average CLSM image with an optical section thickness of  $5.2 \pm 0.3 \mu\text{m}$  compared to  $\sim 6 \mu\text{m}$  with CLSM capable of performing optical sectioning in thick and optically scattering specimens which present a challenge to CLSM. Additional processing time is required to obtain an optically sectioned image from the raw data. Typically, five minutes of processing time are required for a full FOV image pair, however, the processing time varies greatly depending on the computer used to run the process. The main drawbacks of the current implementation of the HiLo method were the high computational cost and slow switch between structured and uniform illumination. Both drawbacks can be addressed effectively by changing the existing spinning diffuser setup to a reflective diffuser that can be vibrated electronically, e.g. with a piezo-electric mirror. Furthermore, the homebuilt MATLAB script that was used to process the HiLo data could be either optimised or re-written in a more efficient programming language to reduce computational cost. With new cameras available now with higher framerates that can accommodate the high pixel count requirement of the Mesolens, this method would be a viable widefield optical sectioning imaging system.

### 5.1.2 Light Sheet Mesoscopy

In this work two approaches to perform optical sectioning using light sheet illumination on the Mesolens were explored. Firstly, an attempt was made to generate a thin strip of light using a pulsed IR laser to perform two-photon absorption swept light sheet microscopy, akin to the MesoSPIM initiative approach. Secondly a simple Gaussian light sheet illuminator was built.

Although the two-photon excitation setup did not perform as hoped and was abandoned in favour of the simple Gaussian light sheet illuminator, optically sectioned images were acquired albeit with a section thickness of 30  $\mu\text{m}$  at the center of the FOV diverging to 40  $\mu\text{m}$  at the edge of the FOV of the Mesolens. Compared to the 7  $\mu\text{m}$  axial resolution of the Mesolens, this light sheet thickness was an order of magnitude thicker than would have been desired for the Mesolens. The main advantage of the Gaussian illuminator is its simplicity as no scanning optics or other moving parts are required in the illumination beam path. Furthermore, the photodose to the specimen is low compared to CLSM to acquire equal fluorescence signal and the acquisition speed is limited only by the camera framerate. A dedicated project focused on a two-photon axially swept light sheet would be a viable approach to achieve thin optical sections on the Mesolens. Furthermore, at the time of writing this thesis, a thin light sheet using a non-diffracting Airy beam setup was built by fellow PhD student Eliana Batistella.

### 5.1.3 Blind-SIM mesoscopy

Super-resolution microscopy was attempted with the Mesolens using the blind-SIM approach. Unfortunately, super-resolution mesoscopy could not be achieved using the blind-SIM algorithm due to the low illumination NA of 0.2 in the current experimental setup. Images of a single pollen grain with a peak signal-to-noise ratio of 64.71 could be achieved



using the blind-SIM algorithm with Good's Roughness regularisation and no positivity constraint. Furthermore, images of Actin network of MeT5A cells were processed resulting in a peak signal-to-noise ratio of 67.04 using the Total Variation regulariser with hyperbolic positivity constraint compared to a pSNR of 15.21 for a widefield image of the Actin network. Parameter tuning for other regularisers and positivity constraint combinations would likely result in similar values for the pSNR, however, that approach was out of scope of this work. Furthermore, 2D deconvolution performed similarly to blind-SIM processing but at a fraction of the computation time, on the order of 60 times faster than blind-SIM. The additional computational cost cannot be justified for the current blind-SIM implementation.

To estimate the scalability of the algorithm, an image stack comprised of 50 slices with  $2691 \times 2337$  pixels per image was processed using tiled processing. Processing time was on the order of 10 hours, suggesting that full FOV Mesolens data would take approximately 4 days for a single slice and processing z-stacks would be practically impossible.

Larger optical elements would solve the issue of low effective illumination NA but require a complete overhaul of the illumination beam optical path. However, even if super-resolution was achieved with a future setup, the requirement to obtain 100s of images for a single super-resolved slice would only be practical when a faster camera is used together with structured illumination that can be rotated and/or translated quickly. As an optical sectioning method alone, blind-SIM was computationally too expensive and 2D or 3D deconvolution would be preferable.

To better quantify the performance of the blind-SIM algorithm, ground truth images of the processed samples would be necessary. In future studies using this algorithm, ground truths could be obtained by imaging the same specimens with a high NA lens and comparing the

processed data to that data. Alternatively, regular SIM could be used to acquire ground truth data for comparison.

## 5.2 Future Work

### 5.2.1 HiLo Mesoscopy

The HiLo mesoscopy approach showed satisfactory results with optically sectioned images. This could be performed even for large image stacks because each image pair can be processed independently from all other pairs, thus allowing the algorithm to run on a standard desktop PC. The server was primarily used for convenience rather than necessity. The acquisition speed could potentially be further increased by rebuilding the illumination setup; In its current implementation, the diffuser used to generate the speckle illumination is glued to a DC motor that can be rotated at high RPM to generate the uniform illumination. Instead, it would be possible to use a diffuse reflector held by a piezoelectric stage that can be vibrated rapidly to quickly alternate between speckle and uniform illumination (M. A. Lauterbach *et al.*, 2015). Alternatively, an optical fibre could be used in the existing epi-illumination path which could be vibrated to switch between structured and uniform illumination. Either of these approaches would eliminate the need for a bulky DC motor and allow faster acquisition of the image pairs. This could also be computer controlled and integrated into the acquisition software currently used on the Mesolens system together with a faster version of the HiLo algorithm, ideally written in C++ for high performance, to generate optical sections already during image acquisition. To complement a faster algorithm, it would be sensible to also invest in more powerful hardware, specifically a GPU that can easily handle the large file size. Additionally, the illumination optical train should have more than one excitation wavelength to allow multicolour imaging. The 488 nm Coherent laser could be replaced with a multi-line laser bank for easy alignment in the open beam setup.

### 5.2.2 Light Sheet Mesoscopy

The use of a Gaussian light sheet for single photon absorption was originally rejected in favour of the HiLo microscopy approach but towards the end of the project it was revisited. Now that the Gaussian light sheet is successfully implemented and its limitations understood, the two-photon excitation approach should be revisited. Although the initial tests were unsuccessful in generating a strip with a cylindrical lens that could generate sufficient fluorescence, the approach was never implemented in the Mesolens due to time constraints, this could be a suitable basis of another project.

The Gaussian light sheet illuminator could be extended with multi-wavelength excitation as suggested above for the HiLo setup since the current setup used the same light source already. This way, both setups could be made viable for multicolour imaging simultaneously. Furthermore, dual sided illumination could be implemented by splitting the excitation beam and guided each part from opposing sides under the Mesolens to alleviate some of the striping artefacts. However, this approach would necessitate alignment of two illumination arms which would complicate the setup significantly for not much gain other than more uniform illumination. It would make more sense to abandon the simple Gaussian light sheet and focus on the two-photon excitation approach.

Further, improvements in specimen prep should be considered. The resin embedding could be optimised by machining a mould with optically flat surfaces that could also be heated to accelerate resin hardening avoiding the formation of trapped air bubbles. The cut cuvette pieces should have larger base area to match the large coverslips and general size of the Mesolens and specimen stage.

### 5.2.3 Blind-SIM mesoscopy

The most important improvement for the blind-SIM mesoscopy setup would be to increase the illumination NA to generate a finer speckle pattern, on the order of the diffraction limit of the Mesolens. Furthermore, improving the rotation or translation mechanic for the speckle pattern would accelerate the image acquisition making the 100 frames required less of a bottleneck. The possible ideas for this have already been introduced in the future work for HiLo mesoscopy above and would be equally useful here. The key for more efficient data acquisition for both setups using the speckle illumination (HiLo and blind-SIM mesoscopy) would be to automate the image acquisition and speckle pattern control via software. This approach was considered during this project; however, software development takes a lot of time and was ultimately deemed out-of-scope for this work. It could potentially form the basis of a new project that would also involve rewriting the software currently used for image acquisition on the Mesolens.

As an additional method for SR imaging, the standard SIM approach could be implemented with a grating structure which could be coupled in through the epi-illumination port. This would allow a tried and tested approach for SR microscopy with the Mesolens; however it would only work with specimens up to a few micrometres thick. Nevertheless, for large FOV specimens, e.g., single cell layer neuronal prep specimens, this would be a viable approach.

## 6 Acknowledgement

I would like to thank my colleagues and fellow PhD students for the stimulating and helpful discussions during this project. Dr Ross Scrimgeour for his helpful insights into script writing and computational image analysis and Dr Peter Tinning for discussions around optical design and 3D modelling. Further, Dr Aimee Franssen, Katrina Wesencraft and Lisa Koelln for specimen preparation and advice for imaging said specimens. Dr Amos for offering his vast knowledge on specimen preparation, optical design and specifically the Mesolens.

Special thanks to my supervisor Prof Gail McConnell for her continued support, encouragement, understanding and mostly for her seemingly endless patience in the final stages of my project and writing this thesis. It cannot have been easy.

Further, I would like to thank my two children Elai and Ezra and our cat Leia for bringing joy and welcome distraction to my life during these trying times as well as my parents Joachim and Renate Schniete for their support regardless of what my aspirations were.

Lastly, I wish to thank Dr Jana Schniete for being a supportive, loving, and all-around amazing wife. Without her, I could not have undertaken this journey, let alone finish it.

## 7 References

Abbe, E. (1873) 'Beiträge zur Theorie des Mikroskops und der mikroskopischen Wahrnehmung', *Archiv für Mikroskopische Anatomie*, 9(1), pp. 413–418. doi: 10.1007/BF02956173.

Abbe, E. (1874) 'Neue Apparate zur Bestimmung des Brechungs- und Zerstreuungsvermögens fester und flüssiger Körper', *Jenaische Zeitschrift für Naturwissenschaft*, 8, pp. 96–174.

Abbe, E. (1881) 'On the Estimation of Aperture in the Microscope', *Journal of the Royal Microscopical Society*, 1(3), pp. 388–423. doi: 10.1111/j.1365-2818.1881.tb05909.x.

Abdul Rahman, N. Z., Greenwood, S. M., Brett, R. R., Tossell, K., Ungless, M. A., Plevin, R. and Bushell, T. J. (2016) 'Mitogen-Activated Protein Kinase Phosphatase-2 Deletion Impairs Synaptic Plasticity and Hippocampal-Dependent Memory', *Journal of Neuroscience*, 36(8), pp. 2348–2354. doi: 10.1523/JNEUROSCI.3825-15.2016.

Agard, D. A. (1984) 'Optical Sectioning Microscopy: Cellular Architecture in Three Dimensions', *Annual Review of Biophysics and Bioengineering*, 13(1), pp. 191–219. doi: 10.1146/annurev.bb.13.060184.001203.

Amor, R., Mahajan, S., Amos, W. B. and McConnell, G. (2015) 'Standing-wave-excited multiplanar fluorescence in a laser scanning microscope reveals 3D information on red blood cells', *Scientific Reports*, 4(1), p. 7359. doi: 10.1038/srep07359.

Amor, R., McDonald, A., Trägårdh, J., Robb, G., Wilson, L., Abdul Rahman, N. Z., Dempster, J., Amos, W. B., Bushell, T. J. and McConnell, G. (2016) 'Widefield Two-Photon Excitation without Scanning: Live Cell Microscopy with High Time Resolution and Low Photo-Bleaching',

*PLOS ONE*. Edited by T. Abraham, 11(1), p. e0147115. doi: 10.1371/journal.pone.0147115.

Amos, W. B., McConnell, G. and Wilson, T. (2011) 'Confocal Microscopy', in Egelman, E. H. (ed.) *Comprehensive Biophysics*. 1st edn. Elsevier B.V., pp. 3–23. Available at: [https://pure.strath.ac.uk/portal/files/14152084/Confocal\\_microscopy\\_Amos\\_McConnell\\_Wilson.pdf](https://pure.strath.ac.uk/portal/files/14152084/Confocal_microscopy_Amos_McConnell_Wilson.pdf).

Amos, W. B. and White, J. G. (2003) 'How the confocal laser scanning microscope entered biological research', *Biology of the Cell*, 95(6), pp. 335–342. doi: 10.1016/S0248-4900(03)00078-9.

Arigovindan, M., Fung, J. C., Elnatan, D., Mennella, V., Chan, Y.-H. M., Pollard, M., Branlund, E., Sedat, J. W. and Agard, D. A. (2013) 'High-resolution restoration of 3D structures from widefield images with extreme low signal-to-noise-ratio', *Proceedings of the National Academy of Sciences*, 110(43), pp. 17344–17349. doi: 10.1073/pnas.1315675110.

Arndt-Jovin, D. J. and Jovin, T. M. (1989) 'Chapter 16 Fluorescence Labeling and Microscopy of DNA', in *Methods in Cell Biology*, pp. 417–448. doi: 10.1016/S0091-679X(08)60989-9.

Ayuk, R., Giovannini, H., Jost, A., Mudry, E., Girard, J., Mangeat, T., Sandeau, N., Heintzmann, R., Wicker, K., Belkebir, K. and Sentenac, A. (2013) 'Structured illumination fluorescence microscopy with distorted excitations using a filtered blind-SIM algorithm', *Optics Letters*, 38(22), p. 4723. doi: 10.1364/OL.38.004723.

Baeyer, A. (1871) 'Über eine neue Klasse von Farbstoffen', *Berichte der Deutschen Chemischen Gesellschaft*, 4(2), pp. 555–558. doi: 10.1002/cber.18710040209.

Bartels, M., Krenkel, M., Haber, J., Wilke, R. N. and Salditt, T. (2015) 'X-Ray Holographic Imaging of Hydrated Biological Cells in Solution', *Physical Review Letters*, 114(4), p. 048103. doi: 10.1103/PhysRevLett.114.048103.



Bassi, A., Schmid, B. and Huisken, J. (2015) 'Optical tomography complements light sheet microscopy for in toto imaging of zebrafish development', *Development*, 142(5), pp. 1016–1020. doi: 10.1242/dev.116970.

Becker, K., Jährling, N., Kramer, E. R., Schnorrer, F. and Dodt, H. U. (2008) 'Ultramicroscopy: 3D reconstruction of large microscopical specimens', *Journal of Biophotonics*, 1(1), pp. 36–42. doi: 10.1002/jbio.200710011.

Betzig, E., Patterson, G. H., Sougrat, R., Lindwasser, O. W., Olenych, S., Bonifacino, J. S., Davidson, M. W., Lippincott-Schwartz, J. and Hess, H. F. (2006) 'Imaging Intracellular Fluorescent Proteins at Nanometer Resolution', *Science*, 313(5793), pp. 1642–1645. doi: 10.1126/science.1127344.

Bhattacharya, D., Singh, V. R., Zhi, C., So, P. T. C. and Barbastathis, G. (2012) 'Three dimensional HiLo-based structured illumination for a digital scanned laser sheet microscopy (DSLM) in thick tissue imaging', *Optics Express*, 20(25), pp. 27337–27347.

Born, M. and Wolf, E. (1970) *Principles of Optics*. 4th edn. Oxford: Pergamon Press.

Buytaert, J. A. N., Descamps, E., Adriaens, D. and Dirckx, J. J. J. (2012) 'The OPFOS Microscopy Family: High-Resolution Optical Sectioning of Biomedical Specimens', *Anatomy Research International*, 2012, pp. 1–9. doi: 10.1155/2012/206238.

Centonze, V. E. and White, J. G. (1998) 'Multiphoton Excitation Provides Optical Sections from Deeper within Scattering Specimens than Confocal Imaging', *Biophysical Journal*. Elsevier, 75(4), pp. 2015–2024. doi: 10.1016/S0006-3495(98)77643-X.

Cheng, P.-C. (2006a) 'Interaction of Light with Botanical Specimens', in *Handbook of Biological Confocal Microscopy*, pp. 414–441.

Cheng, P.-C. (2006b) 'The Contrast Formation in Optical Microscopy', in *Handbook of*

*Biological Confocal Microscopy*, pp. 162–206.

Conchello, J.-A. and Lichtman, J. W. (2005) 'Optical sectioning microscopy', *Nature Methods*, 2(12), pp. 920–931. doi: 10.1038/nmeth815.

Dailey, M. E., Manders, E., Soll, D. R. and Terasaki, M. (2006) 'Confocal Microscopy of Living Cells', in *Handbook of Biological Confocal Microscopy*, pp. 381–398.

Dean, K. M., Roudot, P., Welf, E. S., Danuser, G. and Fiolka, R. (2015) 'Deconvolution-free Subcellular Imaging with Axially Swept Light Sheet Microscopy', *Biophysical Journal*. The Authors, 108(12), pp. 2807–2815. doi: 10.1016/j.bpj.2015.05.013.

Denk, W., Strickler, J. H. and Webb, W. W. (1990) 'Two-photon laser scanning fluorescence microscopy.', *Science*, 248(4951), pp. 73–76. doi: 10.1126/science.2321027.

Dey, N., Blanc-Feraud, L., Zimmer, C., Roux, P., Kam, Z., Olivo-Marin, J.-C. and Zerubia, J. (2006) 'Richardson–Lucy algorithm with total variation regularization for 3D confocal microscope deconvolution', *Microscopy Research and Technique*, 69(4), pp. 260–266. doi: 10.1002/jemt.20294.

Diaspro, A., Bianchini, P., Vicidomini, G., Faretta, M., Ramoino, P. and Usai, C. (2006) 'Multi-photon excitation microscopy', *BioMedical Engineering OnLine*, 5(1), p. 36. doi: 10.1186/1475-925X-5-36.

Diaspro, A., Chirico, G., Usai, C., Ramoino, P. and Dobrucki, J. (2006) 'Photobleaching', in *Handbook of Biological Confocal Microscopy*, pp. 690–702.

Duncan, D. D., Kirkpatrick, S. J. and Wang, R. K. (2008) 'Statistics of local speckle contrast', *Journal of the Optical Society of America A*, 25(1), p. 9. doi: 10.1364/JOSAA.25.000009.

Dunsby, C. (2008) 'Optically sectioned imaging by oblique plane microscopy', *Optics Express*, 16(25), p. 20306. doi: 10.1364/OE.16.020306.

- Engelbrecht, C. J., Voigt, F. and Helmchen, F. (2010) 'Miniaturized selective plane illumination microscopy for high-contrast in vivo fluorescence imaging.', *Optics letters*, 35(9), pp. 1413–5. doi: 10.1364/OL.35.001413.
- Fahrbach, F. O., Gurchenkov, V., Alessandri, K., Nassoy, P. and Rohrbach, A. (2013) 'Light-sheet microscopy in thick media using scanned Bessel beams and two-photon fluorescence excitation', *Optics Express*, 21(11), p. 13824. doi: 10.1364/OE.21.013824.
- Flemming, W. (1878) 'Zur Kenntnis der Zelle und ihrer Teilungs-Erscheinungen', *Schriften des Naturwissenschaftlichen Vereins für Schleswig-Holstein*, 3(1), pp. 23–27.
- Fu, Q., Martin, B. L., Matus, D. Q. and Gao, L. (2016) 'Imaging multicellular specimens with real-time optimized tiling light-sheet selective plane illumination microscopy', *Nature Communications*. Nature Publishing Group, 7, pp. 1–10. doi: 10.1038/ncomms11088.
- Fuchs, E., Jaffe, J., Long, R. and Azam, F. (2002) 'Thin laser light sheet microscope for microbial oceanography', *Optics Express*, 10(2), p. 145. doi: 10.1364/OE.10.000145.
- Gan, J., Greenwood, S., Cobb, S. and Bushell, T. (2011) 'Indirect modulation of neuronal excitability and synaptic transmission in the hippocampus by activation of proteinase-activated receptor-2', *British Journal of Pharmacology*, 163(5), pp. 984–994. doi: 10.1111/j.1476-5381.2011.01293.x.
- Gerlach, J. von (1858) *Mikroskopische Studien aus dem Gebiete der menschlichen Morphologie*. Erlangen: Verlag von Ferdinand Enke.
- Glaser, A. K., Reder, N. P., Chen, Y., McCarty, E. F., Yin, C., Wei, L., Wang, Y., True, L. D. and Liu, J. T. C. (2017) 'Light-sheet microscopy for slide-free non-destructive pathology of large clinical specimens', *Nature Biomedical Engineering*, 1(7), p. 0084. doi: 10.1038/s41551-017-0084.

- Good, I. J. and Gaskins, R. A. (1971) 'Nonparametric roughness penalties for probability densities', *Biometrika*, 58(2), pp. 255–277.
- Gurr, E. (1951) 'Fluorescence microscopy.', *Journal of the Royal Naval Medical Service*, 37(3), pp. 133–40. Available at: <http://www.ncbi.nlm.nih.gov/pubmed/14861894>.
- Gustafsson, M. G. L. (1999) 'Extended resolution fluorescence microscopy', *Current Opinion in Structural Biology*, 9(5), pp. 627–628. doi: 10.1016/S0959-440X(99)00016-0.
- Gustafsson, M. G. L. (2000) 'Surpassing the lateral resolution limit by a factor of two using structured illumination microscopy.', *Journal of Microscopy*, 198(2), pp. 82–87. doi: 10.1046/j.1365-2818.2000.00710.x.
- Gustafsson, M. G. L., Agard, D. A. and Sedat, J. W. (1995) 'Sevenfold improvement of axial resolution in 3D wide-field microscopy using two objective lenses', in Wilson, T. and Cogswell, C. J. (eds) *Proc. SPIE*, pp. 147–156. doi: 10.1117/12.205334.
- Gustafsson, M. G. L., Agard, D. A. and Sedat, J. W. (1997) 'Method and apparatus for three-dimensional microscopy with enhanced depth resolution'. United States.
- Gustafsson, M. G. L., Agard, D. A. and Sedat, J. W. (1999) 'IM: 3D widefield light microscopy with better than 100 nm axial resolution', *Journal of Microscopy*, 195(July), pp. 10–16.
- Gustafsson, M. G. L., Shao, L., Carlton, P. M., Wang, C. J. R., Golubovskaya, I. N., Cande, W. Z., Agard, D. A. and Sedat, J. W. (2008) 'Three-dimensional resolution doubling in wide-field fluorescence microscopy by structured illumination.', *Biophysical Journal*, 94(12), pp. 4957–4970. doi: 10.1529/biophysj.107.120345.
- Heimstädt, O. (1911) 'Das Fluoreszenzmikroskop', *Z. wiss. Mikr.*, 28, pp. 330–337.
- Heintzmann, R. and Benedetti, P. A. (2006) 'High-resolution image reconstruction in fluorescence microscopy with patterned excitation', *Applied Optics*, 45(20), p. 5037. doi:

10.1364/AO.45.005037.

Helden, A. van, Dupré, S., Gent, R. van and Zuidervaart, H. (2010) *The Origins of the Telescope*. Amsterdam: KNAW Press.

Hell, S. W. and Wichmann, J. (1994) 'Breaking the diffraction resolution limit by stimulated emission: stimulated-emission-depletion fluorescence microscopy', *Optics Letters*, 19(11), p. 780. doi: 10.1364/OL.19.000780.

Helmchen, F. and Denk, W. (2005) 'Deep tissue two-photon microscopy', *Nature Methods*, 2(12), pp. 932–940. doi: 10.1038/nmeth818.

Herschel, J. F. W. (1845a) 'On a Case of Superficial Colour Presented by a Homogeneous Liquid Internally Colourless', *Philosophical Transactions of the Royal Society of London*, 135, pp. 143–145. doi: 10.1098/rstl.1845.0004.

Herschel, J. F. W. (1845b) 'On the Epipolic Dispersion of Light', *Philosophical Transactions of the Royal Society of London*, 135, pp. 147–153. doi: 10.1098/rstl.1845.0005.

Hooke, R. (1665) *Micrographia: or Some Physiological Descriptions of Minute Bodies, Made by Magnifying Glasses with Observations and Inquiries Thereupon*. James Allestry.

Hu, B., Li, G. and Brown, J. Q. (2019) 'Enhanced resolution 3D digital cytology and pathology with dual-view inverted selective plane illumination microscopy', *Biomedical Optics Express*, 10(8), p. 3833. doi: 10.1364/boe.10.003833.

Huang, D., Swanson, E., Lin, C., Schuman, J., Stinson, W., Chang, W., Hee, M., Flotte, T., Gregory, K., Puliafito, C. and Et, A. (1991) 'Optical coherence tomography', *Science*, 254(5035), pp. 1178–1181. doi: 10.1126/science.1957169.

Huisken, J. and Stainier, D. Y. R. (2007) 'Even fluorescence excitation by multidirectional selective plane illumination microscopy (mSPIM)', *Optics Letters*, 32(17), p. 2608. doi:

10.1364/OL.32.002608.

Huisken, J. and Stainier, D. Y. R. (2009) 'Selective plane illumination microscopy techniques in developmental biology', *Development*, 136(12), pp. 1963–1975. doi: 10.1242/dev.022426.

Huisken, J., Swoger, J., Del Bene, F., Wittbrodt, J. and Stelzer, E. H. K. (2004) 'Optical Sectioning Deep Inside Live Embryos by Selective Plane Illumination Microscopy', *Science*, 305(5686), pp. 1007–1009. doi: 10.1126/science.1100035.

Hwang, J. Y., Wachsmann-Hogiu, S., Ramanujan, V. K., Nowatzky, A. G., Koronyo, Y., Medina-Kauwe, L. K., Gross, Z., Gray, H. B. and Farkas, D. L. (2011) 'Multimodal wide-field two-photon excitation imaging: characterization of the technique for in vivo applications', *Biomedical Optics Express*, 2(2), p. 356. doi: 10.1364/BOE.2.000356.

Jemielita, M., Taormina, M. J., DeLaurier, A., Kimmel, C. B. and Parthasarathy, R. (2013) 'Comparing phototoxicity during the development of a zebrafish craniofacial bone using confocal and light sheet fluorescence microscopy techniques', *Journal of Biophotonics*. CRC Press, 6(11–12), pp. 920–928. doi: 10.1002/jbio.201200144.

Johnson, I. D. (2006) 'Practical Considerations in the Selection and Application of Fluorescent Probes', in *Handbook of Biological Confocal Microscopy*, pp. 353–364.

Jost, A., Tolstik, E., Feldmann, P., Wicker, K., Sentenac, A. and Heintzmann, R. (2015) 'Optical sectioning and high resolution in single-slice structured illumination microscopy by thick slice blind-SIM reconstruction', *PLOS ONE*, 10(7), pp. 1–10. doi: 10.1371/journal.pone.0132174.

Karadaglić, D. (2008) 'Image formation in conventional brightfield reflection microscopes with optical sectioning property via structured illumination', *Micron*, 39(3), pp. 302–310. doi: 10.1016/j.micron.2007.10.001.

Karadaglić, D. and Wilson, T. (2008) 'Image formation in structured illumination wide-field

- fluorescence microscopy', *Micron*, 39(7), pp. 808–818. doi: 10.1016/j.micron.2008.01.017.
- Karnowski, K., Ajduk, A., Wieloch, B., Tamborski, S., Krawiec, K., Wojtkowski, M. and Szkulmowski, M. (2017) 'Optical coherence microscopy as a novel, non-invasive method for the 4D live imaging of early mammalian embryos', *Scientific Reports*. Springer US, 7(1), p. 4165. doi: 10.1038/s41598-017-04220-8.
- Keller, H. E. (2006) 'Aberrations of Refractive Systems', in *Handbook of Biological Confocal Microscopy*, pp. 146–156.
- Keller, P. J. (2013) 'In vivo imaging of zebrafish embryogenesis', *Methods*. Elsevier Inc., 62(3), pp. 268–278. doi: 10.1016/j.ymeth.2013.03.015.
- Keller, P. J., Schmidt, A. D., Wittbrodt, J. and Stelzer, E. H. K. (2008) 'Reconstruction of Zebrafish Early Embryonic Development by Scanned Light Sheet Microscopy', *Science*, 322(5904), pp. 1065–1069. doi: 10.1126/science.1162493.
- Keller, P. J. and Stelzer, E. H. K. (2010) 'Digital Scanned Laser Light Sheet Fluorescence Microscopy', *Cold Spring Harbor Protocols*, 2010(5), p. pdb.top78-pdb.top78. doi: 10.1101/pdb.top78.
- Kervrann, C. and Boulanger, J. (2008) 'Local Adaptivity to Variable Smoothness for Exemplar-Based Image Regularization and Representation', *International Journal of Computer Vision*, 79(1), pp. 45–69. doi: 10.1007/s11263-007-0096-2.
- Kervrann, C., Boulanger, J. and Coupé, P. (2007) 'Bayesian Non-local Means Filter, Image Redundancy and Adaptive Dictionaries for Noise Removal', in *Scale Space and Variational Methods in Computer Vision*. Berlin, Heidelberg: Springer Berlin Heidelberg, pp. 520–532. doi: 10.1007/978-3-540-72823-8\_45.
- Kingslake, R. and Barry Johnson, R. (2010) 'Spherical Aberration', in *Lens Design*

*Fundamentals*. Elsevier, pp. 173–208. doi: 10.1016/B978-0-12-374301-5.00010-3.

Klar, T. A., Jakobs, S., Dyba, M., Egner, A. and Hell, S. W. (2000) 'Fluorescence microscopy with diffraction resolution barrier broken by stimulated emission', *Proceedings of the National Academy of Sciences of the United States of America*, 97(15), pp. 8206–8210. doi: 10.1073/pnas.97.15.8206.

Köhler, A. (1893) 'Ein neues Beleuchtungsverfahren für mikrophotographische Zwecke', *Z. wiss. Mikr.*, 10, pp. 433–440.

Köhler, A. (1904) 'Mikrophotographische Untersuchungen mit ultraviolettem Licht', *Z. wiss. Mikr.*, 21, pp. 129–273.

Krzic, U., Gunther, S., Saunders, T. E., Streichan, S. J. and Hufnagel, L. (2012) 'Multiview light-sheet microscope for rapid in toto imaging', *Nature Methods*, 9(7), pp. 730–733. doi: 10.1038/nmeth.2064.

Lauterbach, M. A., Ronzitti, E., Sternberg, J. R., Wyart, C. and Emiliani, V. (2015) 'Fast Calcium Imaging with Optical Sectioning via HiLo Microscopy', *PLOS ONE*, 10(12), pp. 1–13. doi: 10.1371/journal.pone.0143681.

Leeuwenhoeck, A. van (1677) 'Concerning little Animals observed in Rain-Well-Sea and Snow water; as also in water wherein pepper had lain infused', *Philosophical Transactions of the Royal Society of London*, 12, pp. 821–831. doi: 10.1098/rstl.1677.0003.

Legesse, F. B., Chernavskaia, O., Heuke, S., Bocklitz, T., Meyer, T., Popp, J. and Heintzmann, R. (2015) 'Seamless stitching of tile scan microscope images', *Journal of Microscopy*, 258(3), pp. 223–232. doi: 10.1111/jmi.12236.

Lim, D., Chu, K. K. and Mertz, J. (2008) 'Wide-field fluorescence sectioning with hybrid speckle and uniform-illumination microscopy.', *Optics Letters*, 33(16), pp. 1819–1821. doi:



10.1364/OL.33.001819.

Lim, D., Ford, T. N., Chu, K. K. and Mertz, J. (2011) 'Optically sectioned in vivo imaging with speckle illumination HiLo microscopy.', *Journal of Biomedical Optics*, 16(1), p. 016014. doi: 10.1117/1.3528656.

Liu, A., Xiao, W., Li, R., Liu, L. and Chen, L. (2019) 'Comparison of optical projection tomography and light-sheet fluorescence microscopy', *Journal of Microscopy*, 275(1), pp. 3–10. doi: 10.1111/jmi.12796.

Mazzaferri, J., Kunik, D., Belisle, J. M., Singh, K., Lefrançois, S. and Costantino, S. (2011) 'Analyzing speckle contrast for HiLo microscopy optimization', *Optics Express*, 19(15), p. 14508. doi: 10.1364/OE.19.014508.

McConnell, G., Trägårdh, J., Amor, R., Dempster, J., Reid, E. and Amos, W. B. (2016) 'A novel optical microscope for imaging large embryos and tissue volumes with sub-cellular resolution throughout', *eLife*, 5, pp. 1–15. doi: 10.7554/eLife.18659.

McNair, K., Davies, C. H. and Cobb, S. R. (2006) 'Plasticity-related regulation of the hippocampal proteome', *European Journal of Neuroscience*, 23(2), pp. 575–580. doi: 10.1111/j.1460-9568.2005.04542.x.

Mertz, J. and Kim, J. (2010) 'Scanning light-sheet microscopy in the whole mouse brain with HiLo background rejection', *Journal of Biomedical Optics*, 15(1), p. 016027. doi: 10.1117/1.3324890.

Minsky, M. (1961) 'Microscopy Apparatus U.S. Patent Application'. United States of America.

Neil, M. A. A., Juškaitis, R. and Wilson, T. (1997) 'Method of obtaining optical sectioning by using structured light in a conventional microscope', *Optics Letters*, 22(24), p. 1905. doi: 10.1364/OL.22.001905.

Neil, M. A. A., Juškaitis, R. and Wilson, T. (1998) 'Real time 3D fluorescence microscopy by two beam interference illumination', *Optics Communications*, 153(1–3), pp. 1–4. doi: 10.1016/S0030-4018(98)00210-7.

Orieux, F., Sepulveda, E., Lorient, V., Dubertret, B. and Olivo-Marin, J. C. (2012) 'Bayesian estimation for optimized structured illumination microscopy', *IEEE Transactions on Image Processing*, 21(2), pp. 601–614. doi: 10.1109/TIP.2011.2162741.

Oron, D., Tal, E. and Silberberg, Y. (2005) 'Scanningless depth-resolved microscopy', *Optics Express*, 13(5), p. 1468. doi: 10.1364/OPEX.13.001468.

Pang, J. and Cheung, G. (2017) 'Graph Laplacian Regularization for Image Denoising: Analysis in the Continuous Domain', *IEEE Transactions on Image Processing*, 26(4), pp. 1770–1785. doi: 10.1109/TIP.2017.2651400.

Pawley, J. B. (2006) *Handbook of Biological Confocal Microscopy*. Third Edit. New York: Springer.

Pedrotti, F. L., Pedrotti, L. M. and Pedrotti, L. S. (2007) *Introduction to Optics*. Third Edit. San Francisco: Pearson Education, Inc.

Petráň, M., Hadravský, M., Egger, M. D. and Galambos, R. (1968) 'Tandem-Scanning Reflected-Light Microscope\*', *Journal of the Optical Society of America*, 58(5), p. 661. doi: 10.1364/JOSA.58.000661.

Power, R. M. and Huisken, J. (2017) 'A guide to light-sheet fluorescence microscopy for multiscale imaging', *Nature Methods*, 14(4), pp. 360–373. doi: 10.1038/nmeth.4224.

Ritchie, L., Tate, R., Chamberlain, L. H., Robertson, G., Zagnoni, M., Sposito, T., Wray, S., Wright, J. A., Bryant, C. E., Gay, N. J. and Bushell, T. J. (2018) 'Toll-like receptor 3 activation impairs excitability and synaptic activity via TRIF signalling in immature rat and human

- neurons', *Neuropharmacology*. Elsevier Ltd, 135, pp. 1–10. doi: 10.1016/j.neuropharm.2018.02.025.
- Rohrbach, A. (2000) 'Observing Secretory Granules with a Multiangle Evanescent Wave Microscope', *Biophysical Journal*. Elsevier, 78(5), pp. 2641–2654. doi: 10.1016/S0006-3495(00)76808-1.
- Rohrbach, A. (2009) 'Artifacts resulting from imaging in scattering media: a theoretical prediction', *Optics Letters*, 34(19), p. 3041. doi: 10.1364/OL.34.003041.
- Rudin, L. I., Osher, S. and Fatemi, E. (1992) 'Nonlinear total variation based noise removal algorithms', *Physica D: Nonlinear Phenomena*, 60(1–4), pp. 259–268. doi: 10.1016/0167-2789(92)90242-F.
- Sanderson, J. (2019) *Understanding Light Microscopy*. Chichester: Wiley. doi: 10.1002/9781118696736.
- Santi, P. A. (2011) 'Light Sheet Fluorescence Microscopy A Review', *Journal of Histochemistry & Cytochemistry*, 59(2), pp. 129–138. doi: 10.1369/0022155410394857.
- Sasian, J. (2017) 'Method to design apochromat and superachromat objectives', *Optical Engineering*, 56(10), p. 1. doi: 10.1117/1.OE.56.10.105106.
- Scherz, P. J., Huisken, J., Sahai-Hernandez, P. and Stainier, D. Y. R. (2008) 'High-speed imaging of developing heart valves reveals interplay of morphogenesis and function', *Development*, 135(6), pp. 1179–1187. doi: 10.1242/dev.010694.
- Schindelin, J., Arganda-Carreras, I., Frise, E., Kaynig, V., Longair, M., Pietzsch, T., Preibisch, S., Rueden, C., Saalfeld, S., Schmid, B., Tinevez, J.-Y., White, D. J., Hartenstein, V., Eliceiri, K., Tomancak, P. and Cardona, A. (2012) 'Fiji: an open-source platform for biological-image analysis', *Nature Methods*, 9(7), pp. 676–682. doi: 10.1038/nmeth.2019.

- Schmid, B., Shah, G., Scherf, N., Weber, M., Thierbach, K., Campos, C. P., Roeder, I., Aanstad, P. and Huisken, J. (2013) 'High-speed panoramic light-sheet microscopy reveals global endodermal cell dynamics.', *Nature Communications*, 4, p. 2207. doi: 10.1038/ncomms3207.
- Schniete, J., Franssen, A., Dempster, J., Bushell, T. J., Amos, W. B. and McConnell, G. (2018) 'Fast Optical Sectioning for Widefield Fluorescence Mesoscopy with the Mesolens based on HiLo Microscopy', *Scientific Reports*, 8(1), p. 16259. doi: 10.1038/s41598-018-34516-2.
- Schröter, T. J., Johnson, S. B., John, K. and Santi, P. A. (2012) 'Scanning thin-sheet laser imaging microscopy (sTSLIM) with structured illumination and HiLo background rejection', *Biomedical Optics Express*, 3(1), p. 170. doi: 10.1364/BOE.3.000170.
- Shannon, C. E. (1949) 'Communication in the Presence of Noise', *Proceedings of the IRE*, 37(1), pp. 10–21. doi: 10.1109/JRPROC.1949.232969.
- Shimomura, O. (1979) 'Structure of the chromophore of Aequorea green fluorescent protein', *FEBS Letters*, 104(2), pp. 220–222. doi: 10.1016/0014-5793(79)80818-2.
- Shmaefsky, B. R. (2006) *Biotechnology 101*. Westport: Greenwood Press. doi: 10.1017/CBO9781107415324.004.
- Siedentopf, H. and Zsigmondy, R. (1902) 'Über Sichtbarmachung und Größenbestimmung ultramikroskopischer Teilchen, mit besonderer Anwendung auf Goldrubingläser', *Annalen der Physik*. WILEY-VCH Verlag, 315(1), pp. 1–39. doi: 10.1002/andp.19023150102.
- Smiles, J. (1958) 'Ultraviolet Microscopy', *Journal of Applied Bacteriology*, 21(1), pp. 137–142. doi: 10.1111/j.1365-2672.1958.tb00127.x.
- Sofroniew, N. J., Flickinger, D., King, J. and Svoboda, K. (2016) 'A large field of view two-photon mesoscope with subcellular resolution for in vivo imaging', *eLife*, 5. doi: 10.7554/eLife.14472.

Soulez, F., Denis, L., Tourneur, Y. and Thiébaud, E. (2012) 'Blind deconvolution of 3d data in wide field fluorescence microscopy', in *9th IEEE International Symposium on Biomedical Imaging (ISBI)*, pp. 1735–1738.

Sparrow, C. M. (1916) 'On Spectroscopic Resolving Power', *The Astrophysical Journal*, 44, p. 76. doi: 10.1086/142271.

Stirman, J. N., Smith, I. T., Kudenov, M. W. and Smith, S. L. (2016) 'Wide field-of-view, multi-region, two-photon imaging of neuronal activity in the mammalian brain', *Nature Biotechnology*. Nature Publishing Group, 34(8), pp. 857–862. doi: 10.1038/nbt.3594.

Stokes, G. G. (1852) 'On the Change of Refrangibility of Light', *Philosophical Transactions of the Royal Society of London*, 143, pp. 463–562. doi: 10.1098/rstl.1853.0016.

Ströhl, F. and Kaminski, C. F. (2017) 'Speed limits of structured illumination microscopy', *Optics Letters*, 42(13), p. 2511. doi: 10.1364/OL.42.002511.

Swoger, J., Verveer, P., Greger, K., Huisken, J. and Stelzer, E. H. K. (2007) 'Multi-view image fusion improves resolution in three-dimensional microscopy', *Optics Express*, 15(13), p. 8029. doi: 10.1364/OE.15.008029.

Tang, J. and Han, K. Y. (2020) 'Instantaneous non-diffracting light-sheet generation by controlling spatial coherence', *Optics Communications*. Elsevier Ltd., 474(April), p. 126154. doi: 10.1016/j.optcom.2020.126154.

Tinning, P. W., Franssen, A. J. P. M., Hridi, S. U., Bushell, T. J. and McConnell, G. (2018) 'A 340/380 nm light-emitting diode illuminator for Fura-2 AM ratiometric Ca<sup>2+</sup> imaging of live cells with better than 5 nM precision', *Journal of Microscopy*, 269(3), pp. 212–220. doi: 10.1111/jmi.12616.

Tomer, R., Lovett-Barron, M., Kauvar, I., Andalman, A., Burns, V. M., Sankaran, S., Grosenick,

- L., Broxton, M., Yang, S. and Deisseroth, K. (2015) 'SPED Light Sheet Microscopy: Fast Mapping of Biological System Structure and Function', *Cell*. Elsevier Inc., 163(7), pp. 1796–1806. doi: 10.1016/j.cell.2015.11.061.
- Töpperwien, M., Krenkel, M., Vincenz, D., Stöber, F., Oelschlegel, A. M., Goldschmidt, J. and Salditt, T. (2017) 'Three-dimensional mouse brain cytoarchitecture revealed by laboratory-based x-ray phase-contrast tomography', *Scientific Reports*, 7(1), p. 42847. doi: 10.1038/srep42847.
- Truong, T. V., Supatto, W., Koos, D. S., Choi, J. M. and Fraser, S. E. (2011) 'Deep and fast live imaging with two-photon scanned light-sheet microscopy', *Nature Methods*, 8(9), pp. 757–760. doi: 10.1038/nmeth.1652.
- Ventalon, C., Heintzmann, R. and Mertz, J. (2007) 'Dynamic speckle illumination microscopy with wavelet prefiltering.', *Optics Letters*, 32(11), pp. 1417–9. doi: 10.1364/OL.32.001417.
- Ventalon, C. and Mertz, J. (2005) 'Quasi-confocal fluorescence sectioning with dynamic speckle illumination.', *Optics Letters*, 30(24), pp. 3350–2. doi: 10.1364/OL.30.003350.
- Ventalon, C. and Mertz, J. (2006) 'Dynamic speckle illumination microscopy with translated versus randomized speckle patterns.', *Optics Express*, 14(16), pp. 7198–209. doi: 10.1364/OE.14.007198.
- Verveer, P. J., Gemkow, M. J. and Jovin, T. M. (1999) 'A comparison of image restoration approaches applied to three-dimensional confocal and wide-field fluorescence microscopy', *Journal of Microscopy*, 193(1), pp. 50–61. doi: 10.1046/j.1365-2818.1999.00421.x.
- Vettenburg, T., Dalgarno, H. I. C., Nylk, J., Coll-Lladó, C., Ferrier, D. E. K., Čižmár, T., Gunn-Moore, F. J. and Dholakia, K. (2014) 'Light-sheet microscopy using an Airy beam', *Nature Methods*, 11(5), pp. 541–544. doi: 10.1038/nmeth.2922.

Voie, A. H., Burns, D. H. and Spelman, F. A. (1993) 'Orthogonal-plane fluorescence optical sectioning: Three-dimensional imaging of macroscopic biological specimens', *Journal of Microscopy*, 170(3), pp. 229–236. doi: 10.1111/j.1365-2818.1993.tb03346.x.

Voigt, F. F., Kirschenbaum, D., Platonova, E., Pagès, S., Campbell, R. A. A., Kastli, R., Schaettin, M., Egolf, L., van der Bourg, A., Bethge, P., Haenraets, K., Frézel, N., Topilko, T., Perin, P., Hillier, D., Hildebrand, S., Schueth, A., Roebroek, A., Roska, B., Stoeckli, E. T., Pizzala, R., Renier, N., Zeilhofer, H. U., Karayannis, T., Ziegler, U., Batti, L., Holtmaat, A., Lüscher, C., Aguzzi, A. and Helmchen, F. (2019) 'The mesoSPIM initiative: open-source light-sheet microscopes for imaging cleared tissue', *Nature Methods*. Springer US, 16(11), pp. 1105–1108. doi: 10.1038/s41592-019-0554-0.

Wan, Y., McDole, K. and Keller, P. J. (2019) 'Light-Sheet Microscopy and Its Potential for Understanding Developmental Processes', *Annual Review of Cell and Developmental Biology*, 35(1), pp. 655–681. doi: 10.1146/annurev-cellbio-100818-125311.

WANG, E., BABBEY, C. M. and DUNN, K. W. (2005) 'Performance comparison between the high-speed Yokogawa spinning disc confocal system and single-point scanning confocal systems', *Journal of Microscopy*, 218(2), pp. 148–159. doi: 10.1111/j.1365-2818.2005.01473.x.

Watson, J. D. and Crick, F. H. C. (1953) 'Molecular Structure of Nucleic Acids: A Structure for Deoxyribose Nucleic Acid', *Nature*, 171(4356), pp. 737–738. doi: 10.1038/171737a0.

White, J. G. and Amos, W. B. (1987a) 'Confocal microscopy comes of age', *Nature*, 328(6126), pp. 183–184. doi: 10.1038/328183a0.

White, J. G. and Amos, W. B. (1987b) 'Confocal Scanning Microscope U.K. Patent Application'. United Kingdom.

White, J. G., Amos, W. B. and Fordham, M. (1987) 'An evaluation of confocal versus conventional imaging of biological structures by fluorescence light microscopy', *The Journal of Cell Biology*, 105(1), pp. 41–48. doi: 10.1083/jcb.105.1.41.

Wiedenmann, J., Oswald, F. and Nienhaus, G. U. (2009) 'Fluorescent proteins for live cell imaging: Opportunities, limitations, and challenges', *IUBMB Life*, 61(11), pp. 1029–1042. doi: 10.1002/iub.256.

Xiao, G. Q., Corle, T. R. and Kino, G. S. (1988) 'Real-time confocal scanning optical microscope', *Applied Physics Letters*, 53(8), pp. 716–718. doi: 10.1063/1.99814.

Yang, Z., Prokopas, M., Nylk, J., Coll-Lladó, C., Gunn-Moore, F. J., Ferrier, D. E. K., Vettenburg, T. and Dholakia, K. (2014) 'A compact Airy beam light sheet microscope with a tilted cylindrical lens.', *Biomedical Optics Express*, 5(10), pp. 3434–42. doi: 10.1364/BOE.5.003434.

Yew, E. Y. S., Sheppard, C. J. R. and So, P. T. C. (2013) 'Temporally focused wide-field two-photon microscopy: Paraxial to vectorial', *Optics Express*, 21(10), p. 12951. doi: 10.1364/OE.21.012951.

Young, J. Z. and Roberts, F. (1951) 'A Flying-spot Microscope', *Nature*, 167(4241), pp. 231–231. doi: 10.1038/167231a0.



## 8 Appendix

### 8.1 Matlab HiLo script for processing large stacks without GPU acceleration

```
%% Defining folders and files

close all
clearvars

bar = waitbar(0,'Define folders and parameters');

% Define image folder and names
[fnames_uni,indir_uni] = uigetfile(...
    '*.tif',...
    'Please select ALL UNIFORM files to process',...
    'MultiSelect','on');
[fnames_spe,indir_spe] = uigetfile(...
    '*.tif',...
    'Please select ALL SPECKLE files to process',...
    'MultiSelect','on');
[corr_img,corr_img_dir] = uigetfile(...
    '*.tif',...
    'Please select calibration image');
outdir = uigetdir(...
    'C:\',...
    'Please select output directory for HiLo images');

% Set optical sectioning thickness parameter and low frequency scaling
% factor in dialog box
opts.Interpreter = 'tex';
opts.Resize = 'on';
opts.WindowStyle = 'normal';
input_parameters = str2double(inputdlg(...
    {'Optical sectioning parameter','Low frequency scaling factor'},...
    'Define process parameters',1,{'2','1'},opts));
fnames_uni = {fnames_uni};
fnames_spe = {fnames_spe};
%% Define parameters

time = {'Create filter',...
    'Pre-allocation',...
    'Reading images and median filtering',...
    'Contrast evaluation',...
    'Filtering and scaling',...
    'Reconstruction and Saving',...
    'Total';...
    0,0,0,0,0,0,0};
```

```

% Get number of slices
stck_sz = numel(fnames_uni{1});
LoScale = input_parameters(2);
sigma = input_parameters(1);
info = imfinfo([indir_spe, '\', ...
    char(fnames_spe{1}(1))]); % Getting image properties
w = info.Width; % get image width
h = info.Height; % get image height
sigmaBP = w/(5*sigma); % band pass filter frequency
kc = nearest(sigmaBP*0.18); % cut-off frequency between hp and lp
                                % filter
sigmaLP = kc*2/2.355; % Finding sigma value for low pass and
                                % high pass filter
lambda = nearest(w/(2*kc)); % Side length of contrast evaluation
                                % mask by rounding to nearest odd
                                % integer
if mod(lambda,2) == 0 % lambda must be odd, this is to check
                                % if lambda is even and add 1 to make
                                % it odd
    lambda = lambda+1;
else
end

% Adjust dimension for padding based on mask size to avoid bright fringes
% around the edges of the image if there is specimen data up to the image
% edges.
h = h+2*lambda;
w = w+2*lambda;

% Create kernel for local contrast evaluation
nh = ones(lambda);
Nk = sum(nh(:));
%% Creating filters, pre-allocating and reading image stacks

% Create band pass, high and low pass filters
waitbar(1/9,bar,'Creating filters')

lp = lpgauss(h,w,sigmaLP);
hp = hpgauss(h,w,sigmaLP);
bp = bpgauss(h,w,sigmaBP);
bp = bp/max(bp(:));

tic
time{2,1} = round(toc,2);

% Preallocate memory for stacks
waitbar(2/9,bar,'Pre-allocating stacks')

uni = zeros(h,w,stck_sz,'single');
dif = zeros(h,w,stck_sz,'single');
weight = zeros(h,w,stck_sz,'single');
if corr_img == 0
else
    corr_img = imread([corr_img_dir, '\',corr_img]);
end

time{2,2} = round(toc,2);

```

```

tic

for i=1:stck_sz

    % Read images into stack
    waitbar(3/9,bar,['Reading image pair and band-pass filtering ',...
        int2str(i),' of ',int2str(stck_sz)])

    uni(:,:,i) = padarray(...
        medfilt2(...
            imread([indir_uni,'\ ',char(fnames_uni{1}(i))]) - corr_img,...
            [5 5],'symmetric'),...
            [lambda lambda],'symmetric');
    s = padarray(...
        medfilt2(...
            single(imread([indir_spe,'\ ',char(fnames_spe{1}(i))])...
            - corr_img),[5 5],'symmetric'),...
            [lambda lambda],'symmetric');
    d = fft2(s - uni(:,:,i));

    dif(:,:,i) = real(ifft2(bp.*d));
end

dif_min = min(dif(:));
time{2,3} = round(toc,2);
tic
%% Contrast evaluation

waitbar(4/9,bar,'Contrast evaluation')

for k = 1:stck_sz

    waitbar(5/10,bar,['Contrast evaluation ',int2str(k),...
        ' of ',int2str(stck_sz)])

    d = dif(:,:,k)-dif_min;
    mu = imfilter(d,nh,'same')/Nk;
    sd = stdfilt(d,nh);
    weight(:,:,k) = (sd./mu).^2;
end

waitbar(5/9,bar,'Weighting')

intermediate_weight = weight(lambda+1:end-lambda,lambda+1:end-lambda,:);
w_max = max(intermediate_weight(:));
weight = weight/w_max;

Lo_weighted = fft2(weight.*uni);
time{2,4} = round(toc,2);
tic
%% Filtering and scaling

Hi = zeros(h-2*lambda,w-2*lambda,stck_sz,'single');
Lo = zeros(h-2*lambda,w-2*lambda,stck_sz,'single');
nabla = zeros(stck_sz,1,'single');

for j = 1:stck_sz

```

```

waitbar(6/9,bar,['Filtering and low frequency scaling ',int2str(j),...
    ' of ',int2str(stck_sz)])

hi = fft2(uni(:,:,j)).*hp;
lo = Lo_weighted(:,:,j).*lp;
nabla(j) = abs(hi(1,kc))./abs(lo(1,kc));
hi_out = real(ifft2(hi));
lo_out = real(ifft2(lo));
Hi(:,:,j) = hi_out(lambda+1:end-lambda,lambda+1:end-lambda);
Lo(:,:,j) = lo_out(lambda+1:end-lambda,lambda+1:end-lambda);

end

%% Choose scaling factor
nabla_min = min(nabla);
happy = 0;
while(happy == 0)
    LoScale = str2double(inputdlg({'...
        'Minimum scaling factor of stack: ',num2str(nabla_min)}),...
        'Choose final low scaling factor',1,{num2str(nabla_min)}));
    figure(1)
    imshow(Hi(:,:,ceil(stck_sz/2)) +...
        LoScale * Lo(:,:,ceil(stck_sz/2)),[])
    happy = inputdlg({'Happy? (if so type "y")'},...
        'Accept or reject final low scaling factor',1,{ 'y'});
    if happy{1} == 'y'
        happy = 1;
    else
        happy = 0;
    end
end

close(figure(1))

time{2,5} = round(toc,2);
tic
%% Reconstruction and saving

waitbar(7/9,bar,'Reconstructing and saving')

HiLo = im2uint16(mat2gray(Hi + LoScale * Lo));
mkdir(outdir, strcat('HiLo_',int2str(sigma),'_',num2str(LoScale,2)));

for j=1:stck_sz

    waitbar(8/9,bar,['Reconstructing and saving ',int2str(j),...
        ' of ',int2str(stck_sz)])

    imwrite(HiLo(:,:,j),[outdir,...
        '\','HiLo_',...
        int2str(sigma),'_',num2str(LoScale,2),'HiLo',...
        int2str(j),'.tif'],'Compression','none')

end

time{2,6} = round(toc,2);
time{2,7} = round(sum(cell2mat(time(2,1:6))),2);

```

```
waitbar(1,bar,['DONE!!! ', 'Total time taken: ', '~', ...
    num2str(round(cell2mat(time(2,7)))), ' Seconds (', ...
    num2str(round(cell2mat(time(2,7))/60)), ' Minutes)'])
```

## 8.2 Matlab HiLo script for processing small stacks with GPU acceleration

```
%% Defining folders and files

clear

bar = waitbar(0, 'Define folders and parameters');

% Define image folder and names
[fnames_uni, indir_uni] = uigetfile(...
    '*.tif', ...
    'Please select ALL UNIFORM files to process', ...
    'MultiSelect', 'on');
[fnames_spe, indir_spe] = uigetfile(...
    '*.tif', ...
    'Please select ALL SPECKLE files to process', ...
    'MultiSelect', 'on');
[corr_img, corr_img_dir] = uigetfile(...
    '*.tif', ...
    'Please select calibration image');
outdir = uigetdir(...
    'C:\', ...
    'Please select output directory for HiLo images');

% Set optical sectioning thickness parameter and low frequency scaling
% factor in dialog box
opts.Interpreter = 'tex';
opts.Resize = 'on';
opts.WindowStyle = 'normal';
input_parameters = str2double(inputdlg(...
    {'Optical sectioning parameter', 'Low frequency scaling factor'}, ...
    'Define process parameters', 1, {'2', '1'}, opts));
fnames_uni = {fnames_uni};
fnames_spe = {fnames_spe};
%% Define parameters

tic

time = {'Create filter', ...
    'Pre-allocation', ...
    'Reading images and median filtering', ...
    'Contrast evaluation', ...
    'Filtering and scaling', ...
    'Reconstruction and Saving', ...
```

```

    'Total';...
    0,0,0,0,0,0,0};

% Get number of slices
stck_sz = numel(fnames_uni{1});
LoScale = input_parameters(2);
sigma = input_parameters(1);
info = imfinfo([indir_spe, '\', ...
    char(fnames_spe{1}(1))]); % Getting image properties
w = info.Width; % get image width
h = info.Height; % get image height
sigmaBP = w/(5*sigma); % band pass filter frequency
kc = nearest(sigmaBP*0.18); % cut-off frequency between hp and lp
                                % filter
sigmaLP = kc*2/2.355; % Finding sigma value for low pass and
                                % high pass filter
lambda = nearest(w/(2*kc)); % Side length of contrast evaluation
                                % mask by rounding to nearest odd
                                % integer
if mod(lambda,2) == 0 % lambda must be odd, this is to check
                                % if lambda is even and add 1 to make
                                % it odd
    lambda = lambda+1;
else
end

% Adjust dimension for padding based on mask size to avoid bright fringes
% around the edges of the image if there is specimen data up to the image
% edges.
h = h+2*lambda;
w = w+2*lambda;

% Create kernel for local contrast evaluation
nh = gpuArray(ones(lambda));
Nk = sum(nh(:));
%% Creating filters, pre-allocating and reading image stacks

% Create band pass, high and low pass filters
waitbar(1/9,bar,'Creating filters')

lp = lpgauss(h,w,sigmaLP);
hp = hpgauss(h,w,sigmaLP);
bp = bpgauss(h,w,sigmaBP);
bp = bp/max(bp(:));

time{2,1} = round(toc,2);
tic

% Preallocate memory for stacks
waitbar(2/9,bar,'Pre-allocating stacks')

uni = zeros(h,w,stck_sz,'single');
dif = zeros(h,w,stck_sz,'single');
weight = zeros(h,w,stck_sz,'single');
if corr_img == 0
else
    corr_img = imread([corr_img_dir, '\',corr_img]);

```

```

end

time{2,2} = round(toc,2);
tic

for i=1:stck_sz

    % Read images into stack
    waitbar(3/9,bar,['Reading image pair and band-pass filtering ',...
        int2str(i),' of ',int2str(stck_sz)])

    uni(:,:,i) = padarray(...
        medfilt2(...
            imread([indir_uni,'\ ',char(fnames_uni{1}(i))]) - corr_img,...
            [5 5], 'symmetric'),...
        [lambda lambda], 'symmetric');
    s = padarray(...
        medfilt2(...
            single(imread([indir_spe,'\ ',char(fnames_spe{1}(i))])...
            - corr_img),[5 5], 'symmetri'),...
        [lambda lambda], 'symmetric');
    d = fft2(gpuArray(s - uni(:,:,i)));

    dif(:,:,i) = gather(real(ifft2(gpuArray(bp).*d)));
end

dif_min = min(dif(:));
time{2,3} = round(toc,2);
tic
%% Contrast evaluation

waitbar(4/9,bar,'Contrast evaluation')

for k = 1:stck_sz

    waitbar(5/10,bar,['Contrast evaluation ',int2str(k),...
        ' of ',int2str(stck_sz)])

    d = gpuArray(dif(:,:,k)-dif_min);
    mu = imfilter(d,nh,'same')/Nk;
    sd = stdfilt(d,nh);
    clear d
    weight(:,:,k) = gather(sd./mu);
end

clear mu sd

waitbar(5/9,bar,'Weighting')

intermediate_weight = weight(lambda+1:end-lambda,lambda+1:end-lambda,:);
w_max = max(intermediate_weight(:));
weight = weight/w_max;

Lo_weighted = fft2(weight.*uni);
time{2,4} = round(toc,2);
tic
%% Filtering and scaling

```

```

hp = gpuArray(hp);
lp = gpuArray(lp);
Hi = zeros(h-2*lambda,w-2*lambda,stck_sz,'single');
Lo = zeros(h-2*lambda,w-2*lambda,stck_sz,'single');
nabla = gpuArray(zeros(stck_sz,1,'single'));

for j = 1:stck_sz

    waitbar(6/9,bar,['Filtering and low frequency scaling ',...
        int2str(j),' of ',int2str(stck_sz)])

    hi_gpu = fft2(gpuArray(uni(:, :, j))).*hp;
    lo_gpu = gpuArray(Lo_weighted(:, :, j)).*lp;
    nabla(j) = abs(hi_gpu(1,kc-1))./abs(lo_gpu(1,kc-1));
    hi_out = gather(real(ifft2(hi_gpu)));
    lo_out = gather(real(ifft2(lo_gpu)));
    Hi(:, :, j) = hi_out(lambda+1:end-lambda,lambda+1:end-lambda);
    Lo(:, :, j) = lo_out(lambda+1:end-lambda,lambda+1:end-lambda);

end

nabla_min = min(nabla);
happy = 0;
while(happy == 0)
    LoScale = str2double(inputdlg({'...
        'Minimum scaling factor of stack: ',num2str(nabla_min)}),...
        'Choose final low scaling factor',1,{num2str(nabla_min)}));
    figure(1)
    imshow(Hi(:, :, ceil(stck_sz/2)) + ...
        LoScale * Lo(:, :, ceil(stck_sz/2)), [])
    happy = inputdlg({'Happy? (if so type "y")'},...
        'Accept or reject final low scaling factor',1,{ 'y' });
    if happy{1} == 'y'
        happy = 1;
    else
        happy = 0;
    end
end

close(figure(1))
clear hi_gpu lo_gpu

time{2,5} = round(toc,2);
tic
%% Reconstruction and saving

waitbar(7/9,bar,'Reconstructing and saving')

HiLo = im2uint16(mat2gray(Hi + LoScale * Lo));
mkdir(outdir, strcat('HiLo_', int2str(sigma), '_', num2str(LoScale,2)));

for j=1:stck_sz

    waitbar(8/9,bar,['Reconstructing and saving ',int2str(j),...
        ' of ',int2str(stck_sz)])

```



```

        imwrite(HiLo(:,:,j),[outdir,...
            '\','HiLo_',...
            int2str(sigma),'_',num2str(LoScale,2),...
            '\HiLo',int2str(j),'.tif'],'Compression','none')
    end
    time{2,6} = round(toc,2);
    time{2,7} = round(sum(cell2mat(time(2,1:6))),2);
    waitbar(1,bar,['DONE!!! ','Total time taken: ','~',...
        num2str(round(cell2mat(time(2,7)))), ' Seconds (',...
        num2str(round(cell2mat(time(2,7))/60)), ' Minutes)'])

```

## 8.3 User-made functions

### 8.3.1 Low pass filter function

```

function out = lpgauss(H,W,SIGMA)

% Creates a 2D Gaussian filter for a Fourier space image
% W is width of the source image and H is the height. SIGMA is the
% standard deviation of the Gaussian.

% Convert input numbers to 32-bit float format and scale sigma to correct
% distance for non-square images.
H = single(H);
W = single(W);
kcx = (SIGMA);
kcy = ((H/W)*SIGMA);

% Creat meshgrid with zero in the centre of the image to form a Gaussian
% distribution. The output is inverted FFT shifted to match an FFT of an
% image when used as a filter outside this function.
[x,y] = meshgrid(-floor(W/2):floor((W-1)/2), -floor(H/2):floor((H-1)/2));
out = ifftshift(exp(-(x.^2/(kcx^2)+y.^2/(kcy^2))));

end

```

### 8.3.2 High pass filter function

```

function out = hpgauss(H,W,SIGMA)

% Creates a 2D Gaussian filter for a Fourier space image of height H and
% width W. SIGMA is the standard deviation of the Gaussian.

% Call lpgauss() function and subtract it from unity to form the
% complementary high pass filter.
out = 1-lpgauss(H,W,SIGMA);

```

```
end
```

### 8.3.3 Band pass filter function

```
function out = bpgauss(H,W,SIGMA)

% Input height H, width W and standard deviation SIGMA to construct a
% band pass filter

% Convert input numbers to 32-bit float format and scale sigma to correct
% distance for non-square images.
H = single(H);
W = single(W);
kcx = SIGMA;
kcy = (H/W)*SIGMA;

% Create meshgrid with zero in the centre of the image to form a Gaussian
% distribution. The output is inverted FFT shifted to match an FFT of an
% image when used as a filter outside this function. The band pass filter
% is constructed by subtracting one Gaussian from another with two times
% the standard deviation.
[x,y] = meshgrid(-floor(W/2):floor((W-1)/2), -floor(H/2):floor((H-1)/2));
out = ifftshift(exp(-(x.^2/(2*kcx^2)+y.^2/(2*kcy^2))))...
    -exp(-(x.^2/(kcx^2)+y.^2/(kcy^2))));

end
```

### 8.3.4 Project height to colourmap function

```
function rgb_heightmap = ProjectHeight2RGB(image_stack, varargin)
% This function takes as an input an image stack (X,Y,Z) and outputs a 2D
% RGB image with the height information encoded in a colourmap. The
% colourmap can be chosen as a name-value pair or defaults to the 'jet'
% colourmap. The colourmap is automatically scaled to the height of the
% image stack.

% Default colourmap 'jet' and list of options.
default_hmap = 'jet';
expected_cmaps = {'parula','jet','hot','pink','hsv','flag','turbo',...
    'cool','spring','summer','autumn','winter','gray','bone',...
    'copper','lines','colorcube','prism'};

% Generate parser object for the function input that checks that inputs
% are compatible. Image stack must be numeric and colourmap must be given
% as name-value pair, eg. 'colourmap','parula' in the VARARGIN field in
% the function call
p = inputParser;
```

```

addRequired(p, 'image_stack', @isnumeric)
addParameter(p, 'colourmap', default_hmap, ...
    @(x) any(validatestring(x, expected_cmaps)))
parse(p, image_stack, varargin{:})

% Convert input image stack to 32-bit float, get slice number and
% construct scaled colourmap to match the height of the stack.
im_stack = single(p.Results.image_stack);
z = size(im_stack, 3);
cmap = str2func(p.Results.colourmap);
hmap = single(cmap(z));

% Shift dimension of hmap and multiply element-wise with the image stack.
% Then collapse the image stack by summing up along the z dimension,
% resulting in the 2D RGB output image.
hmap = shiftdim(hmap, -2);
rgb_heightmap = im2uint8(mat2gray(squeeze(sum(im_stack.*hmap, 3))));

end

```